Technical University of Munich
TUM Campus Straubing for Biotechnology and Sustainability

Theoretical analysis and model-based optimization of enzymatic cascade reaction systems

Leandros Paschalidis

Complete reprint of the dissertation approved by the TUM Campus Straubing for Biotechnology and Sustainability of the Technical University of Munich for the award of the

Doktor der Ingenieurwissenschaften (Dr.-Ing.).

Chair: Prof. Dr.-Ing. Michael Zavrel

Examiners:

1. Prof. Dr.-Ing. Jakob Burger
2. Prof. Dr. rer. nat. Volker Sieber

The dissertation was submitted to the Technical University of Munich on 18.04.2024 and accepted by the TUM Campus Straubing for Biotechnology and Sustainability on 31.07.2024.

Acknowledgments

The following work was carried out during my employement as a research associate in the Laboratory of Chemical Process Engineering at the Campus for Biotechnology and Sustainability of the Technical University of Munich. First of all, I would like to thank my supervisor Prof. Dr.-Ing. Jakob Burger for his constant support, guidance, and encouragement which have been invaluable throughout the entire process. I highly valued the biweekly meetings we held in our laboratories jour fixe, which not only helped to keep my research on track but also provided me with plenty of encouragement. I am very grateful for the immeasurable contributions he made to my education and my professional development as a researcher and an engineer. I can not imagine a better environment to do research in. I would also like to express my gratitude to Prof. Dr. rer. nat. Volker Sieber for giving me the chance to contribute to the very interesting topic of enzymatic cascades.

I would like to thank all of my hard working colleagues at the Laboratory of Chemical Process Engineering for the scientific discussions, support, and exchange of knowledge. I am especially grateful to Ms. Birgit Aich-Bauer, Mr. Stefan Hartl, and Ms. Christina Wolf for their support and guidance in administrative issues. Further, I would like to thank the colleagues from the Chair of Chemistry for Biogenic Resources for the collaboration in various projects. A special thanks to Dr. rer. nat. Sara Arana-Peña for the interesting and successful work we did together as well as her positive outlook that helped make research much more fun.

I would also like to thank all of the university students and employees who I met, exchanged ideas and worked with during my time in the university. A special thanks to all the bachelor's and master's students that collaborated with me in research, either for their thesis or the cooperative design project. A special thanks also to our neighbors, the colleagues from the Professorship for Electrobiotechnology, for the friendly climate we enjoyed and all the fun we had together the past few years.

Finally, I would like to thank Prof. Dr. Dr. h. c. Hubert Schmidbaur for his insightful and extremely helpful advice as my mentor as well as my parents in Thessaloniki, my brother in Athens, and the rest of my family in Munich for their inexhaustable patience and support over the years.

Thessaloniki, January 2024
Leandros Paschalidis

Abstract

Systems with enzymatic cascade reactions are promising alternatives to complex chemical syntheses or microbial bioreactors. A large number of enzymatic cascade reactions have been developed in the past years. Generally, the enzymes of the cascade are dissolved in the aqueous phase in which the reactions occur or they are immobilized inside the pores of solid particles, which are brought in contact with the aqueous phase that contains the substrates and cofactors. Designing and optimizing enzymatic cascade reaction processes solely based on laboratory experiments is challenging. There are numerous decisions to be made and parameters to be selected. Kinetic modeling can help make these decisions in a systematic way. In the present work, enzymatic cascade reaction systems are modeled and analyzed.

For a system with dissolved enzymes that produces α-ketoglutarate, model-based, multi-objective, dynamic optimization is applied. Pareto-optimal process schedules, which are best compromises between space-time yield, enzyme consumption, and cofactor consumption, are determined and visualized. Depending on the importance of the individual objectives, the optimal process schedules vary. It is demonstrated, that multi-objective optimization is a valuable tool for the development of enzymatic cascades. It provides decision support for making further experiments, finding bottlenecks in the cascade, and choosing an optimal process schedule for production.

Further, a phenomenon called boosting by intermediates, where adding intermediates of an enzymatic cascade reaction at the start of the reaction process increases the space-time yield significantly is explained using kinetic models. The phenomenon was studied with mathematical models and several theorems are proven. The dynamics of four chemical reaction networks that exhibit boosting by intermediate are studied under the quasi steady state approximation and numerical solutions. A novel graphical method that can be used to deduce which intermediates boost linear, redox enzymatic cascades is presented.

Systems with immobilized enzymes are also studied. Enzymes can be immobilized in porous particles using different spatial immobilization distributions (SIDs). A theoretical framework for modeling enzymatic cascade reactions catalyzed by enzymes immo-

bilized in porous particles is developed. The developed framework is used to study and characterize four different SIDs for a two-step enzymatic cascade reaction. Individual immobilization, homogeneous co-immobilization, and two heterogeneous co-immobilization strategies. Through analytical solutions of the model equations and Monte Carlo sampling of parameters, general conclusions are derived for the conditions under which the different SIDs are advantageous.

Finally, for flow systems with immobilized enzymes, the comparison of spatial immobilization distributions is combined with the comparison of different designs of catalyst zones. General theoretical insights into the selection of different spatial immobilization distributions and catalyst zones are derived through analytical solutions and a mathematical proof.

Kurzfassung

Systeme mit enzymatischen Kaskadenreaktionen sind vielversprechende Alternativen zu komplexen chemischen Synthesen oder mikrobiellen Bioreaktoren. In den letzten Jahren wurde eine Vielzahl enzymatischer Kaskadenreaktionen entwickelt. Im Allgemeinen sind die Enzyme der Kaskade in der wässrigen Phase, in der die Reaktionen stattfinden, gelöst oder in den Poren fester Partikel immobilisiert, die mit der wässrigen Phase in Kontakt gebracht werden, die die Substrate und Cofaktoren enthält. Die Entwicklung und Optimierung enzymatischer Kaskadenreaktionsprozesse ausschließlich auf der Grundlage von Laborexperimenten ist eine Herausforderung. Es sind zahlreiche Entscheidungen zu treffen und Parameter auszuwählen. Die kinetische Modellierung kann dabei helfen, diese Entscheidungen systematisch zu treffen. In der vorliegenden Arbeit werden enzymatische Kaskadenreaktionssysteme modelliert und analysiert.

Für ein System mit gelösten Enzymen, das α-Ketoglutarat produziert, wird eine modellbasierte, mehrobjektive, dynamische Optimierung angewendet. Pareto-optimale Prozesspläne, die den besten Kompromiss zwischen Raum-Zeit-Ausbeute, Enzymverbrauch und Cofaktorverbrauch darstellen, werden ermittelt und visualisiert. Je nach Bedeutung der einzelnen Ziele variieren die optimalen Prozesspläne. Es wird gezeigt, dass die Mehrzieloptimierung ein wertvolles Werkzeug für die Entwicklung enzymatischer Kaskaden ist. Sie bietet Entscheidungsunterstützung für die Durchführung weiterer Experimente, das Auffinden von Engpässen in der Kaskade und die Auswahl eines optimalen Prozessplans für die Produktion.

Darüber hinaus wird mithilfe kinetischer Modelle ein Phänomen namens Boosting by Intermediates erklärt, bei dem die Zugabe von Intermediaten einer enzymatischen Kaskadenreaktion zu Beginn des Reaktionsprozesses die Raum-Zeit-Ausbeute deutlich erhöht. Das Phänomen wurde mit mathematischen Modellen untersucht und mehrere Theoreme wurden bewiesen. Die Dynamik von vier chemischen Reaktionsnetzwerken, die eine Verstärkung durch Zwischenprodukte zeigen, wird unter der quasi-stationären Näherung und numerischen Lösungen untersucht. Es wird eine neuartige grafische Methode vorgestellt, mit der abgeleitet werden kann, welche Zwischenprodukte lineare Redox-Enzymkaskaden ankurbeln.

Es werden Systeme mit immobilisierten Enzymen untersucht. Enzyme können mithilfe verschiedener räumlicher Immobilisierungsverteilungen (SIDs) in porösen Partikeln immobilisiert werden. Es wird ein theoretischer Rahmen für die Modellierung enzymatischer Kaskadenreaktionen entwickelt, die durch in porösen Partikeln immobilisierte Enzyme katalysiert werden. Das entwickelte Framework wird verwendet, um vier verschiedene SIDs für eine zweistufige enzymatische Kaskadenreaktion zu untersuchen und zu charakterisieren. Individuelle Immobilisierung, homogene Co-Immobilisierung und zwei heterogene Co-Immobilisierungsstrategien. Durch analytische Lösungen der Modellgleichungen und Monte-Carlo-Probenahme von Parametern werden allgemeine Schlussfolgerungen für die Bedingungen abgeleitet, unter denen die verschiedenen SIDs vorteilhaft sind.

Schließlich, wird für Strömungssysteme mit immobilisierten Enzymen der Vergleich räumlicher Immobilisierungsverteilungen mit dem Vergleich verschiedener Designs von Katalysatorzonen kombiniert. Durch analytische Lösungen und einen mathematischen Beweis werden allgemeine theoretische Erkenntnisse zur Auswahl unterschiedlicher räumlicher Immobilisierungsverteilungen und Katalysatorzonen abgeleitet.

Declaration

This dissertation contains material that has been published previously or that is included in submitted publications or publications under preparation. In the following, these publications are listed together with a statement on the contributions of the author of the present dissertation.

1. L. Paschalidis, B. Beer, S. Sutiono, V. Sieber, J. Burger: Design of enzymatic cascade reactors through multi-objective dynamic optimization. Biochemical Engineering Journal 181 (2022) 108384.

   The author developed the methodology and the mathematical model, wrote the python and pyomo code, evaluated the results and wrote the manuscript except of the experiments section (the experiments section was written by Dr. rer. nat. Barbara Beer and is not included in the dissertation).

2. L. Paschalidis, D. Fröschl, M. Ibañez, S. Sutiono, V. Sieber, J. Burger: Boosting of enzymatic cascades by intermediates: Theoretical analysis and model-based optimization. Biochemical Engineering Journal 210 (2024) 109440.

   The author developed the methodology and the mathematical models, prooved the theorems, evaluated the results and wrote the manuscript.

3. L. Paschalidis, S. Arana-Peña, V. Sieber, J. Burger: Mechanistic modeling, parametric study and optimization of immobilization of enzymatic cascades in porous particles. Reaction Chemistry and Engineering 8 (2023) 2234-2244.

   The author developed the methodology and the mathematical model, wrote the python code, derived the analytical solutions, evaluated the results and wrote the manuscript.

4. L. Paschalidis, S. Arana-Peña, V. Sieber, J. Burger: Modeling Enzymatic Cascade Reactions Immobilized in Plug-Flow Reactors for Flow Biocatalysis. Chemie Ingeniuer Technik 96 (2024) 741-748.

   The author developed the methodology and the mathematical model, wrote the code, derived the analytical solutions, evaluated the results and wrote the manuscript (the introduction was written together with Dr. rer. nat. Sara Arana-Peña.).

Parts of the first three publications appear in the introduction. The first publication appears in the second chapter. The second publication appears in the third chapter. The third publication and part of the fourth publication appear in the fourth chapter.

Contents

List of main Symbols

Latin symbols

A	Area of the opening of the pore
A_k	Magnitude of the enzyme supplementation rate
c_1	Molar concentration of the oxidized form of the cofactor
c_2	Molar concentration of the reduced form of the cofactor
D_i	Diffisuvity of substrate i
e_j	Total amount of enzyme j inside the reactor
E^j	Molar concentration of enzyme j
E_n^j	Molar concentration of enzyme j inside pore n
$f_{i,t}$	Correction factor in data reconciliation
f_FOK	First-order kinetic modulus in the parametric study
f_MMK	Michaelis-Menten kinetic modulus in the parametric study
k_cat	Turnover number
$k_\mathrm{L}a$	Volumetric mass transfer coefficient
k_k	Kinetic parameter of reaction k
K_m	Michaelis-Menten kinetic parameter
K_i^j	Michaelis-Menten kinetic parameter of enzyme j on substrate i
K_n	Modulus in the theoretical analysis of zone designs
L	Length of the pore
$m_{1,n}$	Parameter in the theoretical analysis of SIDs
$m_{2,n}$	Parameter in the theoretical analysis of SIDs
n_i^D	Diffusive molar flow-rate of substrate i in/out of the pore
N_{O_2}	Mass tranfer rate of oxygen
N_n	Total number of pores of type n
p_{O_2}	Partial pressure of oxygen
$p_{1,n}$	First kinetic parameter in the theoretical analysis of SIDs
$p_{2,n}$	Second kinetic parameter in the theoretical analysis of SIDs
$p_{3,n}$	Third kinetic parameter in the theoretical analysis of SIDs
r_s^j	Rate of supplementation of enzyme j

$r_{j,n}$	Micro reaction rates inside pore n
R	Ratio of yields
S_i	Molar concentration of substrate i
S_i^*	Solubility of substrate i
$S_{i,n}$	Molar concentration of substrate i inside pore n
$S_{i,0}$	Molar concentration of substrate i in the bulk of the reaction solution
S_i^{qss}	Molar concentration of substrate i in quasi steady-state
t	Time
t_{f}	Total reaction process duration
t_{l}	Supplementation times
t_{p}	Reactor preparation time
u	Average speed of the reaction solution throw the flow reactor
v_k	Rate of reaction k
$V_{\max}^j$	Maximum reaction rate of enzyme j
x	Length axis through the pore
x_i	Coefficient of the characteristic equation
$X_{i,t}$	Measured molar concentration of substrate i at time t
Y_m	Yield
z	Length axis through the flow reactor

Greek symbols

α_i	Oxidation number of intermediate i
$\epsilon_{i,t}^{\mathrm{abs}}$	Absolute error of the measurment of the concentration of substrate i at time t
$\epsilon_{i,t}^{\mathrm{rel}}$	Relative error of the measurment of the concentration of substrate i at time t
ϵ^w	Epsilon-constraint
λ_t	Sum of the measured molar concentrations
μ_1	First modulus in the theoretical study of SIDs
μ_2	Second modulus in the theoretical study of SIDs
τ	Residence time in the flow reactor
τ_{f}	Total time in the flow reactor
Φ^w	Optimization objective w
x_i	Cofactor-intermediate dependence equation coefficient
ψ_t	Sum of the absolute errors at time point t

Matrices and Vectors

$\mathbf{D}$	Diffusivity vector
$\mathbf{n}$	Mass transfer vector
$\mathbf{p}$	Substrate concentration vector
$\mathbf{q}$	Stoichiometry vector
$\mathbf{Q}$	Reduced stoichiometry matrix
$\mathbf{r}_n$	Micro-reaction rate vector
$\mathbf{s}$	Substrate concentration vector
$\mathbf{s}_n$	Substrate concentration vector (concentration inside pore n)
$\mathbf{s}_0$	Substrate concentration vector (bulk concentration)
$\mathbf{U}$	Complete stoichiometry matrix
$\mathbf{v}$	Reaction rate vector
$\mathbf{x}$	Characteristic equation coefficient vector

Abbreviations

CRN	Chemical reaction network
CC	Cofactor consumption
DER	Derivative
EC	Enzyme consumption
FOK	First-order kinetics
MOO	Multi-Objective Optimization
MMK	Michaelis-Menten kinetics
qss	Quasi steady state
SID	Spatial immoblization distribution
STY	Space-time yield

1 Introduction

1.1 State of the art

Systems with enzymatic cascade reactions are promising alternatives to complex chemical syntheses or microbial bioreactors. A cascade reaction is the combination of two or more reaction steps in one pot without isolating the intermediates. In an enzymatic cascade, an enzyme catalyzes at least one reaction step [1]. Enzymatic cascade reactions are advantageous because they avoid the need for purification of the intermediates and bypass unfavorable equilibria [1–3]. Moreover, they enable higher yield and improved atom economy [2, 3] and produce less waste, since less chemicals are used [2].

A large number of enzymatic cascade reactions have been developed in the past years [3–7], e.g., for the conversion of D-glucose into isobutanol or ethanol [4], D-xylose or D-glucuronate into α-ketoglutarate [8, 9], and D-glucose into L-alanine [10]. The reaction networks of *in vitro* cascades often have similar structures with their *in vivo* counterparts but different challenges exist in modeling and model-based optimization for the two. The task in *in vivo* systems is the genetic modification of the cells to direct the metabolic flux towards the wanted products by preventing certain pathways and allowing others. The *in vivo* cascades are most often modeled to be in steady state. On the other hand, *in vitro* cascades often display complex non-linear dynamics, and the challenge in designing their reaction processes lies in the selection of process parameters (e.g., titers of enzymes or cofactor) to optimize one or more objectives. Redox, *in vitro* cascades often reach a quasi steady state and are an exception.

Generally, the enzymes of the cascade are dissolved into the aqueous phase, in which the reactions occur, or they are immobilized inside the pores of solid porous particles, which are brought in contact with the aqueous phase that contains substrates, intermediates, and products [11–16]. While the immobilization approach is more challenging in preparation, it promises improved enzyme stability [17–22], facilitated catalyst separation, and, not least, allows for continuous/repeated catalyst use [23, 24]. Furthermore, it can improve enzyme activity [25, 26] and help with enzyme purification [27]. Specifically for immobilization, many experimental studies have been published on the topic of immobilizing and comparing and characterizing enzyme spatial immobilization distributions (SIDs) in the past few years [28–32]. By contrast, little work has been done in comparing SIDs using modeling approaches.

Increasing the productivity of enzymatic cascades is an important task [33]. A lot of success has been found to this end in the areas of enzyme engineering and enzyme immobilization [13, 16, 34–42]. However, attention must be also given to the optimization of the reaction processes themselves. Straightforward thinking implies increasing the titers of enzymes and cofactors to increase space-time yield. However, there is often an upper limit to the amount of enzymes that can be used. Even when no other physical limitations exist, eventually the solubility limit of each enzyme is reached [43, 44]. Further, both enzymes and cofactors are expensive, and not recycling them is prohibitive [45, 46]. Finally, the complex dynamics of cascade reaction systems might often require that certain cofactor-dependent enzymes be kept at low titers to avoid cofactor depletion and the termination of the cascade reaction.

Designing enzymatic cascade reaction processes solely based on laboratory experiments has challenges. There are numerous parameters in an enzymatic cascade reaction process, e.g., the titers and addition schedule of substrates, several enzymes, and cofactors, the used spatial immobilization distribution when the enzymes are immobilized, etc. Only a limited set of experiments can be done, so when the design of the reaction processes is only based on experiments, a large part of the parameter space remains unexplored. Kinetic modeling and model-based optimization is, therefore, an essential step, commonly done in the scientific community. Modeling *in vitro* cascades has been studied also by other researchers in the past few years [9, 47–54]. Notable contributions to the topic are the works of Shen et al. [9] and Johannsen et al. [51]. Shen et al. demonstrated that a reliable kinetic model can be developed for a multi-enzyme cascade and used to study its dynamics. Johannsen et al. demonstrated how kinetic models of multi-enzyme cascades can be used to design and optimize a real process carried out in a mini-plant. This dissertation goes beyond the already achieved tasks and provides novel results both in model-based optimization and the theoretical analysis of enzymatic cascade reaction processes. The goal and contents of the dissertation are discussed in the following section.

1.2 Thesis and structure of the work

The goal of the work is to demonstrate that:

- the design of enzymatic cascade reaction systems can be done using parameterized, kinetic models through model-based, multi-objective optimization and,
- that when the parametrization of models requires too many experiments or other resources, design decisions can be made based on the structure of the equations of the kinetic models.

The present work deals with both dissolved and immobilized enzyme systems. Also, both dynamic and continuous reaction processes are studied. When studying real reaction processes, experimental data provided by our collaborators in the Chair of Biogenic Resources of the Technical University of Munich are used to parameterize the models.

For systems with dissolved enzymes, it is demonstrated how a dynamic process can be designed through model-based, multi-objective optimization. As an application, the production of α-ketoglutarate via the oxidative pathway of C6 uronic acids is chosen [8]. Pareto-optimal process schedules which are best compromises between space-time yield, enzyme consumption, and cofactor consumption are determined, visualized, and discussed for a batch reaction process that produces α-ketoglutarate. The applied methodology and the results are presented in Section 2.

Further, a theoretical analysis of systems with dissolved enzymes is carried out. The focus of our analysis is the reaction networks of four redox, cofactor-balanced cascade reactions, three of which were developed by Gargiulo et al., Sutiono et al. and Gutterl et al. [2, 4, 55, 56]. As demonstrated by Sutiono et al. [56] experimentally, the cofactors and intermediates of redox cascades often reach a quasi steady state during batch processes. The dynamics of the reaction networks were studied with mathematical models, via the quasi steady state approximation and numerical solutions of the model equations. A phenomenon called boosting by intermediates, which was first observed and discussed by Sutiono et al. [56], was explained and analyzed using mathematical models and several theorems about boosting by intermediate were prooven. A graphical method was developed to answer the question of which intermediates boost or delay linear redox cascades. The applied methodology and the results are presented in Section 3.

For systems with immobilized enzymes, some fundamental theoretical questions about the optimal way to distribute enzymes in the pores of porous particles are tackled for dynamic processes. During the immobilization of several enzymes in porous particles, one could wonder what is the best spatial immobilization distribution (SID) to fix the enzymes relative to each other distributed over particles, and inside the pores [34]. A mechanistic modeling framework is developed for immobilized enzymatic cascades in porous particles based on first principles. The framework is versatile enough to model and compare various SIDs. The performance of different SIDs is compared against each other in parametric studies to elucidate when certain SIDs are better. When possible, analytical solutions for the macro-kinetics are derived. Otherwise, Monte Carlo sampling is used to check parameter sensitivities. Based on the results of the parametric studies, some general guidelines from our theory are derived. The applied methodology and the results are presented in Section 4.

For known parameter values (i.e., diffusivities, kinetic parameters, etc.) model-based optimization can be applied to the design of systems with immobilized enzymes. It is demonstrated how such systems can be designed with model-based optimization in an application example. The optimal SID and enzyme ratio is selected for a two-step cascade reaction. The applied methodology and the results are presented in Section 4.

Finally, for continuous processes with immobilized enzymes, the theoretical analysis of spatial immobilization distributions is combined with the selection of conceptual zone designs of different porous particles inside the reactors. Where possible analytical solutions are derived. A theorem about the optimal way to distribute catalysts (enzymes) in different zones in a plug-flow reactor is prooven. The applied methodology and the results are presented in Section 4. An overview of the studied problems as well as their organisation inside the thesis is given in Figure 1.

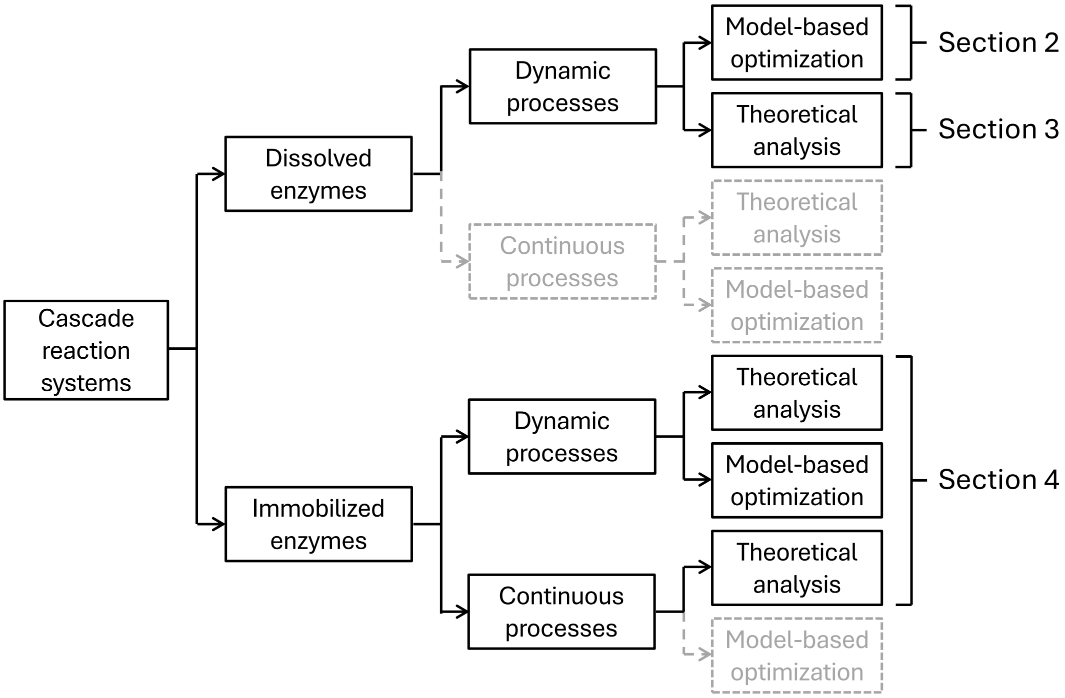

Figure 1: An overview of organization of topics within the dissertation. The gray dashed lines indicate topics that are not covered in the dissertation.

2 Model-based optimization of dynamic processes with dissolved enzymes

2.1 Motivation

Numerous enzymatic cascades were researched and successfully carried out in the laboratory scale in the last years [2, 3, 47, 57–63]. In this section, how kinetic modeling and model-based optimization can be applied for the design of enzymatic cascade reaction system with dissolved enzymes is demonstrated.

Multiple conflicting objectives must be taken into account during the design of an enzymatic cascade reaction process. There is not such a thing as one optimal cascade schedule. Instead, there is a multitude of schedules representing best compromises between the objectives. Cascade developers are aware of these compromises: e.g., improving the space-time yield has to be often paid by increasing the enzyme consumption. A systematic way to deal with conflicting objectives is multi-objective optimization (MOO), also known as multi-criteria optimization or Pareto optimization. It avoids the need for weighing/prioritizing the single objectives and instead identifies a set of best compromises. MOO has been applied throughout process engineering [64–67], including the design of microbial bioreactors [68–71], and enzymatic reactors [51]. In this section MOO is applied to the design of enzymatic cascade batch reactors and the underlying scheduling problem. It is shown that MOO provides advanced decision support for making further experiments, finding bottlenecks, and choosing an optimal process schedule.

The production of α-ketoglutarate via the oxidative pathway of C6 uronic acids is chosen as an application [8]. Kinetics models were fit to the experimental results of Beer et al. [8], enzyme deactivation kinetics were added, and the kinetic model was combined with a reactor model. It will be shown that the combined simulation model provides time profiles agreeing with the respective experimental profiles. Using dynamic optimization, process schedules for the production of α-ketoglutarate are identified. Thereby, three conflicting objectives are considered: space-time yield, enzyme consumption, and cofactor consumption. The optimization parameters comprise the initial concentrations of substrates, enzymes and cofactors, the batch time, as well as the dosing times and amounts of supplemented substrates and enzymes. The set of Pareto-optimal process schedules is determined and serves as decision support for further process design.

2.2 Methodology

2.2.1 Studied system

An *in vitro* metabolic engineering approach for the production of α-ketoglutarate through the oxidative pathway of C6 uronic acids was developed and published by Beer et al. [8]. As shown in Figure 2 a), this enzymatic cascade includes four enzymatic reactions and one non-enzymatic chemical step. First, D-glucuronate is oxidized in a cofactor-dependent manner by uronate dehydrogenase (UDH) from *Agrobacterium tumefaciens* to yield glucaro-1,4-lactone. The heterocyclic ring structure of glucaro-1,4-lactone then opens to yield D-glucarate. D-glucarate is then dehydrated by glucarate dehydratase (GlucD) from *Actinobacillus succinogenes* to yield 5-keto-4-deoxyglucarate. 5-keto-4-deoxyglucarate then reacts with a reaction catalyzed by 5-keto-4-deoxyglucarate dehydratase (KdgD) from *Acinetobacter baylyi* to form ketoglutaric semialdehyde. The final step is another cofactor-dependent oxidation by α-ketoglutaric semialdehyde dehydrogenase (KgsalDH) from *Pseudomonas putida* to yield α-ketoglutarate.

The non-enzymatic reaction (II) has not been described by Beer et al. [8] and was added in the present work because its kinetics are relevant. In the next section, experimental justification is described. In two other similar studies, the kinetics of lactone opening steps were found to be relevant in the work of Shen et al. and Sutiono et al. [9, 72].

The reduced cofactor (NADH) is regenerated by the enzyme NADH oxidase (NOX) from *Lactobaccilus pentosu* to yield its oxidized form (NAD^+), as shown in Figure 2 b). In this reaction, oxygen is required as a second substrate and water is formed as a byproduct.

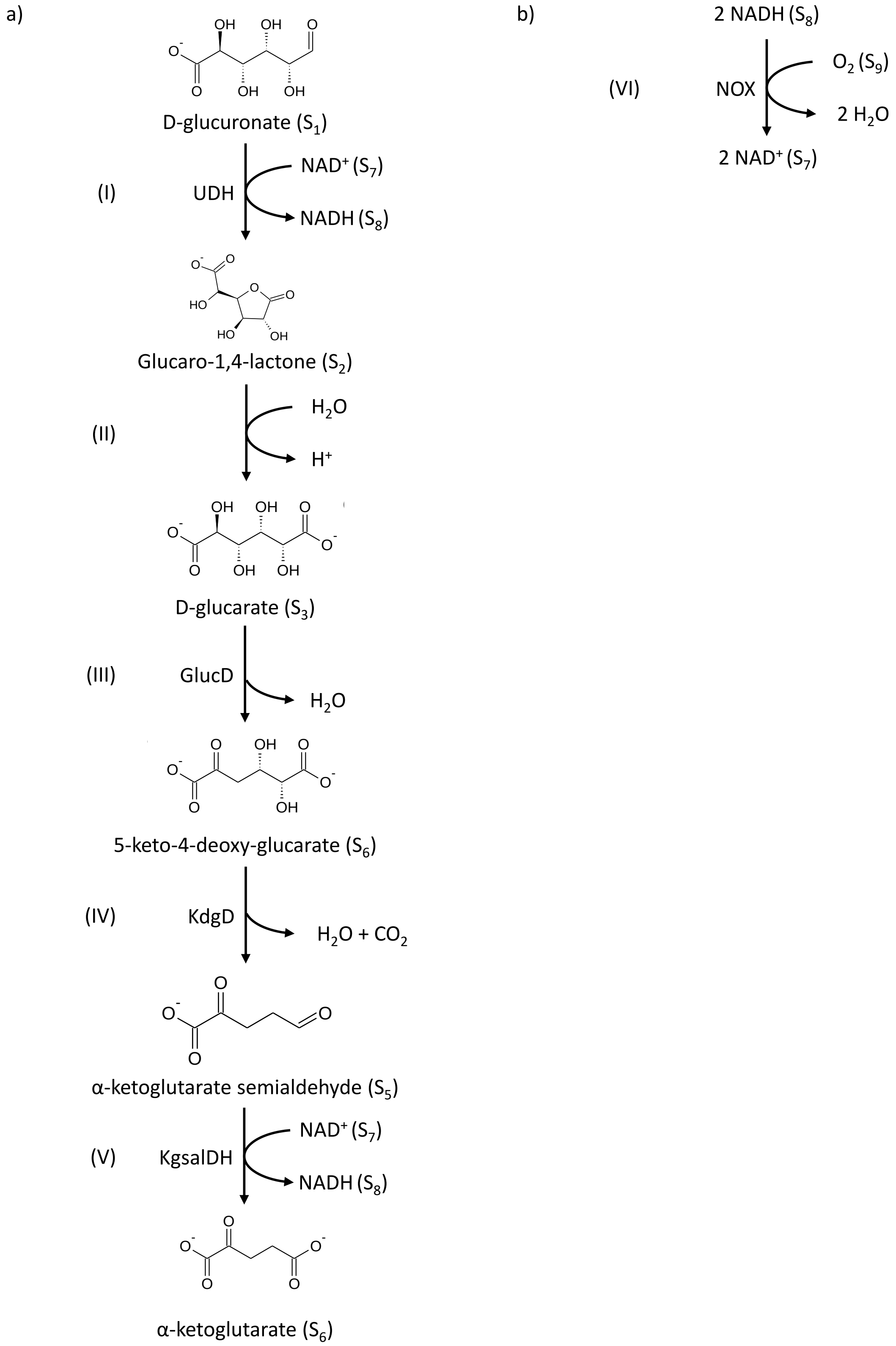

Figure 2: a) The enzymatic cascade reaction for the sythesis of α-ketoglutarate through the oxidative pathway of C6 uronic acids. b) The cofactor regeneration reaction. Each reaction is assigned a Roman nummeral, each substrate is assigned an Arabic nummeral, and each enzyme is assigned an abbreviation of its name.

2.2.2 Assumptions

Before giving the model equations the major assumptions are discussed. An ideal, perfectly mixed, isothermal, batch reactor is assumed. A steady supply of air through the reactor is assumed. The mass transfer of oxygen is modeled with a lumped $k_\mathrm{L}a$ parameter as explained below. All enzymes are assumed to be stable over the entire batch time with the exception of NOX. Regarding the kinetics of the enzymes it is assumed that they behave in the cascade as they do in the kinetic assay experiments of the individual enzyme.

2.2.3 Model equations

Differential balances for the molar concentrations of all substrates, enzymes and cofactors are formulated following the stoichiometry given in Figure 2. With the exception of the cofactor regeneration reaction, the stoichiometry of all reactions is 1:1. The material balances for all substrates are presented with a compact matrix notation in Equation (1). The substrates and reactions are assigned Arabic indices and Roman indices, respectively, while the enzymes are assigned abbreviations of their names as indices. All indices are given in Figure 2. The substrate concentrations, S_i with $i = 1, 2, ..., 9$, are included in vector $\mathbf{s}$. The stoichiometric coefficients are included in matrix $\mathbf{U}$. The reaction rates v_k with $k =$ I, II, ..., VI, are included in vector $\mathbf{v}$. The oxygen mass transfer rate, N_{O_2}, is included in vector $\mathbf{n}$.

$$\frac{d\mathbf{s}}{dt} = \mathbf{U} \cdot \mathbf{v} + \mathbf{n} \tag{1}$$

where

$$\mathbf{s} = \begin{bmatrix} S_1 \\ S_2 \\ S_3 \\ S_4 \\ S_5 \\ S_6 \\ S_7 \\ S_8 \\ S_9 \end{bmatrix}, \ \mathbf{U} = \begin{bmatrix} -1 & 0 & 0 & 0 & 0 & 0 \\ +1 & -1 & 0 & 0 & 0 & 0 \\ 0 & +1 & -1 & 0 & 0 & 0 \\ 0 & 0 & +1 & -1 & 0 & 0 \\ 0 & 0 & 0 & +1 & -1 & 0 \\ 0 & 0 & 0 & 0 & +1 & 0 \\ -1 & 0 & 0 & 0 & -1 & +1 \\ +1 & 0 & 0 & 0 & +1 & -1 \\ 0 & 0 & 0 & 0 & 0 & -\frac{1}{2} \end{bmatrix}, \ \mathbf{v} = \begin{bmatrix} v_\mathrm{I} \\ v_\mathrm{II} \\ v_\mathrm{III} \\ v_\mathrm{IV} \\ v_\mathrm{V} \\ v_\mathrm{VI} \end{bmatrix}, \text{and } \mathbf{n} = \begin{bmatrix} 0 \\ 0 \\ 0 \\ 0 \\ 0 \\ 0 \\ 0 \\ 0 \\ N_{\mathrm{O}_2} \end{bmatrix}.$$

The concentration of enzyme j in its active form is denoted with E^j. It is assumed that UDH, GlucD, KdgD and KGSA do not deactivate during the reaction batch. Thus, they can be fed right at the start and their activity stays constant.

$$\frac{dE^{\mathrm{UDH}}}{dt} = \frac{dE^{\mathrm{GlucD}}}{dt} = \frac{dE^{\mathrm{KdgD}}}{dt} = \frac{dE^{\mathrm{KGSA}}}{dt} = 0 \tag{2}$$

For NOX, deactivation is observed [73, 74]. For this reason, supplementation of active NOX might be optimal. The material balance for active NOX is

$$\frac{dE^{\mathrm{NOX}}}{dt} = -k^{\mathrm{NOX}} \cdot E^{\mathrm{NOX}} + r_{\mathrm{s}}^{\mathrm{NOX}} \tag{3}$$

The deactivation is modeled with a first order decay with constant k^{NOX}. $r_{\mathrm{s}}^{\mathrm{NOX}}$ denotes the supplementation rate of active NOX.

The enzyme-catalyzed reaction steps (III) and (IV) are modeled with a Michaelis-Menten kinetic [75].

$$v_{\mathrm{III}} = \frac{E^{\mathrm{GlucD}} \cdot V_{\mathrm{max}}^{\mathrm{GlucD}} \cdot S_3}{K_3^{\mathrm{GlucD}} + S_3} \tag{4}$$

$$v_{\mathrm{IV}} = \frac{E^{\mathrm{KdgD}} \cdot V_{\mathrm{max}}^{\mathrm{KdgD}} \cdot S_4}{K_4^{\mathrm{KdgD}} + S_4} \tag{5}$$

The enzyme-catalyzed steps (I) and (V), which involve a cofactor, are modeled with a Ping-Pong Bi Bi kinetic [76].

$$v_{\mathrm{I}} = \frac{E^{\mathrm{UDH}} \cdot V_{\mathrm{max}}^{\mathrm{UDH}} \cdot S_1 \cdot S_7}{K_7^{\mathrm{UDH}} \cdot S_7 + K_1^{\mathrm{UDH}} \cdot S_1 + S_7 \cdot S_1} \tag{6}$$

$$v_{\mathrm{V}} = \frac{E^{\mathrm{KgsalDH}} \cdot V_{\mathrm{max}}^{\mathrm{KgsalDH}} \cdot S_5 \cdot S_7}{K_7^{\mathrm{KgsalDH}} \cdot S_7 + K_5^{\mathrm{KgsalDH}} \cdot S_5 + S_7 \cdot S_5} \tag{7}$$

In the above and the following equations, v_k are the reaction rates, S_i are the substrate concentrations, E^j are the active enzyme concentrations, V_{max}^j is the specific maximum reaction rate of enzyme j, and K_i^j are the kinetic parameters. The rate of the opening of the glucaro-1,4-lactone is modeled with first order kinetics with rate constant k_{II}.

$$v_{\mathrm{II}} = k_{\mathrm{II}} \cdot S_2 \tag{8}$$

The rate of the cofactor regeneration step is modeled with a Michaelis-Menten kinetic [75].

$$v_{\mathrm{VI}} = \frac{E^{\mathrm{NOX}} \cdot V_{\mathrm{max}}^{\mathrm{NOX}} \cdot S_8}{K_8^{\mathrm{NOX}} + S_8} \tag{9}$$

An alternative cofactor regeneration system was also investigated. Sudar et al. [77] has suggested a different NOX enzyme from *Lactococcus lactis* for cofactor regeneration and have given its rate by

$$v_{\mathrm{VI}}^{'} = \frac{E^{\mathrm{NOX}'} \cdot V_{\mathrm{max}}^{\mathrm{NOX}'} \cdot S_8 \cdot S_9}{(K_8^{\mathrm{NOX}'} + S_8 \cdot (1 + \frac{S_7}{K_7^{\mathrm{NOX}'}})) \cdot (K_9^{\mathrm{NOX}'} + S_9)} \tag{10}$$

v_{VI} (Equation (9)) is used in the parametrization using lab scale experiments of Beer et al. [8]. v_{VI}' (Equation (10)) is used in the process optimization.

The mass transfer of oxygen is modeled assuming that transport through the liquid-phase film of the air bubbles to be rate limiting:

$$N_{\mathrm{O}_2} = k_{\mathrm{L}}a \cdot (S_9^* - S_9) \tag{11}$$

$k_{\mathrm{L}}a$ is the volumetric mass transfer coefficient and S_9^* is the equilibrium solubility of oxygen in the reaction solution. The solubility is calculated from Henry's law. Henry's constant for oxygen in pure water at 25°C and 1 atm was used [78].

$$p_{\mathrm{O}_2} = (0.774\,\mathrm{m}^3\,\mathrm{atm}\,\mathrm{gmol}^{-1}) \cdot S_9^* \tag{12}$$

p_{O_2} is the partial pressure of oxygen, in the air bubbles. In the simulation the partial pressure p_{O_2} was fixed to 0.2099 atm.

2.2.4 Numerical implementation

The model was implemented in Pyomo (Version 5.1) [79–81], a symbolic simulation and optimization toolbox for Python. The finite difference discretization scheme (implicit Euler) [79, 82] and the IPOPT solver (Version 3.11.1) [83] were used. NOX supplementation was modeled using smooth functions instead of sharp impulses or steps:

$$r_{\mathrm{s}}^{\mathrm{NOX}} = \sum_{l=1}^{3} \{A_{\mathrm{k}} \cdot [\tanh(\frac{100 \cdot (t - t_{\mathrm{l}})}{t_{\mathrm{f}}}) - \tanh(\frac{100 \cdot (t - (t_{\mathrm{l}} + 4\mathrm{min}))}{t_{\mathrm{f}}})]\} \tag{13}$$

Up to 3 additions were allowed. The additions start at time point t_l, have a duration of 4 minutes, and a magnitude of A_l. t_l and A_l are optimization variables. 100 is a shape factor.

2.2.5 Parametrization

The parameters of the enzymatic reaction rate equations (4)-(7) and (9) were fitted to the data of individual enzyme assay experiments from Beer et al. [8] minimizing the least squares of the deviations in the rates. Plots comparing the experimental data with the fitted curves are given in the supplementary material. The kinetic parameters are presented in Table 1.

Table 1: The kinetic parameters of the enzymatic reactions and their 95% confidence interval.

j	$V^j_{\mathrm{max}}/(\mathrm{U/mg})$	i	K^j_i/mM
UDH	221.331 ± 7.254	1	0.0780 ± 0.0447
		7	0.5884 ± 0.0052
GlucD	8.876 ± 0.651	3	0.2945 ± 0.0695
KdgD	5.109 ± 0.457	4	0.4652 ± 0.1333
KgsalDH	40.701 ± 2.360	5	0.4812 ± 0.0342
		7	0.1760 ± 0.0952
NOX	38.872 ± 2.992	8	0.0375 ± 0.0090
NOX'	16.409 ± 0.717*	7	0.1420 ± 0.0450*
		8	0.0050 ± 0.0010*
		9	0.0045 ± 0.0019*

* The kinetic parameters for NOX' were taken from Sudar et al. [77].

The parameter k^{NOX} quantifying the deactivation of NOX was fitted to an experiment in a bench scale bubble reactor, c.f. Appendix A for details, and resulted in 0.03 ± 0.01 min^{-1}. The rate constant k_{II} was fitted to a cascade experiment (Figure 5 (B) in [8]) from Beer et al. [8]. Before used in the fit, the experimental data were reconciled as described in the supplementary material. k_{II} was determined to be $0.013 \pm 4 \cdot 10^{-8}$ min^{-1}. A comparison of reconciled experimental data and the final simulated model is shown in Figure 3. A good fit between model and experiment is observed.

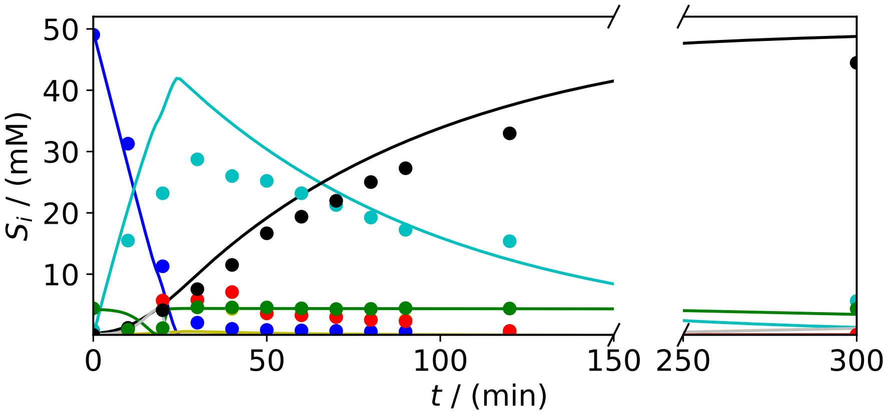

Figure 3: Comparison of the the experimental data and the model for a cascade experiment conducted in the bench scale batch reactor. The experimental data points: ● D-glucuronate, ● glucaro-1,4-lactone, ● D-glucarate, ● 5-keto-4-deoxy-glucarate, ● α-ketoglutarate semialdehyde, ● α-ketoglutarate, ● NAD$^+$, ● NADH. The substrate concentration trajectories calculated by the model: — D-glucuronate, — glucaro-1,4-lactone, — D-glucarate, — 5-keto-4-deoxy-glucarate, — α-ketoglutarate semialdehyde, — α-ketoglutarate, — NAD$^+$, — NADH.

2.2.6 Multi-objective optimization

The focus of this section is a technical, dynamic process that produces α-ketoglutarate using the cascade presented above. The process is done in a stirred-tank reactor with air gassing at pH 7, 25°C, and 1 bar. Two simplifying assumptions are used at this early stage of process design. The air gassing system is not specified in detail. Instead, it is assumed that $k_{\mathrm{L}}a$ values in the range 1.2-15 min^{-1} are technically attainable [78] and consider both limits in separate cases studies. Further, the product space-time yield is maximized and the raw material costs are minimized while neglecting investment and fixed operating costs. Under these assumptions, the size of the reactor becomes irrelevant, and focusing on titers instead of absolute amounts of substrates and enzymes is possible.

Control variables of the process are the titers of D-glucuronate, cofactor, and the five enzymes and their supplementation schedules. Except for NOX, these compounds do neither deactivate nor inhibit any step. Thus, the respective compounds are added at the beginning of the process without any caveats. For NOX, both initial addition or later supplementation at up to three freely chosen time points is allowed, cf. Equation (13). Further, the running time t_{f} of the batch is a control variable. It is assumed that cofactors and enzymes can be used only in one batch and not recycled. Between two batches, a preparation time t_p of 30 min is needed, during which the batch reactor is not available.

Three conflicting objectives $\mathit{\Phi}^w$ are considered in the optimization:

$$\mathit{\Phi}^{\mathrm{STY}} = \frac{S_6(t_\mathrm{f})}{t_\mathrm{f} + t_\mathrm{p}} \tag{14}$$

$$\mathit{\Phi}^{\mathrm{EC}} = \frac{\sum\limits_j \{E^j(0)\} + \int_0^{t_\mathrm{f}} r_\mathrm{p}^{\mathrm{NOX}}\,\mathrm{d}t.}{t_\mathrm{f} + t_\mathrm{p}} \tag{15}$$

$$\mathit{\Phi}^{\mathrm{CC}} = \frac{S_7(0)}{t_\mathrm{f} + t_\mathrm{p}} \tag{16}$$

$\mathit{\Phi}^{\mathrm{STY}}$ quantifies the space-time yield as the final product titer divided by the total duration of one batch, including running and preparation time. It shall be maximized. The enzyme consumption $\mathit{\Phi}^{\mathrm{EC}}$ quantifies the space-time consumption of enzymes. Due to a lack of reliable data, all enzymes are treated as equally costly. $\mathit{\Phi}^{\mathrm{CC}}$ quantifies the space-time consumption of cofactor NAD$^+$. $\mathit{\Phi}^{\mathrm{EC}}$ and $\mathit{\Phi}^{\mathrm{CC}}$ shall be minimized. Instead of prioritizing or weighing the objectives, the set of best compromises between them is determined. Such a best compromise is a Pareto-optimal solution that is defined as follows: an improvement in one of the objectives is only possible by accepting a deterioration in at least one other objective. There are several methods and algorithms to determine Pareto-optimal solutions systematically [64]. In the present work, the epsilon constraint method is used. One Pareto-optimal solution is obtained by solving the following single objective optimization problem:

$$\begin{aligned} &\max \mathit{\Phi}^{\mathrm{STY}} \\ &\mathit{\Phi}^{\mathrm{EC}} \leq \epsilon^{\mathrm{EC}} \\ &\mathit{\Phi}^{\mathrm{CC}} \leq \epsilon^{\mathrm{CC}} \end{aligned} \tag{17}$$

The single objective $\mathit{\Phi}^{\mathrm{STY}}$ is maximized. The other objectives (which have to be minimized) are constrained by some limit ϵ^m from above. The solution to the problem (17) is guaranteed Pareto-optimal [64]. Multiple Pareto-optimal solutions are obtained through systematic variation of the ϵ^m bounds in problem (17). They are members of the Pareto-optimal set, also called Pareto frontier.

During all optimizations, additional inequality constraints are imposed to limiting the considerations to practically relevant operations. The solubility of the substrates should not exceed their solubility limit.

$$S_i(0) \leq 1,000\,\mathrm{mM} \tag{18}$$

Further, the running time of the batch is limited to practically reasonable values:

$$t_\mathrm{f} \leq 50,000\,\mathrm{min} \tag{19}$$

Finally, the yield is also constraint:

$$\frac{S_6(t_\mathrm{f}) - S_6(0)}{S_1(0)} \geq 95\% \tag{20}$$

2.3 Results and discussion

2.3.1 Pareto-optimal process schedules

The results of the design of a dynamic reaction process for the production of α- ketoglutarate via model-based optimization are presented and discussed here. Pareto-optimal reaction process schedules were determined using the methodology previously described. The results are based on the developed model and were derived by solving the discussed optimization problem.

Results for two cases were determined ($k_\mathrm{L}a$ = 1.2 min^{-1} in Figure 4 and $k_\mathrm{L}a$ = 15 min^{-1} in Figure 5). For every case, 28 Pareto-optimal solutions that serve as sampling points of the Pareto frontier were calculated. The numerical values for objectives and all control variables are listed in tables in Appendix A. The trade-offs between the objectives are shown in Figures 4a) and 5a) for the $k_\mathrm{L}a$ = 1.2 min^{-1} and $k_\mathrm{L}a$ = 15 min^{-1} cases, respectively. The Pareto frontiers are 2D surfaces in the 3D objective space. The Pareto frontiers are visualized as a contour plot using Φ^CC as the level parameter. The Pareto frontier divides the objective space into two regions: an infeasible region (top left in Figures 4a) and 5a)) and a dominated region (lower right in Figures 4a) and 5a)) that contains feasible solutions that are not best compromises. For $k_\mathrm{L}a$ = 1.2 min^{-1} (Figure 4a)), the trade-offs between all three objectives are visible. The more enzymes are consumed, the higher the space-time yield gets. This can be seen when, for example, comparing points A and B. Even in an extreme compromise, where an unlimited supply of enzymes is allowed, there is a limit for the space-time yield. In these solutions, the oxygen transfer becomes rate-limiting. Further addition of enzymes does not improve the situation significantly.

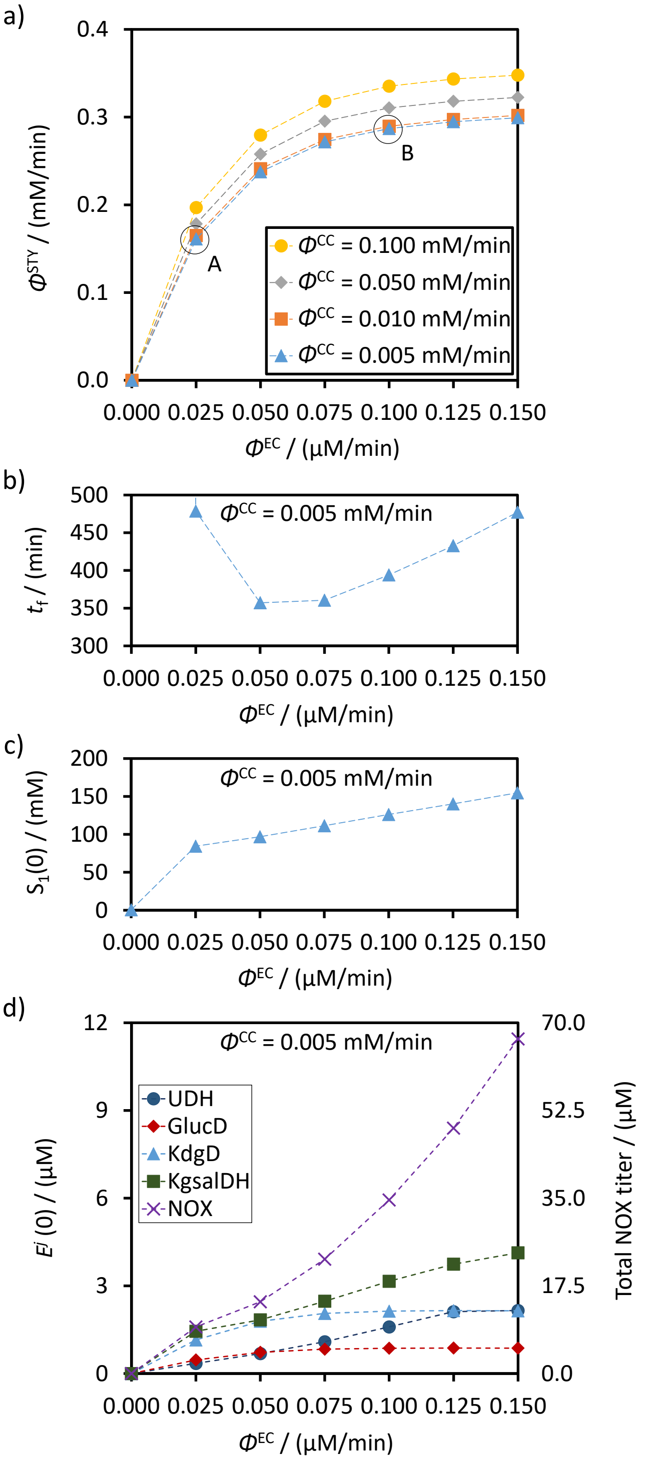

Figure 4: a) The Pareto frontiers for four different cofactor consumptions for the Sudar et al. [77] cofactor regeneration system with $k_La = 1.2\ \text{min}^{-1}$. b) The optimal values for the control variable t_f for each point in the $\Phi^{CC} = 0.005$ mM/min Pareto frontier. c) The optimal values for the control variable $S_1(0)$ for each point in the $\Phi^{CC} = 0.005$ mM/min Pareto frontier. d) The optimal values for the total enzyme titers for each point in the $\Phi^{CC} = 0.005$ mM/min Pareto frontier. NOX titers are read on the right axis. The titers of all other enzymes are read on the left axis.

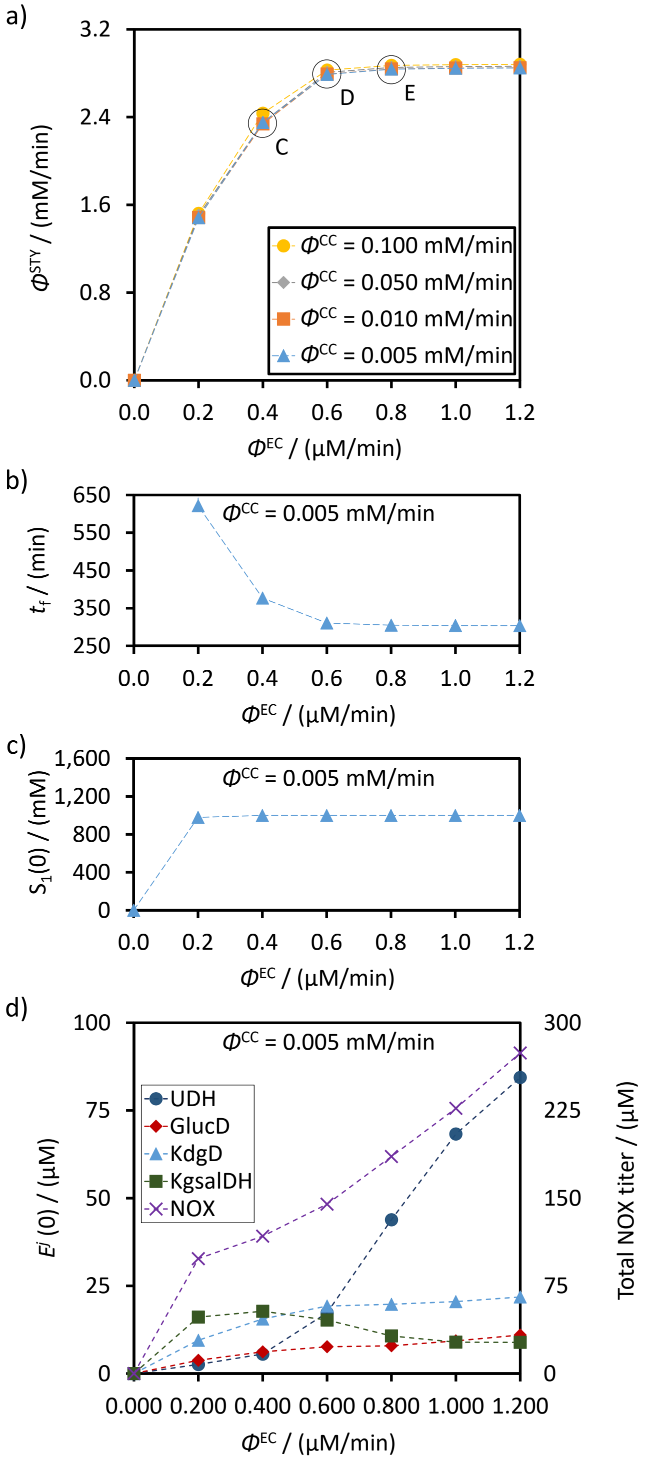

Figure 5: a) The Pareto frontiers for four different cofactor consumptions for the Sudar et al. [77] cofactor regeneration system with $k_\mathrm{L}a = 15\ \mathrm{min}^{-1}$. b) The optimal values for the control variable t_f for each point in the $\Phi^\mathrm{CC} = 0.005$ mM/min Pareto frontier. c) The optimal values for the control variable $S_1(0)$ for each point in the $\Phi^\mathrm{CC} = 0.005$ mM/min Pareto frontier. d) The optimal values for the total enzyme titers for each point in the $\Phi^\mathrm{CC} = 0.005$ mM/min Pareto frontier. NOX titers are read on the right axis. The titers of all other enzymes are read on the left axis.

In the $k_{\mathrm{L}}a = 1.2$ min^{-1} case (Figure 4a)), the space-time yields are significantly lower than in the $k_{\mathrm{L}}a = 15$ min^{-1} case (Figure 5a)). Due to limited oxygen supply, the regeneration of the cofactor is slow, and the initial provision of the cofactor measured by Φ^{CC} is decisive for high space-time yields. Tha maximum space-time yield that can be reached in this case is 0.35 mM/min. If the oxygen transport increases ($k_{\mathrm{L}}a = 15$ min^{-1} in Figure 5a), then much higher space-time yields are feasible. In the $k_{\mathrm{L}}a = 15$ min^{-1} case, changing the initial cofactor concentration has a minor effect. The regeneration is more critical for the availability of the cofactor than the initial cofactor concentration. The maximum space-time yield that can be reached in this case is 2.88 mM/min.

The optimal values of some selected control variables are presented beneath the Pareto frontiers in Figures 4 and 5. All of these values correspond to the $\Phi^{\mathrm{CC}} = 0.005$ mM/min Pareto solutions. In Figures 4b) and 5b) the optimal running times, t_{f} are shown. In Figures 4c) and 5c), the optimal initial D-glucuronate titers, $S_1(0)$ are shown. Finally, in Figures 4d) and 5d), the optimal initial enzyme titers, $E^j(0)$, for UDH, GlucD, KdgD and KgsalDH and the total NOX titer, including supplementation are shown. The initial titers for the first four enzymes are read on the left y-axis while the total NOX titer is read on the right y-axis.

In Figure 4b), the times initially decrease and then increase again with rising Φ^{EC}. The initial decrease is because when more enzymes speed up the reactions the required 95% yield is reached in a shorter time. The increase at high Φ^{EC} is a result of the slow oxygen mass transfer rate. When Φ^{EC} become larger than 0.075 mM/min it is advantageous to allow the reaction process to run for longer times to allow enough oxygen to be transferred back to the reaction solution in order to convert more D-glucuronate. This is shown bellow in more detail. By contrast, in Figure 5b), the running times keep decreasing at higher enzyme consumption. Gradually, a minimum value is approached. This minimum value is a result of the first order kinetic of the lactone opening step and it can not be improved by adding more enzymes.

In Figure 4c), the optimal initial D-glucuronate titers are a lot less than the maximum allowed concentration (1,000 mM). This is once again due to the slow oxygen transfer rate. When, a higher enzyme consumption is allowed more substrate is converted. In Figure 5c), the optimal initial D-glucuronate titers are equal to the solubility limit in all solutions. The large rate of oxygen mass transfer allows for conversion of high amounts of substrates quickly and it's always advantageous to convert the maximum amount of substrate possible.

In Figure 4d), as higher enzyme consumption is allowed the titers of UDH, KgsalDH and NOX rise. This is because cofactor regeneration is a limiting factor due to slow oxygen transfer. Therefore the optimizer compensates by adding more NOX and UDH, KgsalDH respectively. The titers of GlucD and KdgD remain unchanged after an enzyme consumption of 0.075 mM/min. Since oxygen transfer and cofactor regeneration are the rate limiting steps, the optimizer selects all enzymes that accelerate these two steps to supplement. Instead of adding more of GlucD and KdgD it allows them to act for a longer time by increasing the running time of the batch reactor. In Figure 5d), all enzyme titers increase as a larger enzyme consumption is allowed except for KgsalDH, which decreases after 0.4 mM/min. This decrease is because the optimizer applies a different strategy after 0.4 mM/min. This is discussed further in Appendix A.

The results of the optimizations also include the process schedules (when to add NOX etc.) and simulated time profiles of every single Pareto-optimal solution. Detailed inspection yields that solutions from the Pareto frontier differ not only quantitatively but also qualitatively from one another. This is shown in Figures 6 and 7, in which the simulations of solutions A and B of Figure 4 are compared (respective profiles for the solutions C and D of Figure 5 are given in the Appendix A).

In solution B, in Figure 7, the oxygen concentration is close to zero for the most part. This means that the oxygen transfer, and therefore the cofactor regeneration, is the rate limiting step for the enzymatic cascade. This is quite different in solution A, in Figure 6, where the oxygen concentration is significantly larger for most of the time. When the reaction rate is limited by the reaction kinetics, the profiles of the substrates are generally curved as in Figure 6. On the other hand, when oxygen transfer is rate limiting, the profiles of the substrates are generally straight lines, as in Figure 7. This is because the reaction kinetics are modeled with the Michaelis-Menten kinetics, while the oxygen transfer is modeled with a linear equation.

While the oxygen concentration is low in solution B, the optimizer chose to invest more NOX enzyme than in solution A, cf. higher spikes in the NOX time profiles. Consequently, B has a higher enzyme consumption than A, cf. Figure 4, but also a higher space-time yield.

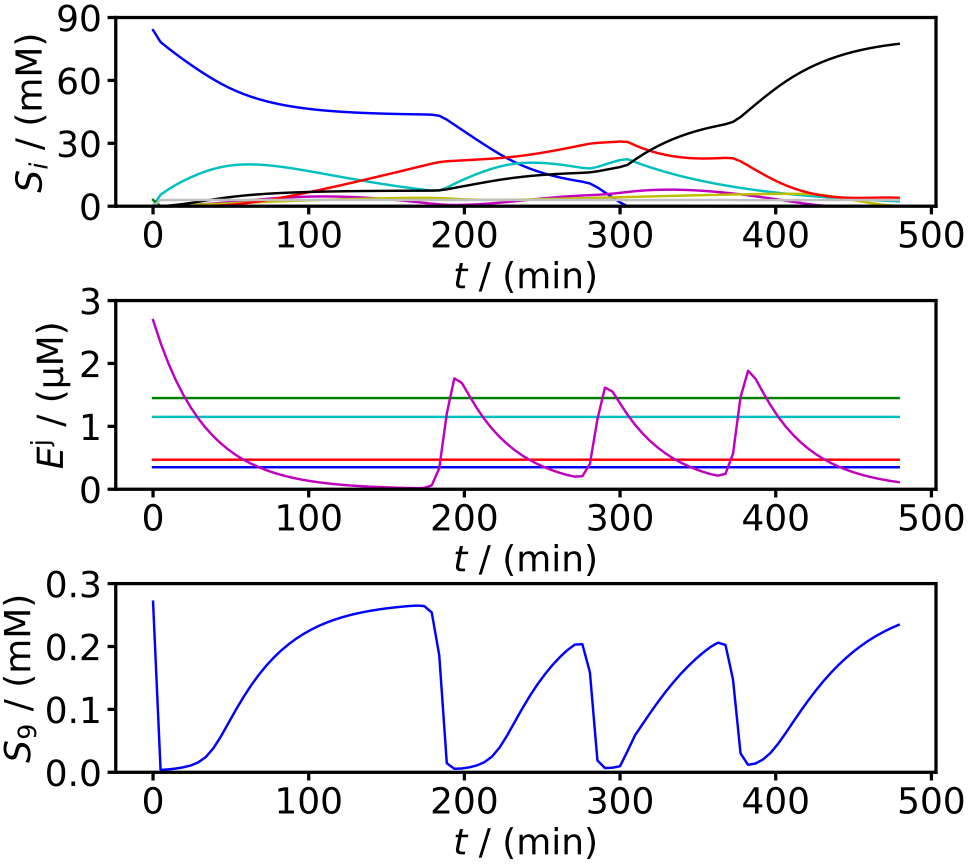

Figure 6: Time profiles of solution A of Figure 4a) ($\Phi^{\mathrm{EC}} = 0.025$ μM/min and $\Phi^{\mathrm{CC}} = 0.005$ mM/min). First plot: The substrate concentration profiles, — D-glucuronate, — glucaro-1,4-lactone, — D-glucarate, — 5-keto-4-deoxy-glucarate, — α-ketoglutarate semialdehyde, — α-ketoglutarate, — NAD$^+$, — NADH. Second plot: The enzyme concentration profiles, — UDH, — GlucD, — KdgD, — KgsalDH, — NOX. Third plot: The oxygen concentration profile.

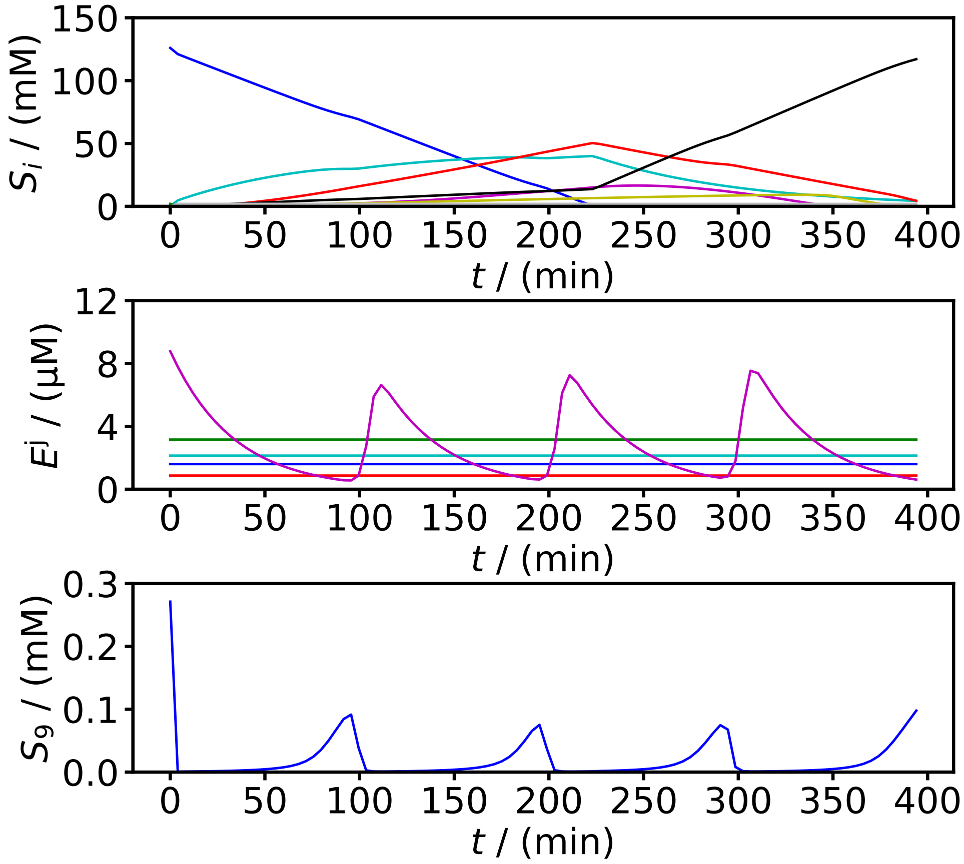

Figure 7: Time profiles solution B of Figure 4a) ($\Phi^{\mathrm{EC}} = 0.100\ \mu\mathrm{M/min}$ and $\Phi^{\mathrm{CC}} = 0.005$ mM/min. First plot: The substrate concentration profiles, — D-glucuronate, — glucaro-1,4-lactone, — D-glucarate, — 5-keto-4-deoxy-glucarate, — α-ketoglutarate semialdehyde, — α-ketoglutarate, — NAD$^+$, — NADH. Second plot: The enzyme concentration profiles, — UDH, — GlucD, — KdgD, — KgsalDH, — NOX. Third plot: The oxygen concentration profile.

2.3.2 Discussion of the applied method

The Pareto frontier offers great decision support for the selection of a process schedule. For example, consider the solutions marked D and E in Figure 5a). If one would maximize only the single objective space-time yield, then E would be better than D. However, since the Pareto frontier is relatively flat in that region, solution D is also very attractive. It saves a decent amount of enzymes at a slight - and thus possibly acceptable - deterioration of the space-time yield. Without the overview provided by the Pareto frontier, the designer would have no feeling for these trade-offs.

Even though all solutions on the Pareto frontier represent best compromises, they may differ significantly from one another as seen in Figures 6 and 7. Different process strategies are applied in different Pareto optimal solutions. The strategies are adjusted each time to maximize the space-time yield under the $k_{\mathrm{L}}a$, Φ^{EC} and Φ^{CC} constraints in effect. Comparing the different strategies provides insight in the cascade itself and helps better understand the Pareto frontier. Without the systematic and automated way as done in this study, obtaining these information by experiment and simulation alone, would be rather tedious and incomplete.

The optimization results are based on the model, thus their validity depends on the models uncertainty. To evaluate the impact of the uncertainty, an analysis was performed, where the sensitivity of our parametrization was quantified on the space-time yield calculated by our model. The details are described in the supplementary material. In some cases, the space-time yield varied between -75% and +2% of the space-time yields presented in Figures 4 and 5. This shows that once a process schedule and a process technology (sparging system, stirrer, etc.) are selected, the model parameters should be validated again. Even though -75% sounds like a lot, one should bear in mind that the space-time yield could be optimized again for the changed parameter set damping the deterioration in the space-time yield. In future work, robust multi-objective optimization as presented by Bortz et al. [84] could be considered.

The results described above provide an excellent base for the subsequent steps of process design. On the one hand, the Pareto frontier implicitly provides an experimental design for further validation and tuning of the model. By focusing on multiple best compromises between the objectives, the resulting model is expected to be accurate right where it matters and robust even if priorities or prices change. In particular, a validation/improvement of the model would be interesting in a large scale technical reactor. With the updated model the frontier could be updated leading to a target-focused iteration. Such an iteration with larger technical reactors was however out of the scope for the cascade studied in the present work.

On the other hand, the Pareto frontier supports the decision-maker in the follow-up steps toward realizing the process. Even though detailed cost functions might not be available yet, the decision-maker can select a solution in the knee of the Pareto frontier (i.e., the region of strong curvature and not in the flat parts of the frontier) and move on. Even if the Pareto frontier shows no sharp knee, it provides a robust set of optimal compromises to focus. The optimization does not have to be repeated from scratch when the objectives are concretized, e.g., by introducing monetary cost functions.

3 Theoretical analysis of dynamic processes with dissolved enzymes

3.1 Cofactor regeneration and boosting by intermediates

Some steps of enzymatic cascades are cofactor-dependent, i.e., they require a cofactor to exhibit catalytic activity. The cofactor exists either in an oxidized or a reduced form, e.g., NAD^+ and NADH. During a reductive, cofactor-dependent, enzyme-catalyzed reaction, the oxidized form of the cofactor is reduced to yield the reduced form of the cofactor. During an oxidative cofactor-dependent catalyzed reaction, the opposite happens. The price of the cofactors is usually high, and using them in stoichiometric amounts is not possible. Therefore, often, an effective cofactor regeneration system must be in place. This is often achieved by having the same number of reduction and oxidation steps in the cascade. This type of cascades are often referred to as redox cascade reactions. Many redox cascades have been developed in the past few years [4, 10, 56, 85–89].

Sutiono et al. developed a method that increases the productivity of redox enzymatic cascades called boosting by intermediates (BBI). Small amounts of intermediates were added at the start of the reaction process to increase the space-time yield and reduce the amount of cofactor in a six-step, redox enzymatic cascade [56]. It was demonstrated that BBI has the potential to increase the productivity of systems of redox enzymatic cascade reactions and decrease their cost by reducing the titer of enzymes or cofactors required to reach the same space-time yield.

In the present work, we study the theory behind the phenomen BBI along more examples of redox cascades and explain in detail how BBI works. We uncover which intermediates boost and which do not. Further, we quantify the boosting effect and answer the question how much intermediate has the same effect as adding a certain amount of cofactor. In this section, the fundamentals and used methods are presented. All results, including a formal definition of BBI and several theorems on BBI are given in the results. The proofs of the theorems are given in the Appendix B.

3.2 Theorems on BBI

We study the chemical reaction networks (CRN) of four exemplary redox enzymatic cascades, which are illustrated in Figure 8. CRN a) corresponds to the enzymatic cascade developed by Gargiulo et al. for the production of cyclohexanol, b) to the one developed by Sutiono et al. for the production of 1,2,4-butanetriol, and c) to one developed by Guterl et al. for the production of ethanol [2, 4, 55, 56]. The fourth example, CRN d) does not correspond to any developed *in vitro* cascade (to the best of our knowledge) but might be developed in the future. Note that we limit our study to cascades with one educt and one product, that start with a cofactor-dependent step and require only one type of cofactor with two forms (oxidized and reduced).

We define BBI along the simplest possible redox neutral cascade shown by CRN a). Suppose we initially add 250 mM of substrate S_1 and 4 mM of cofactor c_1, which is the oxidized form NAD$^+$ of the cofactor. If the enzymes have Michaelis-Menten-like kinetics, then it is reasonable to assume that the kinetic of the first step is of zeroth order with respect to S_1 (titers larger than the respective K_m lead to saturation) and first order with respect to c_1. The subsequent steps, where only small substrate concentrations are present, can be approached with first-order kinetics with respect to the respective substrates and cofactors. Solving the resulting differential material balances for typical values of kinetic constants yields the time profiles as shown in Figure 9. The qualitative profile is very typical of redox neutral cascades: the first substrate is consumed almost linearly, the final product rises also almost linearly. The intermediate (here S_2) assumes a small and nearly constant concentration after a short initial phase. The intermediate and the cofactors (oxidized and reduced form) reach a quasi steady-state soon after the start of the reaction period and stay there until small concentrations of raw material are left.

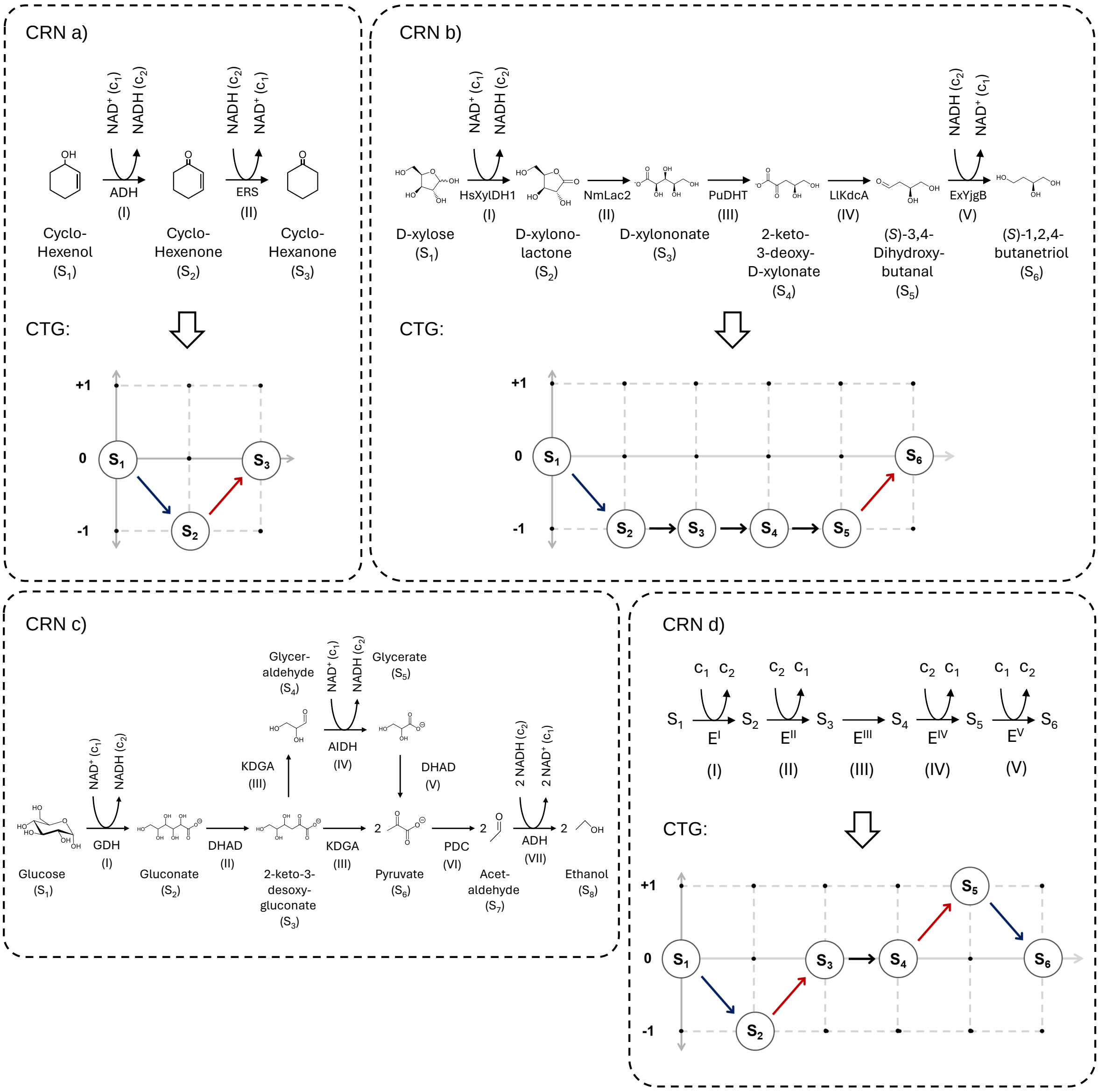

Figure 8: Chemical reaction networks (CRN) and cofactor trajectory graphs (CTG) studied in the present work. For clarity, protons and molecules of CO_2 and H_2O that are acquired or released in the reactions are not shown.

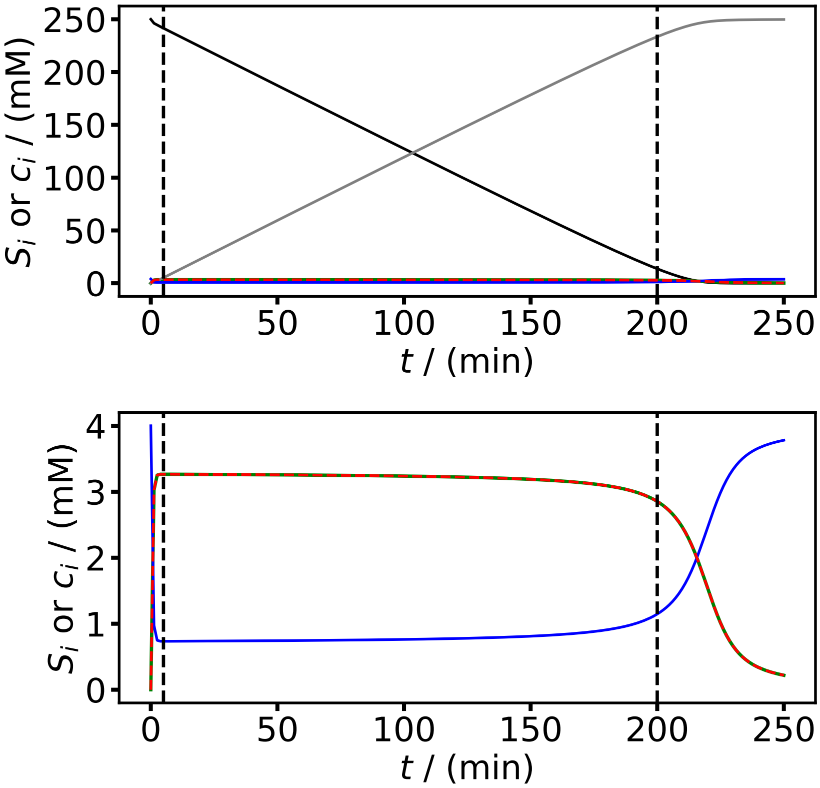

Figure 9: Simulation of the concentration profiles of CRN a) The model equations and kinetic parameters for the model of CRN a) are given in the Appendix B. The lower panel shows a zoom in the y-axis. The dashed lines show the quasi steady state period. — S_1, — S_2, — S_3, — c_1, - - - c_2.

Simulations and experiments (e.g., see [56]) with other redox neutral cascades reveal similar qualitative behavior. (We show simulations of the other CRNs in the Appendix B.) The intermediates can be seen as a "bottleneck" in the overall reaction progress. Their concentration cannot surpass the initial cofactor concentration for stoichiometric reasons. Further, their small concentration slow all reaction steps that have them as substrate. Adding intermediates will increase their concentration in quasi steady-state and thus accelarate the overall cascade. It will also increase the quasi steady-state concentration of the cofactor to a more favorable level, e.g., for a cascade that starts with a reductive step it will increase the quasi steady-state concentration of the oxidized form of the cofactor. Note that the amount of intermediates added at time zero will not be converted to product but will rather stay in one of the intermediate chemical forms. We define boosting by intermediates as follows.

Definition 1: Boosting by intermediates.
Given is an enzymatic cascade reaction that includes at least one intermediate. The cascade reaction is carried out twice, the initial conditions (i.e., initial enzyme titers, titer of the first substrate, and cofactor titers) are kept the same. The first time, no intermediates are added. The second time, some intermediate is added in some amount at the start of the cascade. We define that the intermediate boosts if

$$\underbrace{\int_0^{t_\mathrm{f}} -\frac{dS_1}{dt}\,dt}_{\text{no intermediate added}} < \underbrace{\int_0^{t_\mathrm{f}} -\frac{dS_1}{dt}\,dt}_{\text{intermediate added}} \tag{21}$$

Therein, $\frac{dS_1}{dt}$ (a negative number) is the rate of change of the concentration of the first substrate S_1 that participates in a cofactor-dependent reaction. Its integral over time t from time 0 till final time t_f yields the totally consumed titer of S_1 till time t_f. Boosting by intermediate happens when S_1 is consumed faster.

The decision to integrate the rate of change of the initial substrate of the cascade and not that of the product is not arbitrary. To illustrate this, imagine a cascade independent of cofactors. Adding intermediates to the reaction will - at least for a short time - boost the productivity of the cascade in a trivial way: The added intermediate will react to the product boosting its production. Such an effect is not what we understand as BBI. We define BBI only if adding the intermediate has a feedback effect on the rate of consumption of another substrate upstream.

Even if one intermediate boosts an enzymatic cascade, another might not. In some cases, an intermediate might even delay a cascade reaction. The key to understanding which intermediates boost and which do not is the characteristic equation, which is defined as follows.

Definition 2: Characteristic equation.
The characteristic equation is an equation derived from the material balance connecting the rate of change of the concentration of the oxidized form of the cofactor $\frac{dc_1}{dt}$ with a linear combination of the concentrations of intermediates $\frac{dS_i}{dt}$. For a cascade with one educt and one product that contains n substrates in total, let $\mathcal{I} = \{2, .., n-1\}$ be the set of all intermediates of the cascade and x_i an integer number, the characteristic equation can then be written as follows:

$$\frac{dc_1}{dt} = \sum_{i \in \mathcal{I}} x_i \cdot \frac{dS_i}{dt} \tag{22}$$

The characteristic equations of the four CRNs in Figure 8 are shown in Equations (23) - (26):

$$\frac{dc_1}{dt} = -\frac{dS_2}{dt} \tag{23}$$

$$\frac{dc_1}{dt} = -\frac{dS_2}{dt} - \frac{dS_3}{dt} - \frac{dS_4}{dt} - \frac{dS_5}{dt} \tag{24}$$

$$\frac{dc_1}{dt} = -\frac{dS_2}{dt} - \frac{dS_3}{dt} - \frac{dS_5}{dt} - \frac{dS_6}{dt} - \frac{dS_7}{dt} \tag{25}$$

$$\frac{dc_1}{dt} = -\frac{dS_2}{dt} + \frac{dS_5}{dt} \tag{26}$$

The characteristic equations show the dependence of the rate of change of the cofactor concentration on the rate of change of the concentration of certain intermediates. When all intermediates appear with negative coefficients, then all intermediates are constrained and cannot exceed the initial cofactor concentration during the reaction process if BBI is not used. If some interemdiates do not appear in the characteristic equation they are not constrained in the same way. When some intermediates appear with positive and some with negative coefficients in the characteristic equation, the behavior of the cascade is more complex and whether intermediates accumulate depends on the kinetic parameters. The characteristic equation can be used to deduce which intermediates boost as follows.

Theorem 1: Identification of intermediates that boost for any redox neutral cascade.
For a redox neutral cascade that reaches a quasi steady-state, finding which intermediates boost can be done through the characteristic equation. If the cascade starts with a cofactor-reducing step and the characteristic equation contains all intermediates with negative coefficients x_i then all intermediates boost the cascade. If the characteristic equation contains both intermediates with positive, negative and/or zero coefficients the answer depends on the relative value of the kinetic parameters. In the case that an oxidative or neutral step whose educt appears in the characteristic equation is rate limiting, all intermediates with a coefficient of the same (opposite) sign as the coefficient of that educt boost (delay) the cascade. In the case that a reductive step whose educt appears in the characteristic equation is rate limiting, all intermediates with a negative (positive) coefficient boost (delay) the cascade.

Note that the characteristic equation does not include the first substrate or the product of the cascade, it only includes intermediates. Obtaining the characteristic equation for a certain redox neutral cascade is the task of finding the coefficients x_i. A method for deriving the coefficients is given below.

Method 1: Obtaining the characteristic equation.
Let the differential material balance for all substrates except the first one of a cascade reaction with n substrates be written as follows: $\frac{d\mathbf{p}}{dt} = \mathbf{Q} \cdot \mathbf{v}$, where, $\mathbf{p}$ includes the concentrations of all substrates except the first one, $\mathbf{Q}$ is a stoichiometry matrix and $\mathbf{v}$ includes the reaction rates. The material balance for the oxidized form of the cofactor can be written as follows: $\frac{dc_1}{dt} = \mathbf{q} \cdot \mathbf{v}$, where, c_1 is the concentration of the oxidized form of the cofactor and $\mathbf{q}$ a stoichiometry vector. Vector $\mathbf{x}$ containing the coefficients of the characteristic equation x_i with $i \in \{2, .., n\}$ is found by solving the following matrix equation: $\mathbf{x} \cdot \mathbf{Q} = \mathbf{q}$

For linear cascades, without branching points, and the same number of oxidizing and reducing steps, method 1 can be replaced by a simple graphical method which includes the cofactor trajectory graph (CTG). The cofactor trajectory graph is a simple graph, comprising arrows and levels, constructed directly from the stoichiometry of the CRN. The y-axis gives the cumulative change in oxidation number α_i of the cofactor from step to step in the cascade. The graph starts at $\alpha_1 = 0$ for substrate S_1. Every step that reduces (oxidizes) the cofactor leads to a decrease (increase) in the oxidation number by one. All steps not depending on the cofactor leave the oxidation number the same. The oxidation numbers in the CTG, equal the coefficients of the characteristic equation. Three examples of the CTG are given in Figure 8 for the studied CRNs. The cofactor trajectory graph can be used to understand which intermediates boost linear redox neutral cascades according to theorem 2.

Theorem 2: Graphical identification of intermediates that boost for linear redox neutral cascades.
For linear redox neutral cascades as we study in the CRNs a), b) and d), the identification of boosting intermediates is easily done with the cofactor trajectory graph (CTG). If all intermediates in the cofactor trajectory graph are below (above) or on the x-axis, all intermediates boost the cascade. If there are intermediates both below and on/above the x-axis, which intermediates boost depends on the relative value of the kinetic parameters. When the rate limiting step is reductive, all intermediates above the x-axis delay and all intermediates below the x-axis boost. When the rate limiting step is neutral or oxidative and is above the x-axis, intermediates above the line boost and below the line delay. When the rate limiting step is neutral or oxidative and is below the x-axis, the opposite is true. When the rate limiting step is on the x-axis no intermediate boosts.

Note that for CRN c) no solution is given. This network is non-linear and therefore can not be solved using 2. Still, theorem 1 can be used. Applying theorems 1 and 2 one can tell that in CRNs a) and b) all cascades boost, while in cascades c) and d) which intermediates boost depends on the kinetic parameters. After knowing the intermediate(s) that boost the cascade, it is also interesting to know how strongly they boost. As illustrated in Figure 9, the cofactors and the intermediates enter a quasi steady-state which determines the duration of the cascade. Larger quasi steady-state concentrations for the oxidized form of the cofactor (for cascades that start with a cofactor-reducing step) and the intermediates lead to faster overall kinetics in the cascade reaction. The quasi steady- state reaction rates and concentrations can be calculated using Method 2.

Method 2: Quasi steady-state analysis
For known kinetic parameters and initial titers, and the kinetics of the first step saturated and independent of the raw material concentration the quasi steady-state concentrations of cofactors and intermediates as well as the quasi steady-state reaction rate can be calculated by solving the system of equations $v_{\mathrm{I}}^{\mathrm{qss}} = v_{\mathrm{II}}^{\mathrm{qss}} = ... = v_{k}^{\mathrm{qss}}$ for cascades of k steps together with the characteristic equation of the redox neutral cascade and the equation $\frac{dc_1}{dt} = -\frac{dc_2}{dt}$ that is derived from the material balance. After the quasi steady-state concentrations are estimated, the runtime t_{f} till high conversion can be estimated by the equation $t_{\mathrm{f}} = S_1^0/v_{\mathrm{I}}^{\mathrm{qss}}$.

Though adding intermediates can significanly increase the space-time yield, there are limitations as described in Theorem 3.

Theorem 3: Maximum space-time yield. In a redox enzymatic cascade reaction with one educt and one product and a 1:1 stoichiometry, the quasi steady-state space-time yield never exceeds the smallest maximum reaction rate V_{max} of the enzymes regardless of how much substrate, intermediate or cofactor is added.

Of course, the space-time yield might not reach this limit for several reasons, e.g., because not enough intermediates or cofactors are used to accelerate the cascade, due to inhibition or because enzymes deactivate. Since cofactor costs are high, it is interesting to study the case where the reaction rates of cofactor-dependent steps are further constrained because not enough cofactor is added. Let us look at the simplest cascade in Figure 8 CRN a). An upper limit to the quasi steady-state cofactor concentration can be calculated as follows. Suppose Michaelis-Menten type kinetics like:

$$v_{\mathrm{I}} = \frac{V_{\mathrm{max,I}} \cdot S_1 \cdot c_1}{(K_{\mathrm{m,S_1}} + S_1) \cdot (K_{\mathrm{m,c_1}} + c_1)} \tag{27}$$

$$v_{\mathrm{II}} = \frac{V_{\mathrm{max,II}} \cdot S_2 \cdot c_2}{(K_{\mathrm{m,S_2}} + S_2) \cdot (K_{\mathrm{m,c_2}} + c_2)} \tag{28}$$

During the quasi steady-state, the educt concentration S_1 is much larger than the respective K_{m,S_1} also it is reasonable to assume that the cofactor concentration is much smaller than the respective K_{m}. Therefore, $S_1 >> K_{\mathrm{m,S_1}}$ and $c_1 << K_{\mathrm{m,c_1}}$ Equation (27) simplifies to:

$$v_\mathrm{I} \approx \underbrace{\frac{V_\mathrm{max,I}}{K_\mathrm{m,c_1}}}_{k_\mathrm{I}} \cdot c_1 \tag{29}$$

For the second step of CRN a), when no or small amounts of intermediate are added in the start of the reaction, the reaction rate can be approximated as follows (when $S_2 << K_\mathrm{m,S_2}$ and $c_2 << K_\mathrm{m,c_2}$) by simplifying Equation (28):

$$v_\mathrm{II} \approx \underbrace{\frac{V_\mathrm{max,II}}{K_\mathrm{m,c_2 \cdot K_{m,S_2}}}}_{k_\mathrm{II}} \cdot c_2 \cdot S_2 \tag{30}$$

Equation (30) is just an approximation and is only valid when small amounts of substrates S_2 and c_2 are present. If a large amount of intermediate S_2 is added to boost the cascade, the kinetics of the second reaction step will eventually become large enough to ignore the dependence on S_2. Therefore, when $S_2 >> K_\mathrm{m,S_2}$ and $c_2 << K_\mathrm{m,c_2}$ then Equation (28) simplifies to:

$$v_\mathrm{II} \approx \underbrace{\frac{V_\mathrm{max,II}}{K_\mathrm{m,c_2}}}_{k_\mathrm{II}'} \cdot c_2 \tag{31}$$

Of course, both Equation (30 and 31) are approximations, for an accurate description of the reaction rate Equation (28) has to be used. Applying method 2 (taking $v_\mathrm{I}^\mathrm{qss} = v_\mathrm{II}^\mathrm{qss}$) with the kinetic model of Equations (29) and (30), one can calculate the quasi steady-state concentrations and reaction rates by solving the resulting second order polynomial. Using Equation (29) and (31) an upper limit can be calculated that looks as follows:

$$c_\mathrm{1,max}^\mathrm{qss} = c_1^0 \cdot \frac{k_\mathrm{II}'}{k_\mathrm{I} + k_\mathrm{II}'} \tag{32}$$

From here an upper limit for the maximum space-time yield can be calculated from $v_\mathrm{I}^\mathrm{qss}$ as follows:

$$v_\mathrm{I,max}^\mathrm{qss} = c_1^0 \cdot \frac{k_\mathrm{I} \cdot k_\mathrm{II}'}{k_\mathrm{I} + k_\mathrm{II}'} \tag{33}$$

The minimum total cascade duration is:

$$t_{\mathrm{f,min}} = \frac{S_1^0 \cdot (k_{\mathrm{I}} + k'_{\mathrm{II}})}{c_1^0 \cdot k_{\mathrm{I}} \cdot k'_{\mathrm{II}}} \tag{34}$$

The quasi steady-state cofactor concentration is plotted for different initial intermediate concentrations (S_2^0) in Figure 10 by applying method 2 for CRN a) with selected parameter values. The red line shows the limit emposed by Equation (32). The doted line shows the quasi steady-state cofactor concentration that is reached when $S_2^0 = K_{\mathrm{m,S_2}}$.

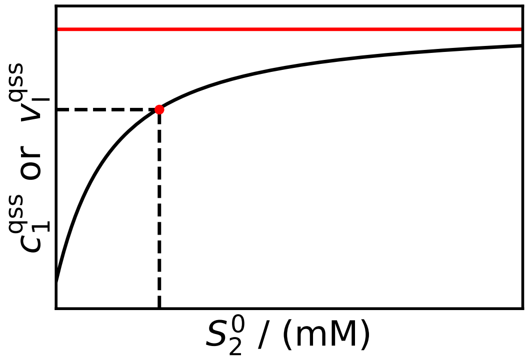

Figure 10: c_1^{qss} or $v_{\mathrm{I}}^{\mathrm{qss}}$ as a function of S_2^0. The red line shows an approximation of the upper limit imposed by Equations (32 and 33). The red dot corresponds to the case where $S_2^0 = K_{\mathrm{m,S_2}}$.

3.3 Numerical studies

3.3.1 Boosting effect on the simplest chemical reaction network

Kinetic modeling as demonstrated in multiple works the past years [51–54, 90] can effectively describe the boosting effect of intermediates. Let us start with the simplest chemical reaction network. Simulations for CRN a) (using a kinetic model with parameters chosen to be in typical ranges) demonstrate the effect of boosting by intermediates for different initial intermediate titers in Figure 11. In the first panel, no intermediate is added, and therefore intermediate S_2 is constrained to be under the initial cofactor titer. This can be shown by integrating the characteristic equation of CRN a) (Equation 23) from time $t = 0$ to time $t = t^{\mathrm{qss}}$ and rearranging:

$$S_2^{\mathrm{qss}} = c_1^0 - c_1^{\mathrm{qss}} + S_2^0 \tag{35}$$

Therefore, when $S_2^0 = 0$:

$$S_2^{\text{qss}} < c_1^0 \tag{36}$$

Due to the small concentrations of the intermediate and cofactor during quasi steady-state, the second reaction, the rate of which depends on the concentration of the intermediate, acts as a bottleneck on the space-time yield. When adding the $S_2^0 = 20$ mM ($\approx K_{m,S_2}$) of intermediate at the start of the reaction process in the second panel, full conversion is reached much faster, since now the constraint on the quasi steady-state cofactor concentration is relaxed by 20 mM.

$$S_2^{\text{qss}} < c_1^0 + 20\text{ mM} \tag{37}$$

Note that the magnitude of the boosting effect depends on the kinetic parameters and not only on the structure of the reaction network. Adding $S_2^0 = 80$ mM of intermediate ($>> K_{m,S_2}$) in panel three does not boost the cascade much further, since what is now rate limiting is the cofactor concentration which is still much lower than the respective $K_{m,c}$.

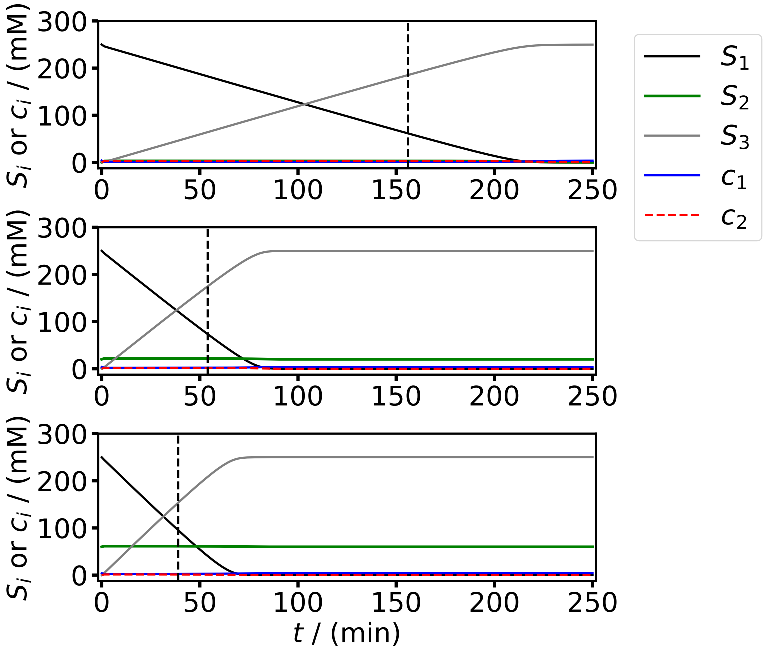

Figure 11: CRN a) simulated with and without the addition of intermediate S_2. The black dashed line shows the approximation obtained for the duration of the cascade by method 2 using the simplified kinetic models shown in Equations (29 and 30). The model equations and kinetic parameters for the model of CRN a) are given in the Appendix B. In the first panel no intermediate is added ($S_2^0 = 0$ mM) . In the second panel $S_2^0 = 20$ mM. In the third panel $S_2^0 = 80$ mM. All other parameters are kept constant.

The value of boosting by intermediates as a method becomes apparent when studying how much cofactor one can potentially substitute for the same amount of intermediate. In Figure 12 different combinations of the initial amounts of intermediate and cofactor that can be used to achieve the same space-time yield are compared. The x- and y-axis show the initial intermediate and cofactor amounts respectively, while the different space-time yields are given with the three different levels. For a space time yield of 1 mM/min, 2 mM of cofactor can be exchanged for 10 mM of intermediate, this exchange might be very favorable economically, considering that the cofactor has a much larger molecular weight than most cascade intermediates, but also a much higher price per unit weight than most, if not all, cascade intermediates.

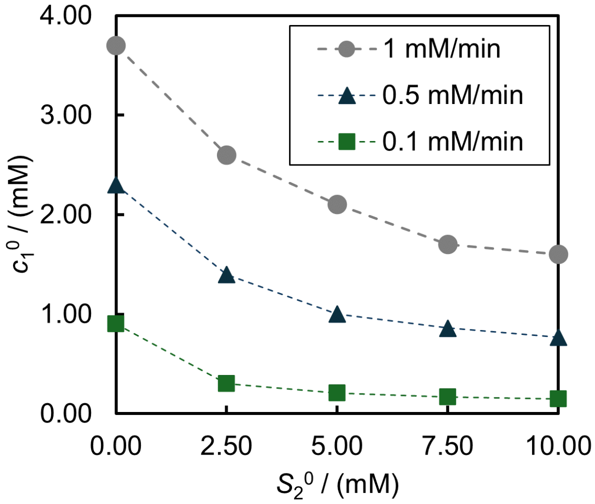

Figure 12: The initial cofactor concentration that must be added to achieve the same space time yield for different initial intermediate concentrations for CRN a). The model equations and kinetic parameters for the model of CRN a) are given in the SI.

3.3.2 Model-based optimization of the production of (S)-1,2,4-butanetriol

The design of enzymatic cascade reaction systems can be achieved through model-based optimization by solving optimal-control problems [51–54, 90, 91]. A model was developed and parameterized for the enzymatic cascade of Sutiono et al. [56] (c.f. Figure 8). Michaelis-Menten type reaction kinetic models were fitted to assay experiments and were used to model the cascade. The complete model, including parameter values, is given in Appendix B. The model demonstrated a decent fit to experiment (c.f. Appendix B) and multi-objective optimization was applied [90]. In industrial processes, decisions are made by comparing profits or costs per unit time so objectives connected with revenue or cost per unit time where used. Namely, the space-time yield which is connected to revenue and the cofactor and intermediate consumptions which are connected to costs were used.

$$\varPhi^{\mathrm{STY}} = \frac{S_6(t_\mathrm{f})}{t_\mathrm{f} + t_\mathrm{p}} \tag{38}$$

$$\varPhi^{\mathrm{CC}} = \frac{c_1^0}{t_\mathrm{f} + t_\mathrm{p}} \tag{39}$$

$$\varPhi^{\mathrm{IC}} = \frac{\sum\limits_{i \in \mathcal{I}} S_i^0}{t_\mathrm{f} + t_\mathrm{p}} \tag{40}$$

Where t_f is the final reaction time, t_p is the preparation time between batches and $\mathcal{I}$ is the set of all intermediates of the cascade. Note that according to theorem 1 and the corresponding CTG, all intermediates can potentially boost this cascade, the choice between all intermediates is given to the optimizer and the optimizer chooses based on which intermediate gives the biggest kinetic advantage. Of course, if information is known about the price (or other criteria) of the intermediates, those can be added to the model and the optimizer can make an informed decision. The first objective, space-time yield, is to be maximized, while the other two objectives have to be minimized. The yield was constrained to be larger or equal to 95%, all substrate titers were kept below the solubility limits and the total reaction process duration was constrained to be smaller or equal to 48 h. Further, the enzyme consumption was constrained to be smaller or equal to 0.1 μM/min as shown below.

$$\frac{\sum\limits_j \{E_j^0\}}{t_\mathrm{f} + t_\mathrm{p}} \leq 0.1\ \mu\mathrm{M/min} \tag{41}$$

Where E_j^0 are the enzyme titers. The results are presented in Figure 13. The objectives shown in Equations (38) and (40) are shown in the x and y axis respectively while the objective shown in Equation (39) is shown with the different levels. The space-time yield rises quite rapidly at first. A small amount of intermediate can increase the space-time yield significantly i.e., from roughly 0.5 mM/min to roughly 1.1 mM/min for an intermediate consumption equal to 0.0005 mM/min. At higher intermediate consumption the Pareto front flattens out. When designing such reaction processes, the trade-offs between the prices can be compared with this method.

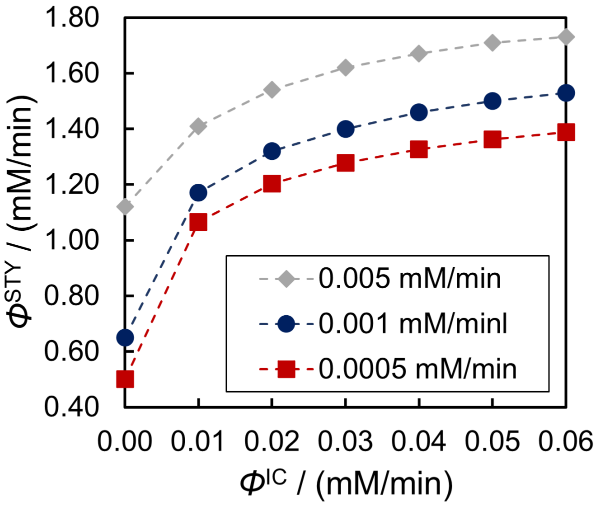

Figure 13: Pareto optimal process schedules for the cascade developed by Sutiono et al.

Model-based optimization is especially useful when designing reaction processes with complex redox neutral cascades where BBI can be applied. Simultaneously selecting the titers of substrates, intermediates, enzymes and cofactors is a difficult task even when all enzymes are kinetically characterized. The optimizer can systematically make that selection to study tradeoffs and maximize productivity. Further, the selection of which intermediates should be added can be done by the optimizer.

3.4 Fundamentals and Proofs

3.4.1 Material balance

We focus on reactions carried out in discontinuous batch processes. The concentrations of the different chemical species of the biochemical reaction networks change with time according to the stoichiometry of the reactions and the reaction rates. Differential material balances are written to express the change in the substrate concentrations. For example, for CRN a) these are written as follows:

$$\frac{dS_1}{dt} = -v_{\mathrm{I}} \tag{42}$$

$$\frac{dS_2}{dt} = v_{\mathrm{I}} - v_{\mathrm{II}} \tag{43}$$

$$\frac{dS_3}{dt} = v_{\mathrm{III}} \tag{44}$$

$$\frac{dc_1}{dt} = -v_{\mathrm{I}} + v_{\mathrm{II}} \tag{45}$$

$$\frac{dc_2}{dt} = v_{\mathrm{I}} - v_{\mathrm{II}} \tag{46}$$

Where, S_i with $i = 1, 2, 3$ are the concentrations of the substrates of the reaction network of the cascade. c_1 and c_2 are the concentrations of the oxidized and reduced forms of the cofactor respectively and v_k with $k = \mathrm{I}, \mathrm{II}$ are the rates of reactions I and II. Material balances can be written in compact matrix form. We include the first-order derivatives with respect to time of the substrate concentrations, $\dot{S}_i$ with $i = 1, 2, ..., n$ together with the cofactor concentrations c_1 and c_2, in the concentration rate vector $\dot{\mathbf{s}}$. The stoichiometric coefficients are included in the stoichiometry matrix **U**. The reaction rates v_k with $k = \mathrm{I}, \mathrm{II}, ..., z$ are included in the reaction rate vector **v**. The material balances for the substrates are then expressed by Equation (47).

$$\frac{d\mathbf{s}}{dt} = \mathbf{U} \cdot \mathbf{v} \tag{47}$$

For CRN a) the matrices are:

$$\mathbf{s} = \begin{bmatrix} S_1 \\ S_2 \\ S_3 \\ c_1 \\ c_2 \end{bmatrix}, \ \mathbf{U} = \begin{bmatrix} -1 & 0 \\ +1 & -1 \\ 0 & +1 \\ -1 & +1 \\ +1 & -1 \end{bmatrix}, \ \mathbf{v} = \begin{bmatrix} v_{\mathrm{I}} \\ v_{\mathrm{II}} \end{bmatrix}$$

The matrices **s**, **U**, and **v** for CRNs b), c) and d) are given in the supporting information. Note that for any CRN the stoichiometry matrix **U** can be rewritten according to the definitions given in Chapter 2 as follows. Where $\mathbf{U}_{\mathrm{R1}} = \mathbf{U}[1; 1, 2, ..., z]$ is the first row of **U**.

$$\mathbf{U} = \begin{bmatrix} \mathbf{U}_{\mathrm{R1}} \\ \mathbf{Q} \\ \mathbf{q} \\ \text{-}\mathbf{q} \end{bmatrix}$$

3.4.2 Reaction rate models and appropriate simplifications

In the absence of inhibition effects, the reaction rate of both single- and double-substrate, enzyme-catalyzed reactions are usually modeled with Michaelis-Menten type reaction rate models as shown in Equation (48 and 49) respectively.

$$v = \frac{V_{\mathrm{max}} \cdot S}{(K_{\mathrm{m,S}} + S)} \tag{48}$$

$$v = \frac{V_{\mathrm{max}} \cdot S \cdot c}{(K_{\mathrm{m,S}} + S) \cdot (K_{\mathrm{m,c}} + c)} \tag{49}$$

It is well known that, the single-substrate Michaelis-Menten kinetic model approximates first-order kinetics for small substrate concentrations and zero-order kinetics for larger substrate concentrations. Steps that are not cofactor dependent are modeled with single Michaelis-Menten kinetics. If these steps are exposed to a large substrate concentration (i.e, $S >> K_{\mathrm{m,S}}$), e.g., if they are the first step of the cascade or if a lot of the respective intermediate is present, the following simplification can be made:

$$v \approx V_{\mathrm{max}} \tag{50}$$

On the other hand, if only a small amount of substrate is present (i.e., $S << K_{\mathrm{m,S}}$) the following simplification can be made:

$$v \approx \underbrace{\frac{V_{\mathrm{max}}}{K_{\mathrm{m,S}}}}_{k} \cdot S \tag{51}$$

The kinetic parameters can be combined in one named k. For cofactor dependent steps, double substrate Michaelis-Menten kinetic models are used. The single substrate Michaelis-Menten kinetic is only appropriate if either large amount of substrate or cofactor are present (i.e, $S >> K_{\mathrm{m,S}}$ or $c >> K_{\mathrm{m,c}}$). For example, when the first step of the cascade is cofactor dependent and a large amount of raw material but small amount of cofactor is used then the reaction rate of the first reaction can be approximated with a single substrate Michaelis-Menten kinetic model as shown below:

$$v \approx \frac{V_{\mathrm{max}} \cdot c}{(K_{\mathrm{m,c}} + c)} \tag{52}$$

For the resulting single-substrate Michaelis-Menten kinetic model the simplifications shown in Equations (50 and 51) apply when the respective conditions are met. Moreover, in intermediate steps both the substrate and the cofactor concentrations might be very small (i.e, $S << K_{\mathrm{m,S}}$ and $c << K_{\mathrm{m,c}}$). For example, in intermediate cascade steps that are cofactor dependent. Then the following simplification applies:

$$v \approx \underbrace{\frac{V_{\max}}{K_{\mathrm{m,S}} \cdot K_{\mathrm{m,S}}}}_{k} \cdot S \cdot c \tag{53}$$

These approximations are useful when studying the CRNs of redox neutral cascades under quasi steady-state conditions. In model-based optimization of the cascades, such approximations are not necessary and complex reaction rate models, e.g., including inhibition effects, can be easily handled by numerical solvers.

3.4.3 Fundamentals of quasi steady-state analysis

Studying redox neutral cascade reaction networks under the quasi steady-state assumption can reveal useful insights and help debottleneck them. As described in method 2, the quasi steady-state concentrations of all intermediates can be estimated. Further, quasi steady-state analysis gives a tool or debbotlenecking the cascades to experimentalists that are not interested in simulating or optimizing kinetic models that comprise systems of differential equations. To demonstrate this we will look at CRN b). It has the same structure as the CRN a) and only differs due to the extra intermediate steps between the two cofactor-dependent steps. One could wonder what the effect of these additional intermediate steps could be. When S_2, S_3, S_4, c_1 and c_2 are in quasi-steady state the following equation holds true (using simplified kinetic models):

$$v_{\mathrm{I}}^{\mathrm{qss}} = v_{\mathrm{II}}^{\mathrm{qss}} = v_{\mathrm{III}}^{\mathrm{qss}} = v_{\mathrm{IV}}^{\mathrm{qss}} = v_{\mathrm{IV}}^{\mathrm{qss}} \tag{54}$$

Using simplified kinetic models we get:

$$k_{\mathrm{I}} \cdot c_1^{\mathrm{qss}} = k_{\mathrm{II}} \cdot S_2^{\mathrm{qss}} = k_{\mathrm{III}} \cdot S_3^{\mathrm{qss}} = k_{\mathrm{IV}} \cdot S_4^{\mathrm{qss}} = k_{\mathrm{V}} \cdot S_5^{\mathrm{qss}} \cdot c_2^{\mathrm{qss}} \tag{55}$$

When reaction II has a much larger kinetic constant than the other reactions the concentration of S_2 approaches zero as shown in the following equation.

$$S_2^{\mathrm{qss}} = \frac{k_{\mathrm{I}}}{k_{\mathrm{II}}} \cdot c_1^{\mathrm{qss}} \tag{56}$$

On the other hand, when reaction II has a much smaller kinetic constant than the other reactions then S_2 accumulates, c_1 goes to zero and the cascade stops. Futher, if we run an experiment and learnt that it took $t_{\mathrm{f}} = 300$ min for $S_1^0 = 100$ mM of raw material to be consumed we could calculate the quasi steady-state cofactor (or any other) concentration as follows:

$$c_1^{\mathrm{qss}} = \frac{S_1^0}{(t_{\mathrm{f}} \cdot k_{\mathrm{I}})} \tag{57}$$

This type of analysis can also show us the circumstances under which a cascade reaction would stop. Let's look at CRN c). The material balance for the cofactor is:

$$\frac{dc_1}{dt} = -k_{\mathrm{I}} \cdot c_1(t) - k_{\mathrm{IV}} \cdot c_2(t) \cdot S_4(t) + k_{\mathrm{VII}} \cdot (c_1^0 - c_1(t)) \cdot S_7(t) \tag{58}$$

When the quasi-steady state is reached $\dot{c}_1(t) = 0$ and Equation (59) can be derived by rearranging Equation (58):

$$c_1^{\mathrm{qss}} = \frac{k_{\mathrm{VII}} \cdot S_7^{\mathrm{qss}} \cdot c_1^0}{k_{\mathrm{I}} + k_{\mathrm{IV}} \cdot S_4^{\mathrm{qss}} + k_{\mathrm{VII}} \cdot S_7^{\mathrm{qss}}} \tag{59}$$

If in the assumed quasi-steady state the concentration of S_7 is zero the cascade will stop.

3.4.4 Fundamentals of the characteristic equation

In redox neutral cascades, the rate of change of the cofactor concentration depends on the rate of change of a number of intermediates of the cascade. This relationship can be derived from the material balance and is specific to redox neutral cascades and will not be found in cascades that require a second independent reaction network for cofactor regeneration like the cascade of Beer et al. [8, 90]. The general form of the characteristic equation is shown in the following equation.

$$\frac{dc_1}{dt} = \sum_{i \in \mathcal{I}} x_i \cdot \frac{dS_i}{dt} \tag{60}$$

Where x_i is a real number and $\mathcal{I} = \{2, .., n-1\}$. Note that the characteristic equation does not include the concentration of the educt or the product. It only includes the concentrations of intermediates and one of the cofactor forms, and therefore, only the concentrations of things that are added at relatively low concentrations at the start of the reaction process (compared to the educt). This is a crucial feature. Naturally, by applying the conservation of mass we can also write this equation in a different form which includes the educts or products. The characteristic equation can also be written in compact matrix form as follows:

$$\frac{dc_1}{dt} = \mathbf{x} \cdot \frac{d\mathbf{p}}{dt} \tag{61}$$

where $\mathbf{p}$ is a vector comprising the concentrations of all substrates except S_1. And $\mathbf{x}$ is defined as shown in Equation (62).

$$\mathbf{x} = [x_2, x_3, ...x_n]. \tag{62}$$

Even though, x_n (corresponding to the product) is included in vector $\mathbf{x}$ it always equals zero for cofactor balanced cascades with one educt and one product (i.e., with the same number of oxidation as reduction steps).

3.4.5 Proof of theorem 1

Lemma 1.1: The characteristic equation can be derived by solving $\mathbf{x} \cdot \mathbf{Q} = \mathbf{q}$
Material balances can be written in compact matrix form as shown in Equation (63).

$$\frac{d\mathbf{s}}{dt} = \mathbf{U} \cdot \mathbf{v} \tag{63}$$

We now rerwite Equation (63) excluding the first substrate and the two cofactor forms:

$$\frac{d\mathbf{p}}{dt} = \mathbf{Q} \cdot \mathbf{v} \tag{64}$$

We include the first order derivatives with respect to time of all substrate concentrations (except S_1) $\frac{dS_i}{dt}$ with $i = 2, ..., n$ in vector $\frac{d\mathbf{p}}{dt}$. $\mathbf{Q}$ and $\mathbf{v}$ are defined as already discussed. We also define the material balance for the oxidized form of the cofactor, c_1 as follows:

$$\frac{dc_1}{dt} = \mathbf{q} \cdot \mathbf{v} \tag{65}$$

Where $\mathbf{q}$ is defined as already discussed. Rearanging Equations (64) and (65) we get:

$$\mathbf{v} = \mathbf{Q}^{-1} \cdot \frac{d\mathbf{p}}{dt} \tag{66}$$

and,

$$\mathbf{v} = \mathbf{q}^{-1} \cdot \frac{dc_1}{dt} \tag{67}$$

Combining these two equations we get:

$$\mathbf{Q}^{-1} \cdot \frac{d\mathbf{p}}{dt} = \mathbf{q}^{-1} \cdot \frac{dc_1}{dt} \tag{68}$$

and rearanging we get:

$$\mathbf{Q}^{-1} = \mathbf{q}^{-1} \cdot \frac{dc_1}{dt} \cdot \left(\frac{d\mathbf{p}}{dt}\right)^{-1} \tag{69}$$

The characteristic equation can be written in matrix form as follows:

$$\frac{dc_1}{dt} = \mathbf{x} \cdot \frac{d\mathbf{p}}{dt} \tag{70}$$

or equivalently:

$$\mathbf{x} = \frac{dc_1}{dt} \cdot \left(\frac{d\mathbf{p}}{dt}\right)^{-1} \tag{71}$$

Combining Equation (69) with (71) we get:

$$\mathbf{Q}^{-1} = \mathbf{q}^{-1} \cdot \mathbf{x} \tag{72}$$

or,

$$\mathbf{Q}^{-1} \cdot \mathbf{x}^{-1} = \mathbf{q}^{-1} \tag{73}$$

which means that:

$$\mathbf{x} \cdot \mathbf{Q} = \mathbf{q} \tag{74}$$

Lemma 1.2: The characteristic equation shows which intermediates boost or delay linear cascades

We are dealing with three types of reaction rate models: cofactor-neutral, cofactor-oxidizing and cofactor-reducing. In this proof, simplified kinetic models are used to approximate the behaviour of Michelis-Menten type models in typical concentration ranges for each step of the cascade as described in previous sections. As already stated, the coefficients of the intermediates are positive or negative, or when they do not appear at all, they are equal to zero. The intermediates that appear in the characteristic equation also appear in the reaction rate models (cofactor-neutral, oxidizing or reducing). Let's look at the case that all intermediates appear in the characteristic equation with negative signs, and therefore they all reach a quasi steady-state, the reaction rates of all steps of the cascade are equal to each other and equal to the reaction rate of the first step.

For a cofactor-neutral reaction step including intermediate S_i (since we are only dealing with linear cascades we can use roman numerals to designate the kinetic parameters, k_i will be the kinetic parameter of the reaction step that has S_i as an educt):

$$k_1 \cdot c_1^{\text{qss}} = k_i \cdot S_i^{\text{qss}} \tag{75}$$

which means that:

$$S_i^{\text{qss}} = \frac{k_1 \cdot c_1^{\text{qss}}}{k_i} \tag{76}$$

For a cofactor-reducing reaction step including intermediate S_i:

$$k_1 \cdot c_1^{\text{qss}} = k_i \cdot S_i^{\text{qss}} \cdot c_1^{\text{qss}} \tag{77}$$

which (for $c_1^{\text{qss}} > 0$) means that:

$$S_i^{\text{qss}} = \frac{k_1}{k_i} \tag{78}$$

For a cofactor-oxidizing reaction step including intermediate S_i:

$$k_1 \cdot c_1^{\text{qss}} = k_i \cdot S_i^{\text{qss}} \cdot c_2^{\text{qss}} \tag{79}$$

which (for $c_1^{\text{qss}} < c_1^0$) means that:

$$S_i^{\mathrm{qss}} = \frac{k_1 \cdot c_1^{\mathrm{qss}}}{k_i \cdot (c_1^0 - c_1^{\mathrm{qss}})} \tag{80}$$

Note that in all three cases, S_i^{qss} rises monotonously with the quasi steady-state concentration of cofactor c_1^{qss}. Integrating the general form of the characteristic equation from time $t = 0$ to time $t = t^{\mathrm{qss}}$ we get:

$$c_1^{\mathrm{qss}} - c_1^0 = \sum_{i \in \mathcal{I}} x_i \cdot (S_i^{\mathrm{qss}} - S_i^0) \tag{81}$$

Rearranging Equation (81) we get:

$$c_1^{\mathrm{qss}} - c_1^0 - \sum_{i \in \mathcal{I}} x_i \cdot S_i^{\mathrm{qss}} = -\sum_{i \in \mathcal{I}} x_i \cdot S_i^0 \tag{82}$$

Substituting Equations (76), (78) and (80) to Equation (82) we get:

$$c_1^{\mathrm{qss}} - c_1^0 - \sum_{i \in \mathcal{N}} x_i \cdot \frac{k_1 \cdot c_1^{\mathrm{qss}}}{k_i} - \sum_{i \in \mathcal{R}} x_i \cdot \frac{k_1}{k_i} - \sum_{i \in \mathcal{O}} x_i \cdot \frac{k_1 \cdot c_1^{\mathrm{qss}}}{k_i \cdot (c_1^0 - c_1^{\mathrm{qss}})} = -\sum_{i \in \mathcal{I}} x_i \cdot S_i^0 \tag{83}$$

Where, $\mathcal{N}$ is the set of all cofactor-neutral steps, $\mathcal{R}$ is the set of all cofactor-reducing steps and $\mathcal{O}$ is the set of all cofactor-oxidizing steps. Let us study the monotonicity of the left hand side term of the above equation. To do so, we will take the first order derivative with respect to c_1^{qss}:

$$DER = 1 - \sum_{i \in \mathcal{N}} x_i \cdot \frac{k_1}{k_i} - \sum_{i \in \mathcal{O}} x_i \cdot \frac{k_1 \cdot c_1^0}{k_i \cdot (c_1^0 - c_1^{\mathrm{qss}})^2} \tag{84}$$

When all x_i are negative the derivative is always positive and therefore the term on the left hand side of Equation (83) is monotonously rising with c_1^{qss}. The right hand side of Equation (83) contains the initial titers of all intermediates that appear in the characteristic equation. Therefore, increasing the initial titers of all intermediates that appear in the characteristic equation will increase c_1^{qss} (since -x_i is a non-negative number for $i \in \mathcal{I}$) and for this reason also increase $v_{\mathrm{I}}^{\mathrm{qss}} = -\dot{S_1}^{\mathrm{qss}}$ and lead to boosting by intermediates.

When the characteristic equation does not include all intermediates with negative coefficients but some of them appear with coefficients positive, negative and/or equal to zero, which intermediates boost depends on the relative values of the kinetic paramaters and no easy answer can be given unless a rate determining step exists.

Let's look at the case were there is a rate determining step, i.e., an oxidizing, neutral or reducing step for which k_{rds}<<k_{i}. In this case, in quasi steady-state the reaction rate of all steps will equal the reaction rate of the rate determining step and the derivative can be approximated one of Equations (85-87). For cofactor-oxidizing:

$$DER \approx -x_{\mathrm{rds}} \cdot \frac{k_1}{k_{\mathrm{rds}}} \tag{85}$$

For cofactor-neutral:

$$DER \approx -x_{\mathrm{rds}} \cdot \frac{k_1 \cdot c_1^0}{k_{\mathrm{rds}} \cdot (c_1^0 - c_1^{\mathrm{qss}})^2} \tag{86}$$

For cofactor-reducing:

$$DER \approx 1 \tag{87}$$

This means that when the rate determing step is cofactor-oxidizing or cofactor-neutral, the intermediates with a coefficient that has the same sign as the intermediate that reacts in the rate determining step boost. Those with the opposite sign delay. When the rate determing step is cofactor-reducing, intermediates with negative coefficients boost and with positive coefficients delay. If the rate determining step corresponds to the reaction of a substrate that has a characteristic coefficient equal to zero, then no boosting or delaying effect can be achieved.

The exact opposite procedure can be carried out for a cascade that starts with a cofactor-oxidizing step to find out under which conditions c_2^{qss} increases.

3.4.6 Proof of theorem 2

Lemma 2.1: Each coefficient a_i, with $i > 1$, of the CTG is equal to: $a_i = \sum_{j=1}^{i-1} q_j$

Proof: From the definition of the CTG. We start at row $a_i = 0$ (a_1 is forced to be 0) and go down a row for each reductive step, stay on the same row for each neutral step, and go up a row for each oxidizing step. Therefore, a step will change the value of a_i as follows: $a_{i+1} = a_i + q_i$ where q_i is the i^{th} entry of vector $\mathbf{q}$ and is -1 for reductive steps, 0 for neutral steps, and $+1$ for oxidizing steps. n consecutive steps will make the value of $a_n = 0 + q_1 + ... + q_{n-1}$ which proves that:

$$a_i = \sum_{j=1}^{i-1} q_j \tag{88}$$

Lemma 2.2: For linear cascades, with 1:1 stoichiometry, Q is an upper bidiagonal matrix where the first entry of each row is +1 and when there is a second it is -1. Each one of the substrates S_2 - S_{n-1} of a linear cascade is produced by one reaction and consumed by another reaction. The second substrate is always produced by reaction I and consumed by reaction II. Therefore the first row of matrix **Q** has the form [+1, -1, 0, ... 0]. The third substrate is always produced by reaction II and consumed by reaction III. Therefore the second row of matrix **Q** has the form [0, +1, -1, ... 0]. This continues until the last substrate, which is only produced by the last reaction. Therefore the last row of matrix **Q** has the form [0, ... +1]. The general form of matrix **Q** for a linear cascade is:

$$\mathbf{Q} = \begin{bmatrix} +1 & -1 & 0 & ... & 0 \\ 0 & +1 & -1 & ... & 0 \\ \vdots & \vdots & \vdots & \ddots & \vdots \\ 0 & 0 & 0 & ... & +1 \end{bmatrix}$$

Lemma 2.3: For linear cascades, with 1:1 stoichiometry, $\mathbf{Q}^{\mathrm{T}}$ is a lower bidiagonal matrix where the first entry of each column is +1 and when there is a second it is -1.

It is proven from the definition of the transpose matrix and Lemma 2.3. The general form of matrix $\mathbf{Q}^{\mathrm{T}}$ for a linear cascade is:

$$\mathbf{Q}^{\mathrm{T}} = \begin{bmatrix} +1 & 0 & ... & 0 & 0 \\ -1 & +1 & ... & 0 & 0 \\ 0 & -1 & ... & 0 & 0 \\ \vdots & \vdots & \ddots & \vdots & \vdots \\ 0 & 0 & ... & -1 & +1 \end{bmatrix}$$

Lemma 2.4: The coefficients of the characteristic equation can be read on the CTG, i.e., $x_i = a_i$ for $i > 1$.

As shown in Lemma 1.1 to derive the coefficients x_i the following system of equations must be solved.

$$\mathbf{x} \cdot \mathbf{Q} = \mathbf{q} \tag{89}$$

or equivalently,

$$\mathbf{Q}^{\mathrm{T}} \cdot \mathbf{x}^{\mathrm{T}} = \mathbf{q}^{\mathrm{T}} \tag{90}$$

The above system of equations can be solved by Gauss-Jordan elimination. Since $\mathbf{Q}^{\mathrm{T}}$ has the form described in Lemma 2.3. The system can be solved by adding each row of the augmented matrix to the next one as shown below:

$R_i + R_{i+1} \longrightarrow R_{i+1}$

When the augmented matrix reaches the reduced row echelon form the solution will look like:

$$x_2 = q_1 \tag{91}$$

$$x_3 = q_1 + q_2 \tag{92}$$

$$x_4 = q_1 + q_2 + q_3 ... \tag{93}$$

Or in general, for $i > 1$:

$$x_i = \sum_{j=1}^{i+1} q_j \tag{94}$$

For example, the augmented matrix for CRN d) would be:

$$\left[\begin{array}{ccccc|c} +1 & 0 & 0 & 0 & 0 & -1 \\ -1 & +1 & 0 & 0 & 0 & +1 \\ 0 & -1 & +1 & 0 & 0 & 0 \\ 0 & 0 & -1 & +1 & 0 & +1 \\ 0 & 0 & 0 & -1 & +1 & -1 \end{array}\right]$$

And after carrying out the operation $R_i + R_{i+1} \longrightarrow R_{i+1} \ \forall \ i \in \{1, 2, 3, 4\}$ we get the following reduced row echelon form matrix:

$$\left[\begin{array}{ccccc|c} +1 & 0 & 0 & 0 & 0 & -1 \\ 0 & +1 & 0 & 0 & 0 & 0 \\ 0 & 0 & +1 & 0 & 0 & 0 \\ 0 & 0 & 0 & +1 & 0 & +1 \\ 0 & 0 & 0 & 0 & +1 & 0 \end{array}\right]$$

And therefore the coefficients x_i would be the same as the ones read from the CTG:

$x_2 = -1 = \sum_{j=1}^{1} q_j$

$x_3 = 0 = \sum_{j=1}^{2} q_j$

$x_4 = 0 = \sum_{j=1}^{3} q_j$

$x_5 = +1 = \sum_{j=1}^{4} q_j$

$x_6 = 0 = \sum_{j=1}^{5} q_j$

3.4.7 Proof of theorem 3

In quasi steady-state all reaction rates are equal to each other. The maximum reaction rate that can be reached by an enzyme is constrained by the respective $V_{\max}$. Therefore, when a cascade operates in quasi steady-state the overal reaction rate (space-time yield) will never exceed the smallest $V_{\max}$.

4 Systems with immobilized enzymes

4.1 Selection of spatial immobilization distributions and zones

In both batch and packed-bed reactors, enzymatic cascades are often achieved by immobilizing enzymes inside porous particles with different spatial immobilization distributions (SID). For example, the enzymes can be immobilized individually on different supports (individual immobilization) or all together on the same support (co-immobilization). Further, in packed bed reactors in particular the porous particles can be arranged in the same zone inside the packed-bed reactor or in different zones [15]. Since enzymatic cascades require co-factors and efficient co-factor regeneration, a number of strategies, both chemical and technical, have been developed in the past few years to make the use of cofactor-dependent enzymes possible in flow systems. The design of porous particles that have both enzymes and co-factors immobilized in them or the engineering of enzymes to attach cofactors [92, 93] are some examples.

When it comes to the design of systems with immobilized enzymes, questions relating to the selection of a SID inside the particle pores arise. In packe-bed reactors these questions are connected with questions about the selection of catalyst zones. Consider a system of a two-step enzymatic cascade reaction. One could wonder what the best way to distribute the enzymes inside the particle pores is. E.g., should the two enzymes be co-immobilized and therefore positioned inside the pores of the same particle? If they are immobilized individually, should the porous particles be mixed in one zone or separated into two separate zones? Note that in practical implementations, there is often a small number of degrees of freedom. E.g., the multiple enzymes might need different reaction conditions (pH, temperature) and can therefore not be placed in the same reactor. In addition, it might not be possible to immobilize certain enzymes on the same support [34]. Nevertheless, it is interesting to study the idealized scenarios in which the enzymes can be freely placed, as a limiting case.

In the present section, a mechanistic modeling framework for immobilized enzymatic cascades in porous particles based on first principles is developed. The framework is versatile enough to model and compare various SIDs and can be applied to both dynamic and continuous processes. The model includes geometric parameters (for describing the porous particles), physical property parameters (for mass transfer/diffusion), kinetic parameters (for reactions) and parameters related to the reactor. Both dynamic and continuous processes are studied. It is demonstrated how, due to the analogy between time and residence time in batch and plug-flow reactors these two systems can be treated analogously. The performances of different SIDs are compared against each other in parametric studies to elucidate when certain SIDs are better. Further, for continuous systems in plug-flow reactors we combine the selection of spatial-immobilization distributions with the selection of catalyst zones. When possible, analytical solutions for the macro-kinetics are derived. Otherwise, Monte Carlo sampling is used to check parameter sensitivities. Based on the results of the parametric studies, some general guidelines are derived from the theory. In addition, for flow systems a theorem is proved. Finally, it is demonstrated how to use the framework to determine the best SID between four options and the optimal enzyme surface densities for a specified reaction process.

4.2 Methodology

4.2.1 Studied systems

Both dynamic and continuous, heterogeneous reaction processes that take place either in a batch or a plug-flow reactor are studied. The reactors contain porous particles that catalyze the following two step enzymatic cascade reaction. Note that the restriction to two steps is not a limitation of the method, but suffices here to obtain speaking quantitative results.

$$\mathrm{S}_1 \xrightarrow{\mathrm{A}} \mathrm{S}_2 \xrightarrow{\mathrm{B}} \mathrm{S}_3$$

The enzymes A and B are immobilized inside the pores of the particles with some spatial immobilization distribution. For batch reactors, four different SIDs are considered (α, β, γ, δ), while for plug-flow reactors two SIDs are considered (α, β), see Figure 14.

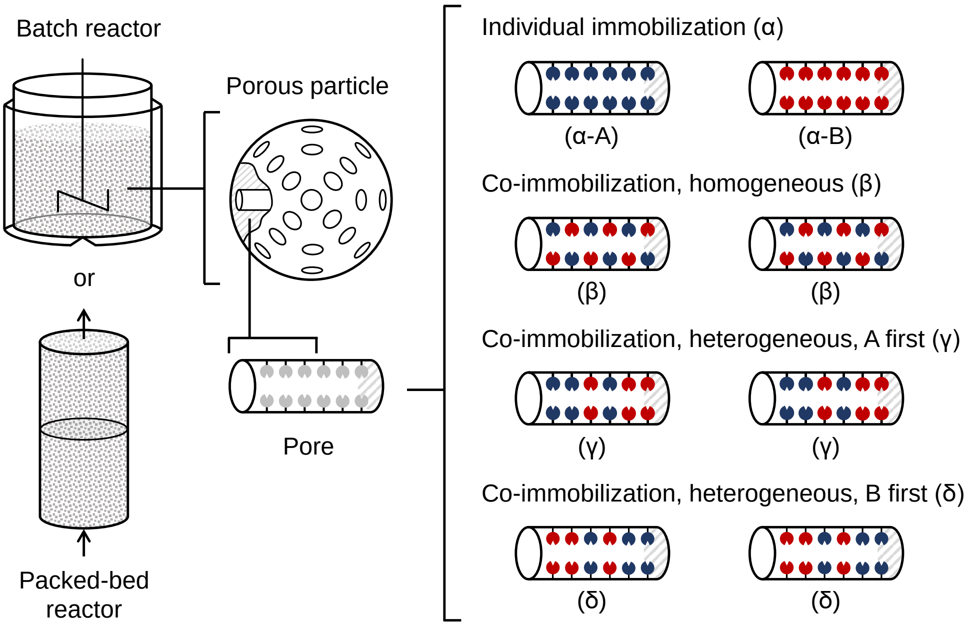

Figure 14: The considered geometry and the studied spatial immobilization distributions. Enzymes A and B are represented with blue and red colour, respectively. The analysis focuses on the cylindrical pores. The particles can have any shape. They are displayed as spherical for illustration purposes.

SID α is individual immobilization in which, each particle, and therefore each pore, only contains either enzyme A or enzyme B. SID β is the ideal homogeneous co-immobilization strategy, in which both enzymes are immobilized together in every pore. The surface densities of both enzyme A and B remain constant in the pores. Finally, two heterogeneous co-immobilization strategies are also considered. In SID γ, both enzymes are immobilized in all pores but A has a higher surface density at the entry of the pore while B has a higher surface density at the end of the pore. In SID δ, the opposite distribution is considered. When comparing the SIDs, the same number of total pores is always considered. Within the SIDs β-δ, all pores are identical. In SID α, there are two different types of pores: α-A and α-B cf. Figure 14.

The changes of substrates and products within the batch reactor depend on the macro-kinetics. The macro-kinetics are the rates resulting from the mass transfer steps and reaction steps around and inside the particle, which are shown in Figure 15 and named in Figure 15's caption. For the sake of illustration, Figure 15 shows the situation of a single immobilized enzyme. When several enzymes of one cascade are co-immobilized inside the pore, the intermediates in the cascade might, of course, adsorb and react on another enzyme's reactive site before diffusing out of the pore. For quantitative modeling and comparison of different SIDs, it is important to explicitly model the rates of both mass transfer and reaction kinetics. Whether mass transfer or whether reaction kinetics are rate-determining is decisive for differences between the performances of the SIDs.

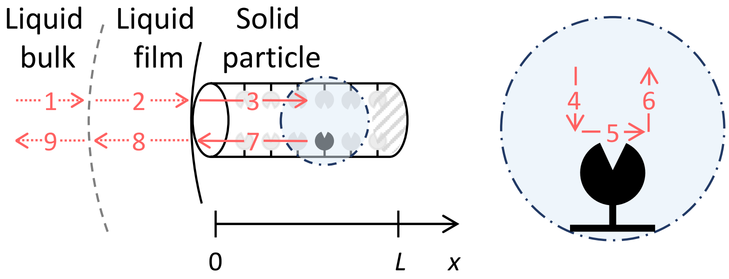

Figure 15: An overview of the considered mass transfer, adsorption-desorption and reaction steps. 1, 9: Convection and diffusion in the bulk; 2, 8: Diffusion in the liquid film around the particle; 3, 7: Diffusion inside the pores; 4: Adsorption onto the enzyme's active site; 5: Chemical reaction; 6: Desorption from the enzyme's active site.

4.2.2 Zone designs

For the packed-bed reactor three conceptual designs are studied, c.f. Figure 16 In the first design, particles with individually immobilized enzymes are mixed in the same zone. In the second design, the particles are separated into two zones, i.e., one that only contains particles with individually immobilized enzyme A and one that only contains particles with individually immobilized enzyme B. In the third design, particles with co-immobilized enzymes are mixed in one zone. When comparing the three designs, the same number of total pores and total enzyme molecules of A and B is always considered.

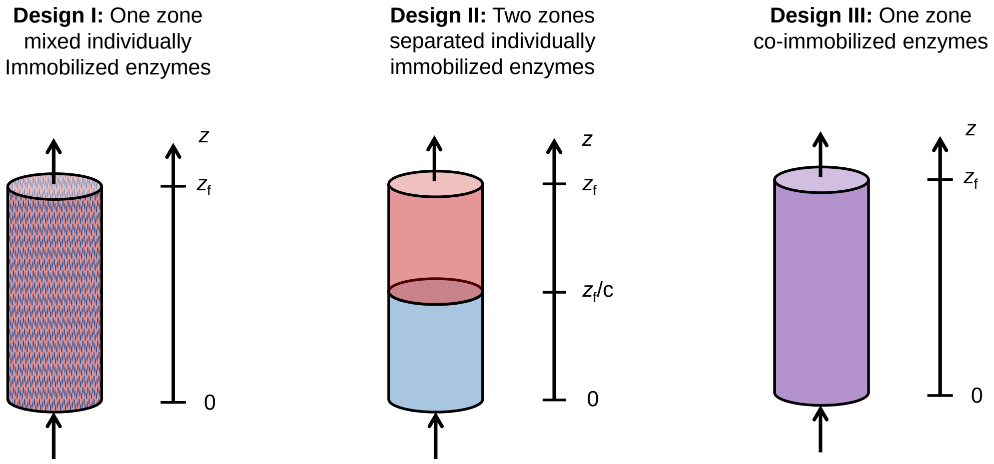

Figure 16: The considered conceptual reactor designs.

4.2.3 Assumptions

Some assumptions are introduced to ease the analysis and keep the problem manageable. This is done carefully, in order not to lose the key characteristics relevant to discriminate the SIDs. The pores are assumed to be open from one side and closed from the other. All pores have a uniform cross area A and length L. Further, it is assumed that the enzymes are immobilized irreversibly, therefore their position does not change with time [94]. It is also assumed that the surface densities of the enzymes and the concentrations of the substrates vary only in one direction inside the pore, the x-axis shown in Figure 15.

An ideal batch reactor and an ideal plug-flow reactor are considered. Mixing inside the reactors is assumed to be perfect, therefore mass transfer through the bulk of the liquid, steps 1 and 9 (cf. Figure 15), are considered instantaneous. It is also assumed that the resistance of the liquid film is negligible compared to the resistance due to diffusion inside the pores. Therefore, steps 2 and 8 are also considered instantaneous [95–98]. Due to these two assumptions, the concentrations at the entry of the pore are the same as the ones in the bulk of the liquid. It is assumed that mass transfer inside the pore takes place only by diffusion following Fick's law. Either first-order or Michaelis-Menten kinetics are used in the analysis. When first-order kinetics are used, the adsorption/desorption steps are considered instantaneous. By using Michaelis-Menten kinetics, the rates of the adsorption/desorption steps are taken implicitly into account.

The processes inside the pores are assumed to be significantly faster than the changes of the concentrations at the bulk of the liquid. From the viewpoint of the bulk, the pores themselves are assumed to be in quasi-steady state, a common assumption when studying porous particles [95–98]. This assumption is equivalent to assuming that there is little enzyme catalyst compared to the amount of substrate in the bulk of the reactor. Under these conditions, the apparent reaction rates of the macro-kinetics equal the rates of substrates diffusing into/out of the pores. This makes it possible to model the system with two decoupled systems of ordinary differential equations. One system is the material balances for the reactors. The other is the material balance along the pore, from which the apparent reaction rates are calculated.

4.2.4 Model equations

The molarity of substrate i ($i \in \{1, 2, 3\}$) in the bulk (index "0") is denoted with $S_{i,0}$. The respective molarity inside the pores is denoted $S_{i,n}$ with $n \in$ {α-A, α-B, β, γ, δ} denoting the type of pore. The molarities inside the pores are a function of the depth x which ranges from 0 (entry) to L (pore length). To define differential material balances for the bulk molarities $S_{i,0}$ in the batch reactor, the well-known ideas of Thiele (1939) [95, 99] are followed. Applying Fick's law at the entry of the pore, one obtains the diffusive molar flow-rates n_i^{D} of the substrates into/out of a single pore as shown in Equation (95):

$$n_i^{\mathrm{D}} = A \cdot D_i \cdot \frac{dS_{i,n}}{dt} \Big|_{x=0} \; \forall \; i \in \{1,2,3\} \tag{95}$$

In the above equation, A is the area of the cross section of the pores and D_i is the diffusivity of substrate i. $\frac{dS_{i,n}}{dt}$ is the gradient of substrate i's molarity along the pore. To obtain the change of substrate i in the bulk of the batch reactor, the diffusive molar flow rates over all pores are summed up as shown in Equation (96):

$$\frac{dS_{i,0}}{dt} = \sum_n N_n \cdot A \cdot D_i \cdot \frac{dS_{i,n}}{dx}\Big|_{x=0} \; \forall \; i \in \{1,2,3\} \tag{96}$$

Thereby it must be taken into account that these might be different types of pores (cf. Figure 14). In Equation (96), N_n is the total number of pores of type n in the reactor. The differential material balances in Equation (96) are solved over time $t = 0$ to $t = t_{\mathrm{f}}$, the total batch time. The initial molalities of substrates 2 and 3 are set to zero: $S_{2,0}|_{t=0} = S_{3,0}|_{t=0} = 0$. The initial molality $S_{1,0}|_{t=0}$ of substrate S_1 is treated as a parameter in the parametric study, cf. below.

Similarly, the change of substrate i in the bulk of the plug-flow reactor is calculated with Equation (97).

$$u \cdot \frac{dS_{\mathrm{i},0}}{dz} = \sum_n N_{\mathrm{n}} \cdot A \cdot D_{\mathrm{i}} \cdot \frac{dS_{\mathrm{i,n}}}{dx}\Bigg|_{x=0} \forall i \in \{1,\ 2,\ 3\} \tag{97}$$

In the above equation u is the average speed of the reaction solution while, z is the distance from the start of the packed-bed reactor. In cases where multiple zones are considered (cf. Figure 16), Equation (97) must be solved piece-wise for each zone.

The gradients of the molarities at the entry of the pore are calculated by solving the differential material balances for the cylindrical pores as follows. The material balances for the pores of type n, are given with compact matrix notation in Equation (98). The boundary conditions are given in Equations (99) and (100) and visualized in Figure 17.

$$\mathbf{D} \cdot \frac{d^2\mathbf{s}_n}{dx^2} = \mathbf{U} \cdot \mathbf{r}_n \tag{98}$$

$$\mathbf{s}_n\big|_{x=0} = \mathbf{s}_0 \tag{99}$$

$$\frac{d\mathbf{s}_n}{dx}\Big|_{x=L} = \mathbf{0} \tag{100}$$

where,

$$\mathbf{D} = \begin{bmatrix} D_1 & 0 & 0 \\ 0 & D_2 & 0 \\ 0 & 0 & D_3 \end{bmatrix},\ \mathbf{s}_n = \begin{bmatrix} S_{1,n} \\ S_{2,n} \\ S_{3,n} \end{bmatrix},\ \mathbf{U} = \begin{bmatrix} +1 & 0 \\ -1 & +1 \\ 0 & -1 \end{bmatrix},\ \mathbf{r}_n = \begin{bmatrix} r_{\mathrm{A},n} \\ r_{\mathrm{B},n} \end{bmatrix} \text{ and, } \mathbf{s}_0 = \begin{bmatrix} S_{1,0} \\ S_{2,0} \\ S_{3,0} \end{bmatrix}.$$

In Equation (98), a second order differential equation along the spatial coordinate x is considering diffusion and reaction. $\mathbf{D}$ is the matrix of diffusivities considering only entries on the main diagonal in the present work. That means that diffusion is assumed to be driven only by molarity gradients of the same substrate (this is a simplifying assumption and not a restriction of the method). The stoichiometry of the reactions A and B is given in matrix $\mathbf{U}$. The reaction rates $r_{j,n}$ with $j = $ A, B, are included in vector $\mathbf{r}_n$. Equation (99) links the substrate molarities at the entry of the pore to the substrate molarities in the bulk. Equation (100) ensures that the gradients of molarities, and thus the diffusion processes, come to zero at the dead end of the pore (cf. Figure 17).

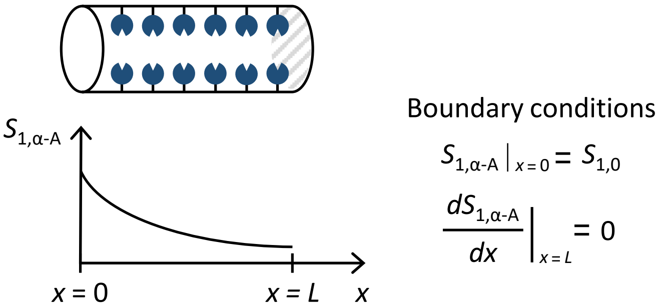

Figure 17: The concentration profile and the boundary conditions for substrate S_1 inside pore a – A.

The micro-kinetics of the enzyme catalyzed reactions are modeled either with first-order kinetics (Equation (101)) or with Michaelis-Menten kinetics (Equation (102)). The equations show the rates of reaction A as an example. Reaction B is analogous.

$$r_{\mathrm{A},n} = E_{\mathrm{A},n} \cdot k_{\mathrm{A}} \cdot S_{1,n} \tag{101}$$

$$r_{\mathrm{A},n} = \frac{E_{\mathrm{A},n} \cdot V_{\mathrm{A}}^{\max} \cdot S_{1,n}}{K_{\mathrm{A}} + S_{1,n}} \tag{102}$$

$E_{\mathrm{A},n}$ is the surface density of the immobilized enzyme A, k_{A} is the first-order kinetic constant, $V_{\mathrm{A}}^{\max}$ is the maximum reaction rate and K_{A} is the Michaelis-Menten constant for the enzyme catalyzed reaction.

4.2.5 Spatial immobilization distributions

The enzyme surface densities $E_{j,n}$ are functions of the depth x inside the pore. The individual profiles used for the SIDs shown in Figure 14 are presented in Table 2. They are normalized so that the total amount e_j of enzyme j in the reactor is equal for all SIDs, as shown in Equation (103).

$$e_j = \sum_n (N_n \cdot \sqrt{4\pi A} \cdot \int_{x=0}^{L} E_{j,n}(x)\, dx) \tag{103}$$

Table 2: Equations describing the spatial immobilization distributions.

Pore	Enzyme A	Enzyme B
α-A	$E_{\mathrm{A,a-A}}(x) = E_{\mathrm{A}}^{\max}$	$E_{\mathrm{B,a-A}}(x) = 0$
α-B	$E_{\mathrm{A,a-B}}(x) = 0$	$E_{\mathrm{B,a-B}}(x) = E_{\mathrm{B}}^{\max}$
β	$E_{\mathrm{A,b}}(x) = \frac{1}{2} \cdot E_{\mathrm{A}}^{\max}$	$E_{\mathrm{B,b}}(x) = \frac{1}{2} \cdot E_{\mathrm{B}}^{\max}$
γ	$E_{\mathrm{A,g}}(x) = -E_{\mathrm{A}}^{\max} \cdot \frac{x}{L} + E_{\mathrm{A}}^{\max}$	$E_{\mathrm{B,g}}(x) = E_{\mathrm{B}}^{\max} \cdot \frac{x}{L}$
δ	$E_{\mathrm{A,d}}(x) = E_{\mathrm{A}}^{\max} \cdot \frac{x}{L}$	$E_{\mathrm{B,d}}(x) = -E_{\mathrm{B}}^{\max} \cdot \frac{x}{L} + E_{\mathrm{B}}^{\max}$

4.2.6 Objectives and model parameters

The performances of different SIDs are compared against each other. As a measure of performance, the yield of the cascade's product S_3, Y_m ($m \in \{\alpha, \beta, \gamma, \delta\}$) at the end of the batch run is defined:

$$Y_m = \frac{S^m_{3,0}(t = t_\mathrm{f})}{S^m_{1,0}(t = 0)} \tag{104}$$

For continuous systems, this is calculated at the end of the reactor z_f.

$$Y_m = \frac{S_{3,0}(z = z_\mathrm{f})}{S_{1,0}(t = 0)} \tag{105}$$

When comparing two SIDs, the ratio of the achieved yields is calculated. For example, when comparing individual immobilization and co-immobilization, the ratio $\mathcal{R}_{\alpha/\beta}$ is calculated as shown in Equation (106).

$$\mathcal{R}_{\alpha/\beta} = \frac{Y_\alpha}{Y_\beta} \tag{106}$$

The same is done for continuous systems, but this time comparing different conceptual designs.

$$\mathcal{R}_{\mathrm{I/II}} = \frac{Y_\mathrm{I}}{Y_\mathrm{II}} \tag{107}$$

The SIDs' performances- and thus their relative performances - depend on the values of the model parameters. When using first-order kinetics (Michaelis-Menten kinetics), there are 16 (18) parameters. Table 3 gives an overview of all parameters along with physically reasonable bounds. Those bounds are either compiled from literature (if source is given) or based on experimental experience. Monte Carlo sampling is used in a parametric study to compare the SIDs. 2,000 sets of parameter values are sampled uniformly within the bounds using logarithmic scaling of the parameter interval to ensure that parameter values of all orders of magnitude will have the same probability to be selected. Each time, the reactor problem is simulated for all SIDs to determine Y_m. Exceptions are the cases of first-order kinetics for individual immobilization (α) and homogeneous co-immobilization (β) for which even analytical solutions for Y_m as a function of the parameters could be obtained.

Table 3: Parameter units and boundaries.

Variable	Units	Min	Max
	Geometric parameters		
A	dm^2	$3 \cdot 10^{-16}$	$2 \cdot 10^{-13}$ [100]
L	dm	10^{-6}	10^{-3} [101]
E_j^{max}	$\mu\mathrm{mol\ dm}^{-2}$	1	10
	Kinetic parameters		
k_j	$\mathrm{dm}^2\ \mu\mathrm{mol}^{-1}\ \mathrm{min}^{-1}$	0.1	1000
$V_j^{\max}$	$\mathrm{mM\ min}^{-1}\ \mathrm{dm}^2\ \mu\mathrm{mol}^{-1}$	0.1	1000
K_j	mM	0.1	50
	Physical property parameters		
D_i	$\mathrm{dm}^2\ \mathrm{min}^{-1}$	10^{-8}	10^{-5}[102]
	Batch reactor parameters		
$S_{1,0}(t=0)$	mM	1	1000
t_f	min	1	2000
N_n	-	10^{12}	10^{16}

4.2.7 Numerical implementation

Two separate systems of differential equations were solved using the SciPy package in Python. The first corresponds to the dynamic material balance inside the batch reactor. The second corresponds to the material balance in the pore. To solve the material balances for the batch reactor computationally, the solver LSODA was used. The second order differential equations representing the material balances in the pores were decoupled and solved as systems of first-order differential equations. The shooting method was applied for the solution and the solver solve_bvp was used. The gradient at the entry of the pore is calculated through solving the material balance for the pores. This gradient is then used to calculate the time profiles inside the batch reactor or the concentrations profiles inside the plug-flow reactor, as shown in Equations (96) and (97).

4.2.8 Application example

To demonstrate how the developed methodology can be applied to design the porous particles, an optimization problem is solved. Since no reliable experimental data were available, a synthetic example is studied. Parameter values are chosen to be inside bounds reported in literature (cf. Table 3). Therefore, for known values of all other parameters (given under Figure 26) the optimal SID inside the particles and the optimal enzyme surface densities are determined. The objective is to maximize the yield after 8 h. To achieve a fair comparison, the total amount of enzyme in the reactor (both enzyme A and B, $e_\mathrm{A} + e_\mathrm{B}$) is kept constant and smaller or equal to 158493 μmol. This is equivalent to keeping the sum $E_\mathrm{A}^{max} + E_\mathrm{B}^{max}$ smaller or equal to 10 μmol dm^2. The problem is solved by a brute-force search.

4.3 Results and discussion

4.3.1 Analytical solutions for dynamic processes

To start, the individual immobilization (SID α) is compared against the homogeneous co-immobilization (SID β) for first-order kinetics. Despite simple kinetics, qualitative statements are expected to be transferable to more complex kinetic expressions. An analytical solution was obtained for the time profiles inside the batch reactor when using first-order kinetics. The expressions representing the time profiles inside the batch reactor as well as their derivation are given in the supplementary material. The ratio $\mathcal{R}_{\alpha/\beta}$ results to:

$$\mathcal{R}_{\alpha/\beta}(t) = \frac{1 - e^{-p_{1,\alpha-\mathrm{A}}\cdot t} - \frac{p_{1,\alpha-\mathrm{A}}}{p_{2,\alpha-\mathrm{B}} - p_{1,\alpha-\mathrm{A}}} \cdot \left(e^{-p_{1,\alpha-\mathrm{A}}\cdot t} - e^{-p_{2,\alpha-\mathrm{B}}\cdot t}\right)}{1 - e^{-p_{1,\beta}\cdot t} - \frac{p_{1,\beta} - p_{3,\beta}}{p_{2,\beta} - p_{1,\beta}} \cdot \left(e^{-p_{1,\beta}\cdot t} - e^{-p_{2,\beta}\cdot t}\right)} \tag{108}$$

where,

$$p_{1,n} = N_n \cdot A \cdot D_1 \cdot m_{1,n} \cdot \tanh(m_{1,n} \cdot L), \tag{109}$$

$$m_{1,n} = \sqrt{\frac{E_{\mathrm{A},n} \cdot k_A}{D_1}}, \tag{110}$$

$$p_{2,n} = N_n \cdot A \cdot D_2 \cdot m_{2,n} \cdot \tanh(m_{2,n} \cdot L), \tag{111}$$

$$m_{2,n} = \sqrt{\frac{E_{\mathrm{B},n} \cdot k_B}{D_2}} \tag{112}$$

and,

$$p_{3,\beta} = \frac{N_\beta \cdot A \cdot D_1 \cdot m_{1,\beta}^2 \cdot m_{2,\beta}^2}{m_{1,\beta}^2 - m_{2,\beta}^2} \cdot \left[\frac{\tanh(m_{2,\beta} \cdot L)}{m_{2,\beta}} - \frac{\tanh(m_{1,\beta} \cdot L)}{m_{1,\beta}}\right] \tag{113}$$

It is interesting to note that the products $m_{1,n} \cdot L$ and $m_{2,n} \cdot L$ in the above equations are the Thiele moduli for the first and second steps of the cascade respectively. The value of $\mathcal{R}_{\alpha/\beta}$ is independent of $S_{1,0}|_{t=0}$ and, D_3. Thus, the extent of the advantage of co-immobilization during the reaction processes is independent of the initial concentration of substrate or the diffusivity of the product. Equation (108) is plotted in a contour plot in Figure 18 to display the dependence of $\mathcal{R}_{\alpha/\beta}$ and of Y_β on the diffusivities D_1 and D_2. The reaction kinetics are chosen fast in Figure 18. Under these conditions, $\mathcal{R}_{\alpha/\beta}$ depends on both diffusivities D_1 and D_2. The dependence on diffusivity D_2 is stronger. The smaller the diffusivities, the more significant the advantage of co-immobilization becomes.

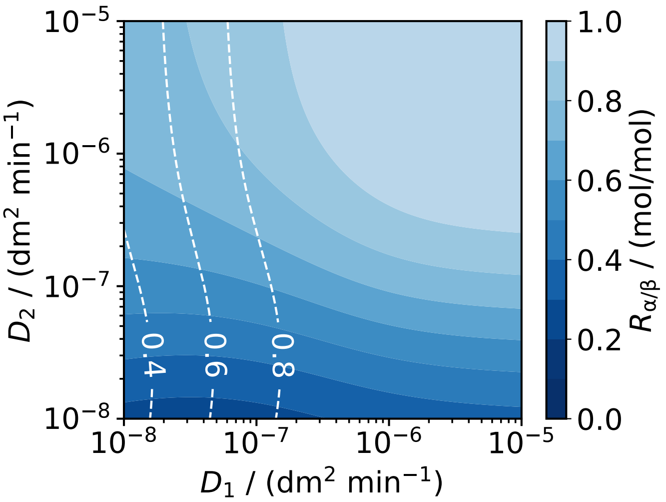

Figure 18: Contour plot of $\mathcal{R}_{\alpha/\beta}$ and Y_β for different diffusivity values. $A = 10^{-13}$ dm^2, $L = 5 \cdot 10^{-4}$ dm, $\mathrm{E}_\mathrm{A}^{max} = 6$ μmol dm^{-2}, $\mathrm{E}_\mathrm{B}^{max} = 6$ μmol dm^{-2}, $k_A = 1000$ dm^2 μmol^{-1} min^{-1}, $k_B = 998$ dm^2 μmol^{-1} min^{-1}, $t_\mathrm{f} = 250$ min, $N_{\alpha\text{-A}} = 2.5 \cdot 10^{12}$ -, $N_{\alpha\text{-B}} = 2.5 \cdot 10^{12}$ -, $N_\beta = 5 \cdot 10^{12}$ -. $\mathcal{R}_{\alpha/\beta}$ is shown with colors while Y_β is shown with the white dashed lines.

The ratio $\mathcal{R}_{\alpha/\beta}$ and Y_β as a function of time for different values of D_2 is presented in Figure 19. For sufficiently large time horizons, individual immobilization always catches up with co-immobilization. However, some differentiation can be made: for fast diffusivities of the intermediate S_2 ($D_2 = 10^{-5}$ dm^2 min^{-1}), single optimization catches up ($\mathcal{R}_{\alpha/\beta}$ tending to 1) while the yields are still quite low (60%-80%) . For very slow diffusivities though, a high yield Y_β could be obtained with co-immobilization while the individual immobilization has made no significant yield yet ($\mathcal{R}_{\alpha/\beta}$ tending to 0).

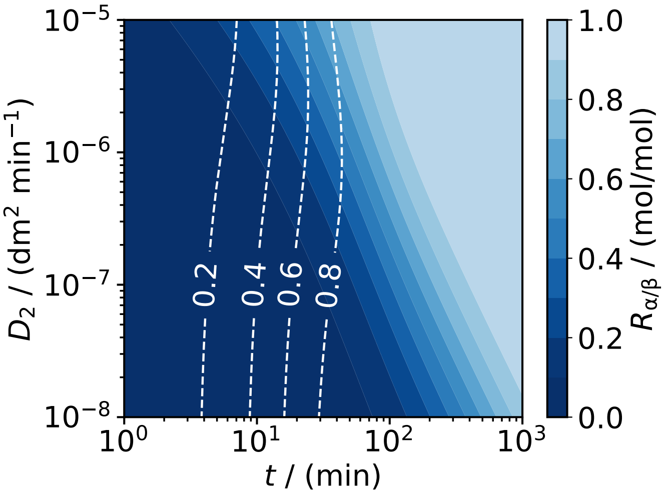

Figure 19: Contour plot of $\mathcal{R}_{\alpha/\beta}$ and Y_β for different diffusivity values and at different times. $A = 10^{-13}$ dm^2, $L = 5 \cdot 10^{-4}$ dm, $E_A^{max} = 6$ μmol dm^{-2}, $E_B^{max} = 6$ μmol dm^{-2}, $k_A = 1000$ dm^2 μmol^{-1} min^{-1}, $k_B = 998$ dm^2 μmol^{-1} min^{-1}, $D_1 = 5 \cdot 10^{-6}$ dm^2 min^{-1}, $N_{\alpha\text{-A}} = 2.5 \cdot 10^{12}$ -, $N_{\alpha\text{-B}} = 2.5 \cdot 10^{12}$ -, $N_\beta = 5 \cdot 10^{12}$ -. $\mathcal{R}_{\alpha/\beta}$ is shown with colors while Y_β is shown with the white dashed lines.

The dependence of the ratio $\mathcal{R}_{\alpha/\beta}$ and Y_β on the pore dimensions is represented in Figure 20. The advantage of co-immobilization is more pronounced for long pores and small cross sections. Therefore, as expected, the advantage is larger when conditions for diffusion are hard. Only for pores longer than 10^{-4} dm, high yields of co-immobilization are obtained while the yields in individual co-immobilization are still low. Note that the given numbers are subject to change if the kinetic parameters / diffusivities change.

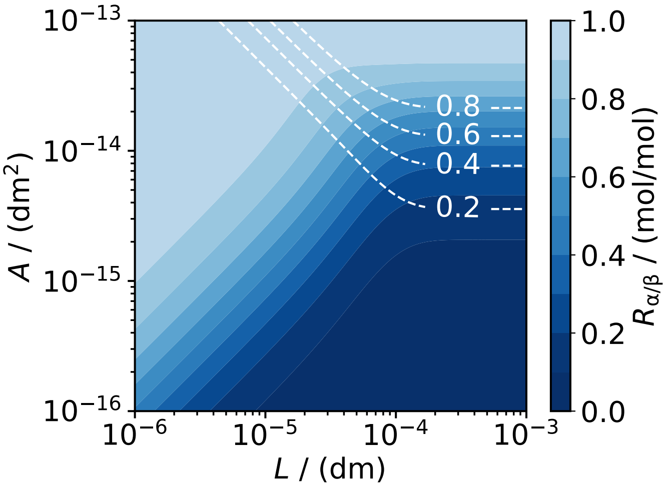

Figure 20: Contour plot of $\mathcal{R}_{\alpha/\beta}$ and Y_β for different pore dimensions. $A = 10^{-13}$ dm^2, $L = 5 \cdot 10^{-4}$ dm, $E_A^{max} = 6$ μmol dm^{-2}, $E_B^{max} = 6$ μmol dm^{-2}, $k_A = 500$dm^2 μmol^{-1} min^{-1}, $k_B = 500$ dm^2 μmol^{-1} min^{-1}, $D_1 = 5.5 \cdot 10^{-6}$ dm^2 min^{-1}, $D_2 = 5 \cdot 10^{-6}$ dm^2 min^{-1}, $t_f = 250$ min, $N_{\alpha-A} = 2.5 \cdot 10^{12}$ -, $N_{\alpha-B} = 2.5 \cdot 10^{12}$ -, $N_\beta = 5 \cdot 10^{12}$ -. $\mathcal{R}_{\alpha/\beta}$ is shown with colors while Y_β is shown with the white dashed lines.

The Equations (108)- (113), are greatly simplified under two assumptions: a) the products $m_{1,n} \cdot L$ and $m_{2,n} \cdot L$ (i.e. the Thiele moduli for steps one and two of the cascade) are larger than one, which is true for the majority of combinations in our parametric study, and, b) when $D = D_1 = D_2$. Assumption b) is plausible if cases are considered where the substrates S_1 and S_2 are of similar molecular structure. The results is shown in Equation (114). $\mathcal{R}_{\alpha/\beta}$ is a function of two moduli μ_1 and μ_2 (cf. Equations (115) and (116)). The complete derivation is given in the Appendix C.

$$\mathcal{R}_{\alpha/\beta}(t) = \frac{1 - e^{-\mu_1} - \frac{\mu_1}{\mu_2 - \mu_1} \cdot \left(e^{-\mu_1} - e^{-\mu_2}\right)}{1 - e^{-\sqrt{2} \cdot \mu_1} - \frac{\mu_1^2}{\mu_2^2 - \mu_1^2} \cdot \left(e^{-\sqrt{2} \cdot \mu_1} - e^{-\sqrt{2} \cdot \mu_2}\right)} \tag{114}$$

where,

$$\mu_1 = N_{\alpha-A} \cdot A \cdot t \cdot \sqrt{E_{A,\alpha-A} \cdot k_A \cdot D} \tag{115}$$

$$\mu_2 = N_{\alpha-B} \cdot A \cdot t \cdot \sqrt{E_{B,\alpha-B} \cdot k_B \cdot D} \tag{116}$$

The ratio $\mathcal{R}_{\alpha/\beta}$ and Y_β as a function of μ_1 and μ_2 is presented in Figure 21. For small values of the moduli, $\mathcal{R}_{\alpha/\beta}$ takes a small value, while for large values of the moduli,

$\mathcal{R}_{\alpha/\beta}$ takes a large value. This means that co-immobilization mostly has a comparative advantage for low values of the moduli. However, for these small values of the moduli only small yields, Y_β can be achieved. Therefore, for the simplified case, with $m_{1,\mathrm{n}} \cdot L$ and $m_{2,\mathrm{n}} \cdot L$ larger than one and $D_1 = D_2 = D$ it is impossible to have a large advantage of co-immobilization and a large yield achieved with co-immobilization simultaneously. Under these conditions co-immobilization, provides no significant kinetic advantage.

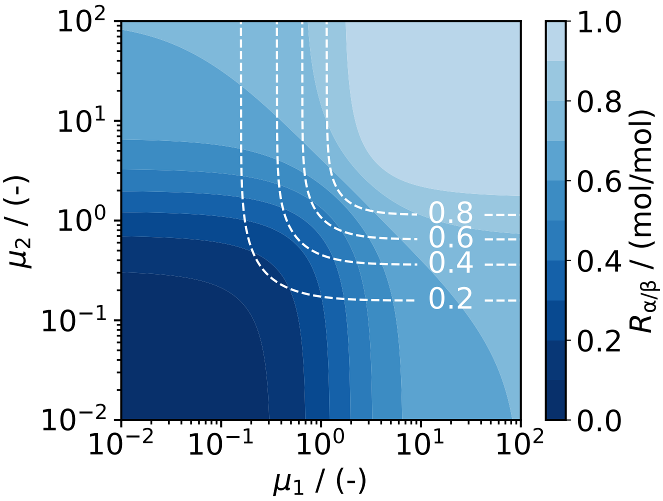

Figure 21: Contour plot of $\mathcal{R}_{\alpha/\beta}$ for different values of moduli μ_1 and μ_2 for $D_1 = D_2 = D$ and omitted tangent hyperbolicus terms. $\mathcal{R}_{\alpha/\beta}$ is shown with colors while Y_β is shown with the white dashed lines.

4.3.2 Analytical solutions for continuous processes

The model equations are solved analytically to derive equations that describe the concentration profiles inside the packed-bed reactor achieved with the three different designs. The yields that are achieved with the three different designs as a function of all the model parameters are presented as follows.

$$Y_\mathrm{I} = 1 - e^{-p_{1,\alpha\text{-A}}} - \frac{p_{1,\alpha\text{-A}}}{p_{2,\alpha\text{-B}} - p_{1,\alpha\text{-A}}} \cdot \left(e^{-p_{1,\alpha\text{-A}}} - e^{-p_{2,\alpha\text{-B}}}\right),\ \forall \tau \in [0, \tau_\mathrm{f}] \tag{117}$$

$$Y_\mathrm{II} = \left\{ \begin{array}{ll} 0 & \forall \tau \in \left[0, \frac{\tau_\mathrm{f}}{c}\right] \\ \left(1 - e^{-p_{1,\mathrm{a\text{-}A}} \cdot \tau}\right) \cdot \left(1 - e^{-c \cdot p_{2,\mathrm{a\text{-}B}} \cdot \left(\tau - \frac{\tau_\mathrm{f}}{c}\right)}\right), & \forall \tau \in \left[\frac{\tau_\mathrm{f}}{c}, \tau_\mathrm{f}\right] \end{array} \right\} \tag{118}$$

$$Y_\mathrm{III} = 1 - e^{-p_{1,\beta}} - \frac{p_{1,\beta} - p_{3,\beta}}{p_{2,\beta} - p_{1,\beta}} \cdot \left(e^{-p_{1,\beta}} - e^{-p_{2,\beta}}\right),\ \forall \tau \in [0, \tau_\mathrm{f}] \tag{119}$$

where,

$$\tau = \frac{z}{u} \tag{120}$$

$$p_{1,\mathrm{n}} = N_{\mathrm{n}} \cdot A \cdot D_1 \cdot m_{1,\mathrm{n}} \cdot \tanh(m_{1,\mathrm{n}} \cdot L) \tag{121}$$

$$m_{1,\mathrm{n}} = \sqrt{\frac{E_{\mathrm{A,n}} \cdot k_{\mathrm{A}}}{D_1}} \tag{122}$$

$$p_{2,\mathrm{n}} = N_{\mathrm{n}} \cdot A \cdot D_2 \cdot m_{2,\mathrm{n}} \cdot \tanh(m_{2,\mathrm{n}} \cdot L) \tag{123}$$

$$m_{2,\mathrm{n}} = \sqrt{\frac{E_{\mathrm{B,n}} \cdot k_{\mathrm{B}}}{D_2}} \tag{124}$$

$$p_{3,\beta} = \frac{N_{\beta} \cdot A \cdot D_1 \cdot m_{1,\beta}^2 \cdot m_{2,\beta}^2}{m_{1,\beta}^2 - m_{2,\beta}^2} \cdot \left[\frac{\tanh(m_{2,\beta} \cdot L)}{m_{2,\beta}} - \frac{\tanh(m_{1,\beta} \cdot L)}{m_{1,\beta}} \right] \tag{125}$$

Note that Y_{I}, Y_{II} and Y_{III} depend on all considered parameters and exhibit a strong dependency on the diffusivities and the reaction kinetic parameters. In order to calculate the product yields the parameter values have to be known. For known values of all parameters the product yield is plotted against the residence time for an arbitrary case in Figure 22.

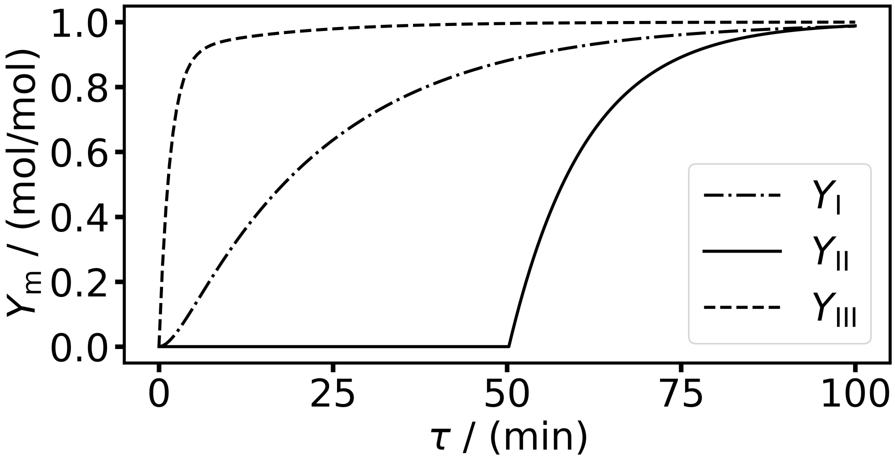

Figure 22: The yields achieved with designs I-III plotted against the residence time. The parameters have values: $D_1 = 10^{-5}$ dm^2 min^{-1}, $D_2 = 10^{-7}$ dm^2 min^{-1}, $k_A = 2000$ dm^2 μmol^{-1} min^{-1}, $k_B = 2000$ dm^2 μmol^{-1} min^{-1}, $L = 10^{-4}$ dm, $N_{\alpha\text{–A}} = 10^{13}$ dm^{-3}, $N_{\alpha\text{–B}} = 10^{13}$ dm^{-3}, $N_\beta = 2\ 10^{13}$ dm^{-3}, $E_{A,\alpha\text{–A}} = 10$ μmol dm^{-2}, $E_{B,\alpha\text{–B}} = 10$ μmol dm^{-2}, $E_{A,\beta} = 5$ μmol dm^{-2}, $E_{B,\beta} = 5$ μmol dm^{-2}, $c = 2$. Note that in the above case study, the intermediate has a much lower diffusivity than the first substrate.

Note that the presented case corresponds to the selected parameter values and will look quantitatively different for other parameter values. Design III reaches large yields significantly faster than designs I and II. Design I gets ahead of design II at small resident times, since for $\tau < 50$ min, the reaction solution in design II has not yet come in contact with α-B porous particles and therefore no product has been produced. Design II catches up and slightly surpasses design I before the final residence time (100 min) is reached. Note that if a final residence time smaller than 100 min was chosen, the second zone, containing α-B porous particles, would have started earlier in design II and the solid black curve would look different. A comparison of the three designs evaluated at different final resident times, τ_f is given in the Appendix C.

Generally, it can be proven (c.f. Appendix C for the complete proof), that design II (i.e., two separated zones) is always better than design I (i.e., one mixed zone of individually immobilized enzymes) for any positive order reaction kinetics (i.e. the reaction rate increases monotonically with increasing substrate concentrations). For such kinetic models, design II will always reach a higher product yield than design I when the final residence time, τ_f is reached. This proof is not restricted to two steps and extends, by induction, to any number of reaction steps. This observation can be written as a theorem like shown below.

Theorem 4: Zone design.
For any positive order kinetic model, the achieved conversion is always higher when seperating the two catalysts of a two-step sequential (cascade) reaction in two separate zones instead of mixing them in one in a plug-flow reactor.

The substrates often have a similar chemical structure and diffusivities. Further, in cases where reaction is sufficiently faster than diffusion and the pores are sufficiently long, the Thiele moduli become larger than one and the tangent hyperbolicus of these product becomes equal to one. The algebraic equations representing the yield for the third design simplify greatly under these two assumptions, i.e.: a) the products $m_{1,\mathrm{n}}$ $\cdot L$, and $m_{2,\mathrm{n}}$ $\cdot L$ (i.e., the Thiele moduli for steps one and two of the cascade) are larger than one, which is true for the majority of combinations in the parametric study, and, b) when $D = D_1 = D_2$. Under these conditions, Equations (-) can be rewritten as follows (for $\tau = \tau_\mathrm{f}$):

$$Y_\mathrm{I} = 1 - e^{-\mu_1} - \frac{\mu_1}{\mu_2 - \mu_1} \cdot \left(e^{-\mu_1} - e^{-\mu_2}\right) \tag{126}$$

$$Y_\mathrm{II} = \left(1 - e^{-\mu_1}\right) \cdot \left(1 - e^{-\mu_2}\right) \tag{127}$$

$$Y_\mathrm{III} = 1 - e^{-\sqrt{2}\cdot\mu_1} - \frac{\mu_1^2}{\mu_2^2 - \mu_1^2} \cdot \left(e^{-\sqrt{2}\cdot\mu_1} - e^{-\sqrt{2}\cdot\mu_2}\right) \tag{128}$$

where,

$$\mu_1 = N_\text{a-A} \cdot A \cdot \sqrt{E_\text{A,a-A} \cdot k_\mathrm{A} \cdot D} \cdot \tau_\mathrm{f} \tag{129}$$

$$\mu_2 = N_\text{a-B} \cdot A \cdot \sqrt{E_\text{B,a-B} \cdot k_\mathrm{B} \cdot D} \cdot \tau_\mathrm{f} \tag{130}$$

Next designs I and II are compared. In design I, particles containing individually immobilized enzymes are mixed together in one zone of the reactor. In design II, particles containing individually immobilized enzymes are separated to two separate zones. As mentioned earlier, design II always outperforms design I for positive order kinetics. Here, the results obtained by analytical solutions are presented, when first-order micro-kinetics and consequently first-order macro-kinetics are considered. The ratio $R_\mathrm{I/II}$ and Y_II as a function of μ_1 and μ_2 are presented in Figure 23. For small values of μ_1 and

μ_2, $R_{\mathrm{I/II}}$ takes a small value, while for large values of μ_1 and μ_2, $R_{\mathrm{I/II}}$ approaches unity. This means that design II has mostly an advantage for low values of the moduli. A large advantage of design II and a high yield of design II can however not be achieved simultaneously. Though using separated zones is advantageous over using one mixed zone, the kinetic advantage is relatively small for first-order macro kinetics. Note that when the reaction micro-kinetics follow higher order kinetic models, design II might exhibit a stronger advantage.

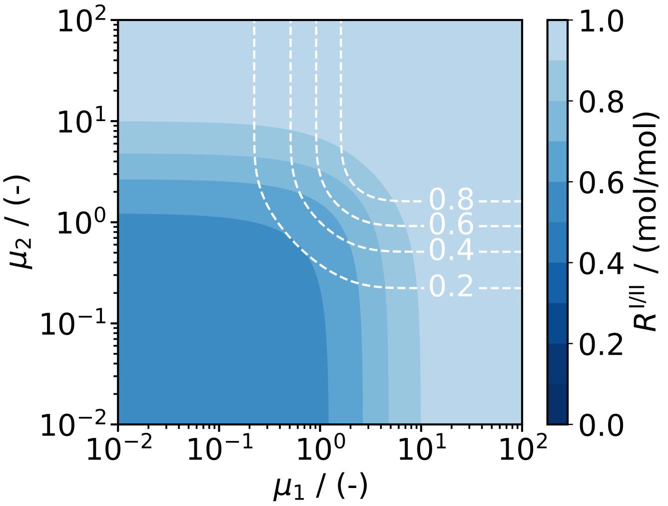

Figure 23: Contour plot of $\mathcal{R}_{\alpha/\beta}$ for different values of moduli μ_1 and μ_2 for $D_1 = D_2 = D$ and omitted tangent hyperbolicus terms. $\mathcal{R}_{\alpha/\beta}$ is shown with colors while Y_β is shown with the white dashed lines.

Then designs I and III are compared. The ratio $R_{\mathrm{I/III}}$ and Y_{III} as a function of the moduli μ_1 and μ_2 is presented in Figure 24. For small values of μ_1 and μ_2, $R_{\mathrm{I/III}}$ takes a small value, while for large values of μ_1 and μ_2, $R_{\mathrm{I/III}}$ takes a large value. This means that design III (i.e., co-immobilization) has mostly an advantage for low values of the moduli. However, for these small values of the moduli only small yields, Y_{III} can be achieved. Therefore, for the simplified case, with $m_{1,n} \cdot L$ and $m_{2,n} \cdot L$ larger than one and $D = D_1 = D_2$ it is impossible to have a large advantage of co-immobilization and a large yield achieved with co-immobilization simultaneously. Under these conditions design III, provides only a small kinetic advantage.

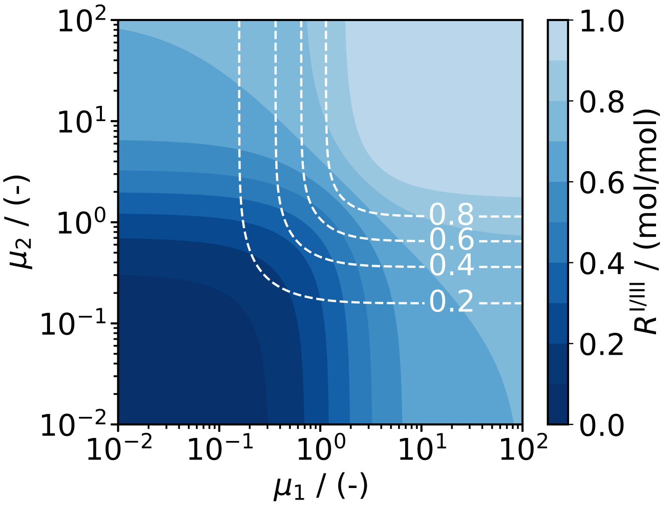

Figure 24: Contour plot of $\mathcal{R}_{\alpha/\beta}$ for different values of moduli μ_1 and μ_2 for $D_1 = D_2 = D$ and omitted tangent hyperbolicus terms. $\mathcal{R}_{\alpha/\beta}$ is shown with colors while Y_β is shown with the white dashed lines.

Finally, designs II and III are compared. In design II, particles containing individually immobilized enzymes are separated into two separate zones. In design III, particles containing co-immobilized enzymes are mixed together in one zone of the reactor. The ratio $R_{\text{II/III}}$ and Y_{III} as a function of μ_1 and μ_2 is presented in Figure 25. Again, large advantages only exist for relatively small yields.

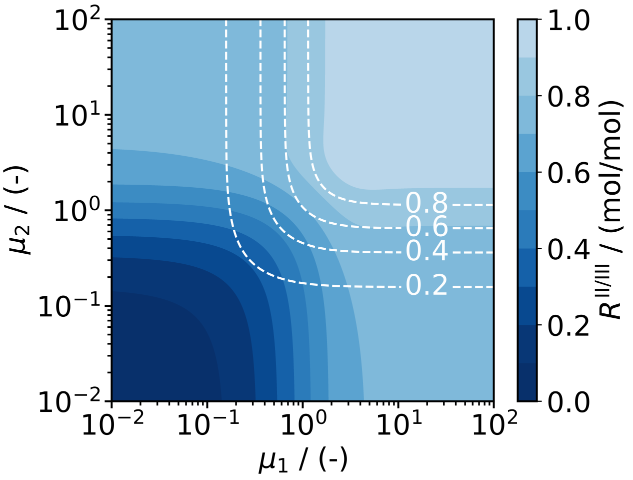

Figure 25: Contour plot of $\mathcal{R}_{\alpha/\beta}$ for different values of moduli μ_1 and μ_2 for $D_1 = D_2 = D$ and omitted tangent hyperbolicus terms. $\mathcal{R}_{\alpha/\beta}$ is shown with colors while Y_β is shown with the white dashed lines.

4.3.3 Monte Carlo sampling for dynamic processes

Monte Carlo sampling allows us to compare also other SIDs and kinetics. Here this is applied to compare SIDs for the batch reactor system. Randomly sampled scenarios of individual immobilization with co-immobilization for both first-order and Michaelis-Menten kinetics and 2,000 randomly sampled sets of parameters were compared. The results for the yields that are achieved in the batch reactor are then plotted in parity plots in Figure 23a) and 24a). Both for first-order and for Michaelis-Menten kinetics, all points fall either above or on the diagonal, which indicates that co-immobilization is always better or equal to individual immobilization for the studied problem.

Let us assume, that it is not possible to achieve homogeneous co-immobilization due to experimental restrictions. E.g., because the enzymes A and B are immobilized one after another, the enzyme surface densities are a function of pore depth as in SIDs γ and δ (cf. Table 2). If A (B) is immobilized first, obtain SID γ (δ) is obtained. Figures 23b) and c) tell how much worse these heterogeneous distributions are compared to the homogeneous ideal. Figure 23d) shows the direct comparison between the SIDs $\gamma$and δ(the respective results for Michaelis-Menten kinetics are qualitatively similar and shown in 24b), c) and d)). In Figures 23b) and c), most points fall above the diagonal while a small number of points falls bellow it. The points that fall above the diagonal correspond to cases where the yield achieved with homogeneous co-immobilization is better than the one achieved with heterogeneous co-immobilization. Each point is color-coded based on the modulus f_{FOK}.

$$f_{\mathrm{FOK}} = \frac{E_{\mathrm{A}}^{max} \cdot k_{\mathrm{A}} \cdot D_1}{E_{\mathrm{B}}^{max} \cdot k_{\mathrm{B}} \cdot D_2} \tag{131}$$

Modulus f_{FOK} relates the overall rates (combining diffusion and reaction) of cascade steps A and B. A large value of f_{FOK} indicates that the reaction of step A is fast (large amount of enzyme A and fast kinetic constant) and/or the diffusion of the respective substrate is fast, compared to step B. Under these conditions, SID δ with A immobilized deeper in the pores is generally better, cf. Figure 23d). For large values of f_{FOK}, SID $\delta$is sometimes even outperforming the homogeneous co-immobilization, cf. Figure 23c). For small values of f_{FOK} the opposite results are obtained, cf. Figure 23b) and d). To sum up: if there is one step in the cascade that has a handicap (e.g., mass transfer limitations, slow kinetics, expensive enzymes), the respective enzymes should be put rather at the entry of the pore. The same trend is not observed for Michaelis-Menten kinetics. The same comparisons were executed for Michaelis-Menten kinetics (Figures 24b)-d)) and the points were color-coded based on a similar modulus f_{MMK}.

$$f_{\mathrm{MMK}} = \frac{E_{\mathrm{A}}^{max} \cdot V_{\mathrm{A}}^{\max} \cdot D_1}{E_{\mathrm{B}}^{max} \cdot V_{\mathrm{B}}^{\max} \cdot D_2} \tag{132}$$

The trends observed for first-order kinetics are not as clear but also seen in the plots of the Michaelis-Menten kinetics (MMK). Most of the points are close to the diagonal indicating that the order of immobilization inside the pore is not so decisive. This can be explained by the generally slower reaction kinetics observed in MMK through consideration of the adsorption/desorption steps compared to faster first-order kinetics. In the Michaelis-Menten comparison plots, the reaction kinetics are almost never faster than diffusion. For this reason differences between the SID is observed in very few cases.

4.3.4 Model-based optimization

It is demonstrated how the developed model can be applied to solve a combinatorial optimization problem. The yields that can be achieved with SIDs α, β, γ and δ are presented in Figure 26. SID γoutperforms the other strategies for all considered enzyme ratios. The optimal solution was found to be 8.8 μmol dm^{-2} of enzyme A and 1.2 μmol dm^{-2} of enzyme B while using SID γ. In the studied problem, individual immobilization (SID α) outperformed heterogeneous co-immobilization with B at the entry of the pore (SID δ).

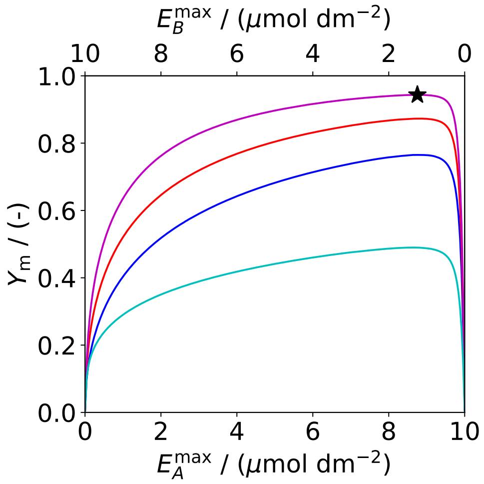

Figure 26: Yields achieved with three different immobilization strategies plotted against time. ——: SID α, ——: SID β, ——: SID γ, ——: SID δ. The star shows the optimal solution. Parameter values: $A = 8 \cdot 10^{-15}$ dm^2, $L = 2 \cdot 10^{-4}$ dm, $k_{\mathrm{A}} = 30$ dm^2 μmol^{-1} min^{-1}, $k_{\mathrm{B}} = 80$ dm^2 μmol^{-1} min^{-1}, $D_1 = 10^{-8}$ dm^2 min^{-1}, $D_2 = 5 \cdot 10^{-6}$ dm^2 min^{-1}, $D_3 = 5 \cdot 10^{-6}$ dm^2 min^{-1}, $S_{1,0}(t = 0) = 1000$ mM, $t_{\mathrm{f}} = 480$ min, $N_{\alpha\text{-A}} = 2.5 \cdot 10^{14}$ -, $N_{\alpha\text{-B}} = 2.5 \cdot 10^{14}$ -, $N_{\beta} = 5 \cdot 10^{14}$ -, $N_{\gamma} = 5 \cdot 10^{14}$ -, $N_{\delta} = 5 \cdot 10^{14}$ -.

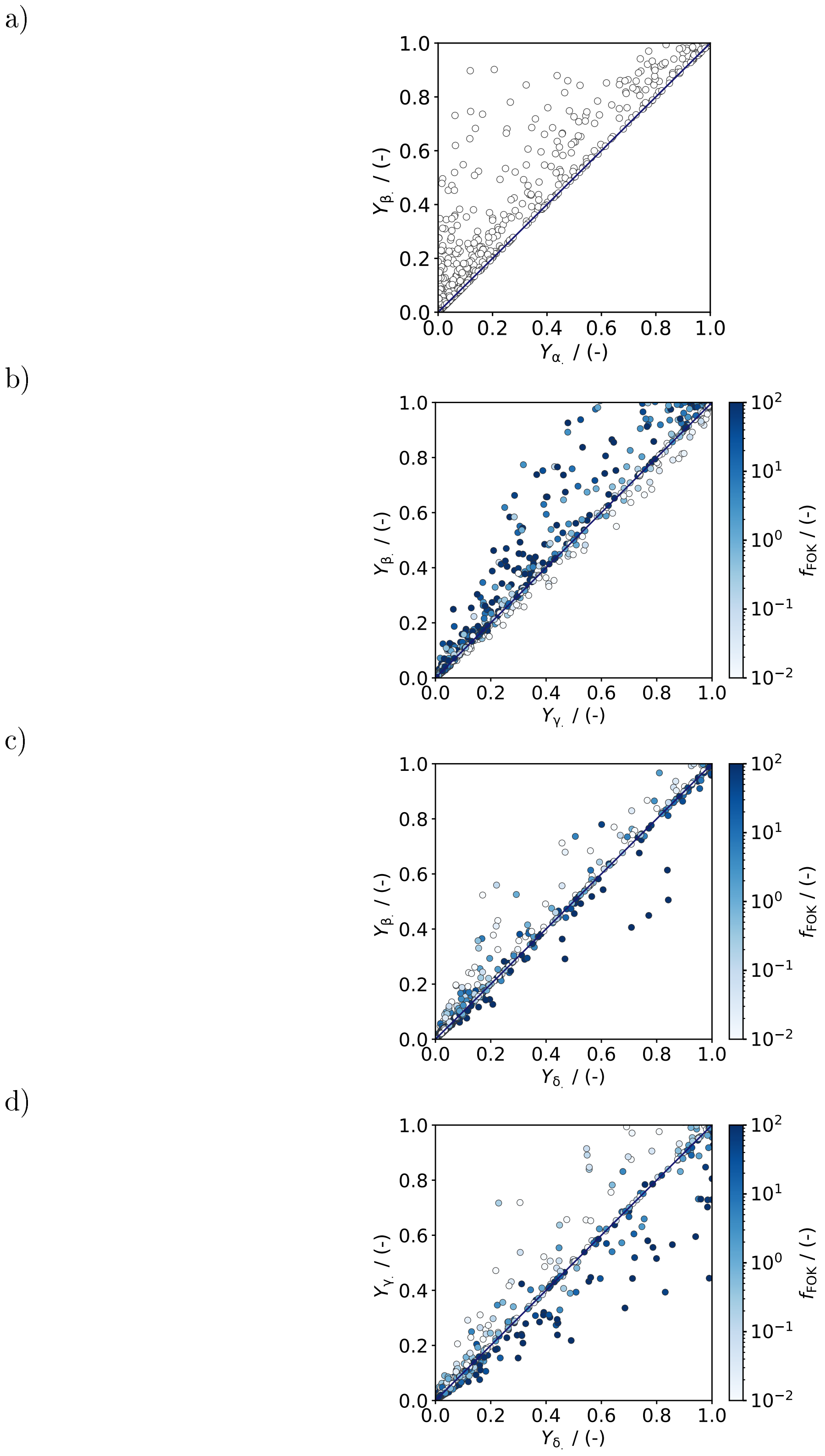

Figure 27: Results of the parametric study for the comparison of the different co-immobilization SIDs using first-order kinetics. a) Comparison of α to β. b) Comparison of β to γ. c) Comparison of β to δ. d) Comparison of γ to δ. All parameters are varied inside the bounds presented in Table 3.

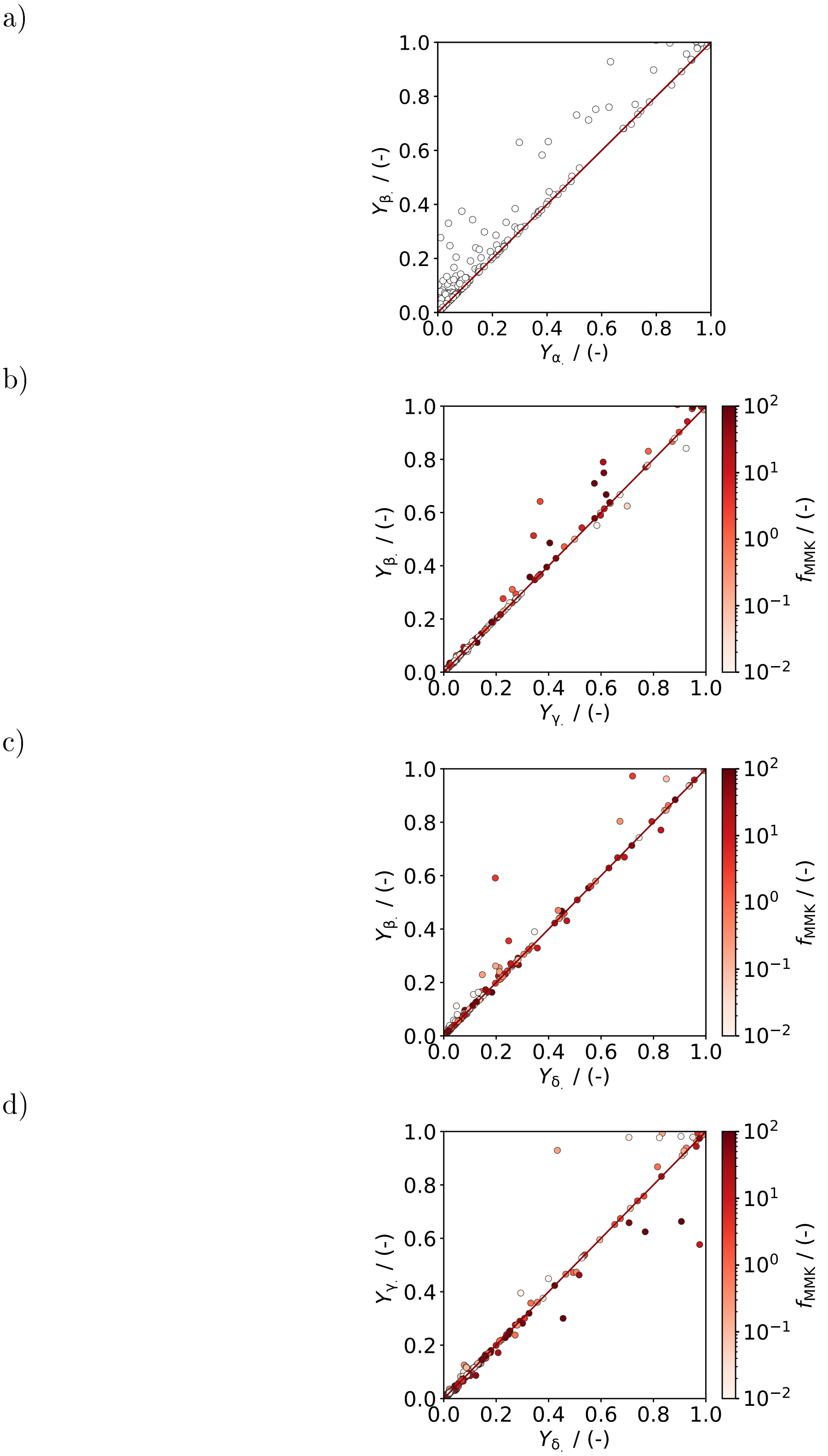

Figure 28: Results of the parametric study for the comparison of the different co-immobilization SIDs using Michaelis-Menten kinetics. a) Comparison of α to β. b) Comparison of β to γ. c) Comparison of β to δ. d) Comparison of γ to δ. All parameters are varied inside the bounds presented in Table 3.

5 Conclusions

The present work developed and applied methodologies for modeling, theoretical analysis and model-based optimization for several problems that arise in the design of enzymatic cascade reaction processes. Firstly, model-based optimization was applied to a reaction process that produces α-ketoglutarate. How such a reaction process is designed through multi-objective optimization (MOO) and the determination of Pareto frontiers was demonstrated. A simulation model to run the cascade in a batch reactor was derived and used in process optimization. This dynamic process has many control parameters, which would be very expensive to vary experimentally. The simulation-based approach enables the evaluation of a large number of conceivable process schedules. Space-time yield, enzyme consumption, and cofactor consumption were used as separate objectives in the MOO problem. The space-time yield in the studied process reached a maximum value of up to 2.88 mM/min, however only for very high enzyme consumption. Enzyme consumption can be significantly lowered to 0.4 μM/min while keeping the space-time yield as high as 2.44 mM/min.

Further, the dynamic bevavior of redox cascade reactions was analyzed and a phenomenon called boosting by intermediates was explaned based on kinetic models. It was demonstrated that studying complex enzymatic cascade reaction networks under the quasi-steady state approximation can help debottleneck them without the need for simulations. Further, it was shown that combining information from the material balance with the quasi steady state approximation which intermediates might boost or delay a cascade can be deduced. For linear cascades this can be achieved graphically with a novel graphical method.

For systems with immobilized enzymes, a mechanistic modeling methodology for heterogeneous reaction processes catalyzed by enzymes immobilized inside porous particles was developed. The developed method was used to answer some theoretical questions about co-immobilization in dynamic batch processes. Algebraic equations describing the amount of product produced with individual immobilization and homogeneous co-immobilization were derived by solving the system of differential equations analytically. The effect of different parameters on the ratio of the yields achieved with individual immobilization and co-immobilization was studied for the first time. For co-immobilization, three different co-immobilization spatial distributions were studied and compared. Also, an optimization problem was solved to demonstrate how the developed methodology can be applied to design the porous particles in such reaction processes.

Finally, the mechanistic modeling methodology for immobilized enzyme systems was extended to continuous processes and flow reactors. Different designs of multi-zone reactors that contain particles with immobilized enzymes were compared and the conditions under which the different designs are adventageous were deduced.

Overall, the thesis demonstrates the advantages of using kinetic models in decision making processes on the design of enzymatic cascade reactors. Both parameterized and non-parameterized models can help design such processes either through model-based optimization or by studying the kinetic models themselves and extracting theoretical insights.

Future work could develop theory and model-based optimization approaches for continuous systems with dissolved enzymes. In particular, systems with disolved enzymes in membrane reactors are of interest. A membrane reactor can help retain the enzymes and separate the products of the cascade. Furthermore, parameterized models for systems with immobilized enzymes can be developed to design both dynamic and continuous processes. Finally, testing whether boosting by intermediates can be used in systems with immobilized enzymes is of interest.

Literature

[1] W. Kroutil, M. Rueping: Introduction to ACS Catalysis Virtual Special Issue on Cascade Catalysis, ACS Catalysis 4 (2014) 2086–2087.

[2] J. H. Schrittwieser, S. Velikogne, M. Hall, W. Kroutil: Artificial Biocatalytic Linear Cascades for Preparation of Organic Molecules, Chemical Reviews 118 (2018) 270–348.

[3] J. M. Sperl, V. Sieber: Multienzyme Cascade Reactions-Status and Recent Advances, ACS Catalysis 8 (2018) 2385–2396.

[4] J.-K. Guterl, D. Garbe, J. Carsten, F. Steffler, B. Sommer, S. Reisse, A. Philipp, M. Haack, B. Rühmann, A. Koltermann, U. Kettling, T. Brück, V. Sieber: Cell-Free Metabolic Engineering: Production of Chemicals by Minimized Reaction Cascades, ChemSusChem 5 (2012) 2165–2172.

[5] N. Losada-Garcia, Z. Cabrera, P. Urrutia, C. Garcia-Sanz, A. Andreu, J. M. Palomo: Recent Advances in Enzymatic and Chemoenzymatic Cascade Processes, Catalysts 10 (2020).

[6] Y. Liu, P. Liu, S. Gao, Z. Wang, P. Luan, J. González-Sabín, Y. Jiang: Construction of chemoenzymatic cascade reactions for bridging chemocatalysis and Biocatalysis: Principles, strategies and prospective, Chemical Engineering Journal 420 (2021) 127659.

[7] E. Ricca, B. Brucher, J. H. Schrittwieser: Multi-Enzymatic Cascade Reactions: Overview and Perspectives, Advanced Synthesis & Catalysis 353 (2011) 2239–2262.

[8] B. Beer, A. Pick, V. Sieber: In vitro metabolic engineering for the production of a-ketoglutarate, Metabolic Engineering 40 (2017) 5–13.

[9] L. Shen, M. Kohlhaas, J. Enoki, R. Meier, B. Schönenberger, R. Wohlgemuth, R. Kourist, F. Niemeyer, D. van Niekerk, C. Bräsen, J. Niemeyer, J. Snoep,

B. Siebers: A combined experimental and modelling approach for the Weimberg pathway optimisation, Nature Communications 11 (2020) 1098.

[10] T. J. Gmelch, J. M. Sperl, V. Sieber: Optimization of a reduced enzymatic reaction cascade for the production of L-alanine, Scientific Reports 9 (2019) 11754.

[11] J. Bié, B. Sepodes, P. C. B. Fernandes, M. H. L. Ribeiro: Enzyme Immobilization and Co-Immobilization: Main Framework, Advances and Some Applications, Processes 10 (2022).

[12] K. Xu, X. Chen, R. Zheng, Y. Zheng: Immobilization of Multi-Enzymes on Support Materials for Efficient Biocatalysis, Frontiers in Bioengineering and Biotechnology 8 (2020).

[13] Q. Ji, B. Wang, J. Tan, L. Zhu, L. Li: Immobilized multienzymatic systems for catalysis of cascade reactions, Process Biochemistry 51 (2016) 1193–1203.

[14] C. Di Spiridione, M. Aresta, A. Dibenedetto: Improving the Enzymatic Cascade of Reactions for the Reduction of CO2 to CH3OH in Water: From Enzymes Immobilization Strategies to Cofactor Regeneration and Cofactor Suppression, Molecules 27 (2022).

[15] E. T. Hwang, S. Lee: Multienzymatic Cascade Reactions via Enzyme Complex by Immobilization, ACS Catalysis 9 (2019) 4402–4425.

[16] J. M. Bolivar, J. M. Woodley, R. Fernandez-Lafuente: Is enzyme immobilization a mature discipline? Some critical considerations to capitalize on the benefits of immobilization, Chem. Soc. Rev. 51 (2022) 6251–6290. Publisher: The Royal Society of Chemistry.

[17] D. Brady, J. Jordaan: Advances in enzyme immobilisation, Biotechnology Letters 31 (2009) 1639.

[18] R. Fernandez-Lafuente: Stabilization of multimeric enzymes: Strategies to prevent subunit dissociation, Enzyme and Microbial Technology 45 (2009) 405–418.

[19] C. Garcia-Galan, A. Berenguer-Murcia, R. Fernandez-Lafuente, R. C. Rodrigues: Potential of Different Enzyme Immobilization Strategies to Improve Enzyme Performance, Advanced Synthesis & Catalysis 353 (2011) 2885–2904.

[20] K. Hernandez, R. Fernandez-Lafuente: Control of protein immobilization: Coupling immobilization and site-directed mutagenesis to improve biocatalyst or biosensor performance, Enzyme and Microbial Technology 48 (2011) 107–122.

[21] P. V. Iyer, L. Ananthanarayan: Enzyme stability and stabilization-Aqueous and non-aqueous environment, Process Biochemistry 43 (2008) 1019–1032.

[22] D.-M. Liu, C. Dong: Recent advances in nano-carrier immobilized enzymes and their applications, Process Biochemistry 92 (2020) 464–475.

[23] R. A. Sheldon: Enzyme Immobilization: The Quest for Optimum Performance, Advanced Synthesis & Catalysis 349 (2007) 1289–1307.

[24] R. A. Sheldon, S. van Pelt: Enzyme immobilisation in biocatalysis: why, what and how, Chem. Soc. Rev. 42 (2013) 6223–6235. Publisher: The Royal Society of Chemistry.

[25] C. Mateo, V. Grazu, J. M. Palomo, F. Lopez-Gallego, R. Fernandez-Lafuente, J. M. Guisan: Immobilization of enzymes on heterofunctional epoxy supports, Nature Protocols 2 (2007) 1022–1033.

[26] R. C. Rodrigues, C. Ortiz, A. Berenguer-Murcia, R. Torres, R. Fernández-Lafuente: Modifying enzyme activity and selectivity by immobilization, Chem. Soc. Rev. 42 (2013) 6290–6307. Publisher: The Royal Society of Chemistry.

[27] T. Bayer, S. Milker, T. Wiesinger, F. Rudroff, M. D. Mihovilovic: Designer Microorganisms for Optimized Redox Cascade Reactions - Challenges and Future Perspectives, Advanced Synthesis & Catalysis 357 (2015) 1587–1618.

[28] U. M. Kahar, K.-G. Chan, M. H. Sani, N. I. M. Noh, K. M. Goh: Effects of single and co-immobilization on the product specificity of type I pullulanase from Anoxybacillus sp. SK3-4, International Journal of Biological Macromolecules 104 (2017) 322–332.

[29] M. Ladero, A. Santos, F. Garcia-Ochoa: Diffusion and chemical reaction rates with nonuniform enzyme distribution: An experimental approach, Biotechnology and Bioengineering 72 (2001) 458–467.

[30] J. Rocha-Martin, B. d. l. Rivas, R. Munoz, J. M. Guisan, F. Lopez-Gallego: Rational Co-Immobilization of Bi-Enzyme Cascades on Porous Supports and their Applications in Bio-Redox Reactions with In Situ Recycling of Soluble Cofactors, ChemCatChem 4 (2012) 1279–1288.

[31] P. Garcia-Garcia, J. Rocha-Martin, G. Fernandez-Lorente, J. M. Guisan: Colocalization of oxidase and catalase inside a porous support to improve the elimination of hydrogen peroxide: Oxidation of biogenic amines by amino oxidase from Pisum sativum, Enzyme and Microbial Technology 115 (2018) 73–80.

[32] J. M. Bolivar, A. Hidalgo, L. SAnchez-Ruiloba, J. Berenguer, J. M. Guisan, F. Lopez-Gallego: Modulation of the distribution of small proteins within porous matrixes by smart-control of the immobilization rate, Journal of Biotechnology 155 (2011) 412–420.

[33] R. Siedentop, C. Claassen, D. Rother, S. Lütz, K. Rosenthal: Getting the Most Out of Enzyme Cascades: Strategies to Optimize In Vitro Multi-Enzymatic Reactions, Catalysts 11 (2021).

[34] S. Arana-Peña, D. Carballares, R. Morellon-Sterlling, A. Berenguer-Murcia, A. R. Alcántara, R. C. Rodrigues, R. Fernandez-Lafuente: Enzyme co-immobilization: Always the biocatalyst designers' choice...or not?, Biotechnology Advances 51 (2021) 107584.

[35] J. D. Bloom, M. M. Meyer, P. Meinhold, C. R. Otey, D. MacMillan, F. H. Arnold: Evolving strategies for enzyme engineering, Membranes/Engineering and design 15 (2005) 447–452.

[36] T. A. S. M. Anshula Sharma, Gaganjot Gupta, B. Kaur: Enzyme Engineering: Current Trends and Future Perspectives, Food Reviews International 37 (2021). Publisher: Taylor & Francis pages = 121–154,.

[37] I. Victorino da Silva Amatto, N. Gonsales da Rosa-Garzon, F. Antonio de Oliveira Simoes, F. Santiago, N. Pereira da Silva Leite, J. Raspante Martins, H. Cabral: Enzyme engineering and its industrial applications, Biotechnology and Applied Biochemistry 69 (2022) 389–409.

[38] J. A. McIntosh, A. E. Owens: Enzyme engineering for biosynthetic cascades, Current Opinion in Green and Sustainable Chemistry 29 (2021) 100448.

[39] J. Nazor, J. Liu, G. Huisman: Enzyme evolution for industrial biocatalytic cascades, Chemical Biotechnology Pharmaceutical Biotechnology 69 (2021) 182–190.

[40] A. I. Benitez-Mateos, D. Roura Padrosa, F. Paradisi: Multistep enzyme cascades as a route towards green and sustainable pharmaceutical syntheses, Nature Chemistry 14 (2022) 489–499.

[41] O. Melse, S. Sutiono, M. Haslbeck, G. Schenk, I. Antes, V. Sieber: Structure-Guided Modulation of the Catalytic Properties of [2Fe-2S]-Dependent Dehydratases, ChemBioChem 23 (2022) e202200088.

[42] J. F. Kornecki, A. Pick, P. Dominguez de María, F. Lopez-Gallego: Heterogeneous biocatalytic reduction of 5-(hydroxy)methyl furfural using two co-immobilised alcohol dehydrogenases, RSC Sustain. 1 (2023) 1883–1895. Publisher: RSC.

[43] R. M. Daniel, J. L. Finney, M. Stoneham, C. Nick Pace, S. Treviño, E. Prabhakaran, J. Martin Scholtz: Protein structure, stability and solubility in water and other solvents, Philosophical Transactions of the Royal Society of London. Series B: Biological Sciences 359 (2004) 1225–1235.

[44] M. Cox, D. L. Nelson: Principles of Biochemistry, 8th edition ed., Macmillan Learning, 2021.

[45] X. Wang, T. Saba, H. H. Yiu, R. F. Howe, J. A. Anderson, J. Shi: Cofactor nad(p)h regeneration inspired by heterogeneous pathways, Chem 2 (2017) 621–654.

[46] L. F. Sotoft, B.-G. Rong, K. V. Christensen, B. Norddahl: Process simulation and economical evaluation of enzymatic biodiesel production plant, Bioresource Technology 101 (2010) 5266–5274.

[47] Q. M. Dudley, A. S. Karim, M. C. Jewett: Cell-free metabolic engineering: Biomanufacturing beyond the cell, Biotechnology Journal 10 (2015) 69–82.

[48] S. Kara, F. Rudroff: Enzyme Cascade Design and Modelling, Springer Nature, 2021.

[49] J. J. Lischeske, J. J. Stickel: A two-phase substrate model for enzymatic hydrolysis of lignocellulose: application to batch and continuous reactors, Biotechnology for Biofuels 12 (2019) 299.

[50] W. Finnigan, R. Cutlan, R. Snajdrova, J. P. Adams, J. A. Littlechild, N. J. Harmer: Engineering a Seven Enzyme Biotransformation using Mathematical Modelling and Characterized Enzyme Parts, ChemCatChem 11 (2019) 3474–3489.

[51] J. Johannsen, F. Meyer, C. Engelmann, A. Liese, G. Fieg, P. Bubenheim, T. Waluga: Multi-enzyme cascade reaction in a miniplant two-phase-system: Model validation and mathematical optimization, AIChE Journal 67 (2021) e17158.

[52] R. Siedentop, M. Siska, N. Moeller, H. Lanzrath, E. von Lieres, S. Luetz, K. Rosenthal: Bayesian Optimization for an ATP-Regenerating In Vitro Enzyme Cascade, Catalysts 13 (2023).

[53] R. Siedentop, M. Dziennus, S. Lütz, K. Rosenthal: Debottlenecking of an In Vitro Enzyme Cascade Using a Combined Model- and Experiment-Based Approach, Chemie Ingenieur Technik 95 (2023) 543–548.

[54] C. Hold, S. Billerbeck, S. Panke: Forward design of a complex enzyme cascade reaction, Nature Communications 7 (2016) 12971.

[55] S. Gargiulo, D. J. Opperman, U. Hanefeld, I. W. C. E. Arends, F. Hollmann: A biocatalytic redox isomerisation, Chem. Commun. 48 (2012) 6630–6632. Publisher: The Royal Society of Chemistry.

[56] S. Sutiono, I. Zachos, L. Paschalidis, A. Pick, J. Burger, V. Sieber: Biocatalytic Production of 1,2,4-Butanetriol beyond a Titer of 100 g/L: Boosting by Intermediates, ACS Sustainable Chemistry & Engineering 11 (2023).

[57] Y.-H. P. Zhang: Production of biocommodities and bioelectricity by cell-free synthetic enzymatic pathway biotransformations: Challenges and opportunities, Biotechnology and Bioengineering 105 (2010) 663–677.

[58] V. Köhler, N. J. Turner: Artificial concurrent catalytic processes involving enzymes, Chemical Communications 51 (2015) 450–464.

[59] J. Muschiol, C. Peters, N. Oberleitner, M. D. Mihovilovic, U. T. Bornscheuer, F. Rudroff: Cascade catalysis - strategies and challenges en route to preparative synthetic biology, Chemical Communications 51 (2015) 5798–5811.

[60] C. Schmidt-Dannert, F. Lopez-Gallego: A roadmap for biocatalysis - functional and spatial orchestration of enzyme cascades, Microbial Biotechnology 9 (2016) 601–609.

[61] S. P. France, L. J. Hepworth, N. J. Turner, S. L. Flitsch: Constructing Biocatalytic Cascades: In Vitro and in Vivo Approaches to de Novo Multi-Enzyme Pathways, ACS Catalysis 7 (2017) 710–724.

[62] C. T. Walsh, B. S. Moore: Enzymatic Cascade Reactions in Biosynthesis, Angewandte Chemie International Edition 58 (2019) 6846–6879.

[63] S. Wu, R. Snajdrova, J. C. Moore, K. Baldenius, U. T. Bornscheuer: Biocatalysis: Enzymatic Synthesis for Industrial Applications, Angewandte Chemie International Edition 60 (2021) 88–119.

[64] M. Bortz, J. Burger, N. Asprion, S. Blagov, R. Böttcher, U. Nowak, A. Scheithauer, R. Welke, K.-H. Kuefer, H. Hasse: Multi-criteria optimization in chemical process design and decision support by navigation on Pareto sets, Computers & Chemical Engineering 60 (2014) 354–363.

[65] J. Burger, N. Asprion, S. Blagov, R. Boettcher, U. Nowak, M. Bortz, R. Welke, K.-H. Kuefer, H. Hasse: Multi-Objective Optimization and Decision Support in Process Engineering - Implementation and Application, Chemie Ingenieur Technik 86 (2014) 1065–1072.

[66] R. Marler, J. Arora: Survey of multi-objective optimization methods for engineering, Structural and Multidisciplinary Optimization 26 (2004) 369–395.

[67] N. Asprion, S. Blagov, O. Ryll, R. Welke, A. Winterfeld, A. Dittel, M. Bortz, K.-H. Küfer, J. Burger, A. Scheithauer, H. Hasse: Pareto-Navigation in Chemical Engineering, in: E. Pistikopoulos, M. Georgiadis, A. Kokossis (Eds.), Computer Aided Chemical Engineering, volume 29, Elsevier, 2011, pp. 422–426.

[68] P. Nimmegeers, M. Vallerio, D. Telen, J. Van Impe, F. Logist: Interactive Multi-objective Dynamic Optimization of Bioreactors under Parametric Uncertainty, Chemie Ingenieur Technik 91 (2019) 349–362.

[69] F. C. Lee, G. P. Rangaiah, A. K. Ray: Multi-objective optimization of an industrial penicillin V bioreactor train using non-dominated sorting genetic algorithm, Biotechnology and Bioengineering 98 (2007) 586–598.

[70] D. Sarkar, J. M. Modak: Pareto-optimal solutions for multi-objective optimization of fed-batch bioreactors using nondominated sorting genetic algorithm, Chemical Engineering Science 60 (2005) 481–492.

[71] K. Flevaris, C. Chatzidoukas: Optimal fed-batch bioreactor operating strategies for the microbial production of lignocellulosic bioethanol and exploration of their economic implications: A step forward towards sustainability and commercialization, Journal of Cleaner Production 295 (2021) 126384.

[72] S. Sutiono, A. Pick, V. Sieber: Converging conversion - using promiscuous biocatalysts for the cell-free synthesis of chemicals from heterogeneous biomass, Green Chem. 23 (2021) 3656–3663. Publisher: The Royal Society of Chemistry.

[73] M. Dias Gomes, B. R. Bommarius, S. R. Anderson, B. D. Feske, J. M. Woodley, A. S. Bommarius: Bubble Column Enables Higher Reaction Rate for Deracemiza-

tion of (R,S)-1-Phenylethanol with Coupled Alcohol Dehydrogenase/NADH Oxidase System, Advanced Synthesis & Catalysis 361 (2019) 2574–2581.

[74] S. R. Anderson, B. R. Bommarius, J. M. Woodley, A. S. Bommarius: Sparged but not stirred: Rapid, ADH-NADH oxidase catalyzed deracemization of alcohols in a bubble column, Chemical Engineering Journal 417 (2021) 127909.

[75] D. L. Purich: Chapter 5 - Initial-Rate Kinetics of One-Substrate Enzyme-Catalyzed Reactions, in: D. L. Purich (Ed.), Enzyme Kinetics: Catalysis & Control, Elsevier, Boston, 2010, pp. 287–334.

[76] D. L. Purich: Chapter 6 - Initial-Rate Kinetics of Multi-Substrate Enzyme-Catalyzed Reactions, in: D. L. Purich (Ed.), Enzyme Kinetics: Catalysis & Control, Elsevier, Boston, 2010, pp. 335–378.

[77] M. Sudar, Z. Findrik, M. V. Domanovac, D. Vasic-Racki: Coenzyme regeneration catalyzed by NADH oxidase from Lactococcus lactis, Biochemical Engineering Journal 88 (2014) 12–18.

[78] P. M. Doran: Chapter 10 - Mass Transfer, in: P. M. Doran (Ed.), Bioprocess Engineering Principles (Second Edition), Academic Press, London, 2013, pp. 379–444.

[79] M. L. Bynum, G. A. Hackebeil, W. E. Hart, C. D. Laird, B. L. Nicholson, J. D. Siirola, J.-P. Watson, D. L. Woodruff: Pyomo–optimization modeling in python, volume 67, third ed., Springer Science & Business Media, 2021.

[80] W. E. Hart, J.-P. Watson, D. L. Woodruff: Pyomo: modeling and solving mathematical programs in Python, Mathematical Programming Computation 3 (2011) 219.

[81] B. Nicholson, J. D. Siirola, J.-P. Watson, V. M. Zavala, L. T. Biegler: pyomo.dae: a modeling and automatic discretization framework for optimization with differential and algebraic equations, Mathematical Programming Computation 10 (2018) 187–223.

[82] A. Rasmuson, B. Andersson, L. Olsson, R. Andersson: Mathematical Modeling in Chemical Engineering, Cambridge University Press, Cambridge, 2014.

[83] A. Waechter, L. T. Biegler: On the implementation of an interior-point filter line-search algorithm for large-scale nonlinear programming, Mathematical Programming 106 (2006) 25–57.

[84] M. Bortz, J. Burger, E. von Harbou, M. Klein, J. Schwientek, N. Asprion, R. Boettcher, K.-H. Kuefer, H. Hasse: Efficient Approach for Calculating Pareto Boundaries under Uncertainties in Chemical Process Design, Industrial & Engineering Chemistry Research 56 (2017) 12672–12681. Publisher: American Chemical Society.

[85] N. Oberleitner, C. Peters, J. Muschiol, M. Kadow, S. Sass, T. Bayer, P. Schaaf, N. Iqbal, F. Rudroff, M. D. Mihovilovic, U. T. Bornscheuer: An Enzymatic Toolbox for Cascade Reactions: A Showcase for an In Vivo Redox Sequence in Asymmetric Synthesis, ChemCatChem 5 (2013) 3524–3528.

[86] N. Oberleitner, C. Peters, F. Rudroff, U. T. Bornscheuer, M. D. Mihovilovic: In vitro characterization of an enzymatic redox cascade composed of an alcohol dehydrogenase, an enoate reductases and a Baeyer-Villiger monooxygenase, Journal of Biotechnology 192 (2014) 393–399.

[87] F. G. Mutti, T. Knaus, N. S. Scrutton, M. Breuer, N. J. Turner: Conversion of alcohols to enantiopure amines through dual-enzyme hydrogen-borrowing cascades, Science 349 (2015) 1525–1529.

[88] S. Milker, M. J. Fink, N. Oberleitner, A. K. Ressmann, U. T. Bornscheuer, M. D. Mihovilovic, F. Rudroff: Kinetic Modeling of an Enzymatic Redox Cascade In Vivo Reveals Bottlenecks Caused by Cofactors, ChemCatChem 9 (2017) 3420–3427.

[89] B. Begander, A. Huber, J. Sperl, V. Sieber: Development of a Cofactor Balanced, Multi Enzymatic Cascade Reaction for the Simultaneous Production of L-Alanine and L-Serine from 2-Keto-3-deoxy-gluconate, Catalysts 11 (2021).

[90] L. Paschalidis, B. Beer, S. Sutiono, V. Sieber, J. Burger: Design of enzymatic cascade reactors through multi-objective dynamic optimization, Biochemical Engineering Journal 181 (2022) 108384.

[91] L. Paschalidis, S. Arana-Peña, V. Sieber, J. Burger: Mechanistic modeling, parametric study, and optimization of immobilization of enzymatic cascades in porous particles, React. Chem. Eng. 8 (2023) 2234–2244. Publisher: The Royal Society of Chemistry.

[92] S. Velasco-Lozano, A. I. Benitez-Mateos, F. Lopez-Gallego: Co-immobilized phosphorylated cofactors and enzymes as self-sufficient heterogeneous biocatalysts for chemical processes, Angewandte Chemie International Edition 56 (2017) 771–775.

[93] M. Zheng, S. Zhang, G. Ma, P. Wang: Effect of molecular mobility on coupled enzymatic reactions involving cofactor regeneration using nanoparticle-attached enzymes, Journal of Biotechnology 154 (2011) 274–280.

[94] E. Diamanti, S. Arana-Peña, P. Ramos-Cabrer, N. Comino, D. Carballares, R. Fernandez-Lafuente, F. Lopez-Gallego: Intraparticle Macromolecular Migration Alters the Structure and Function of Proteins Reversibly Immobilized on Porous Microbeads, Advanced Materials Interfaces 9 (2022) 2200263.

[95] E. W. Thiele: Relation between Catalytic Activity and Size of Particle, Industrial & Engineering Chemistry 31 (1939) 916–920. Publisher: American Chemical Society.

[96] C. G. Vayenas, S. Pavlou: Optimal catalyst distribution for selectivity maximization in pellets: Parallel and consecutive reactions, Chemical Engineering Science 42 (1987) 1655–1666.

[97] F. Shadman-Yazdi, E. E. Petersen: Changing catalyst performance by varying the distribution of active catalyst within porous supports, Chemical Engineering Science 27 (1972) 227–237.

[98] D. R. Rutkin, E. E. Petersen: The effect on selectivity of the macroscopic distribution of the components in a dual function catalyst, Chemical Engineering Science 34 (1979) 109–116.

[99] O. Levenspiel: Chemical Reaction Engineering, Wiley, 1999.

[100] T. J. Mays: A new classification of pore sizes, in: P. L. Llewellyn, F. Rodriquez-Reinoso, J. Rouqerol, N. Seaton (Eds.), Characterization of Porous Solids VII, volume 160 of *Studies in Surface Science and Catalysis*, Elsevier, 2007, pp. 57–62.

[101] M. Vert, Y. Doi, K.-H. Hellwich, M. Hess, P. Hodge, P. Kubisa, M. Rinaudo, F. Schué: Terminology for biorelated polymers and applications (IUPAC Recommendations 2012), Pure and Applied Chemistry 84 (2012) 377–410.

[102] P. Doran: Bioprocess Engineering Principles, Engineering professional collection, Elsevier Science, 2012.

A Appendix: Model-based optimization of dynamic processes with dissolved enzymes

A.1 Reaction model fits

The reaction models were fitted to experimental data from Beer et al. [8]. Comparisons of the reaction models and the experimental data are presented in Figures 29-35.

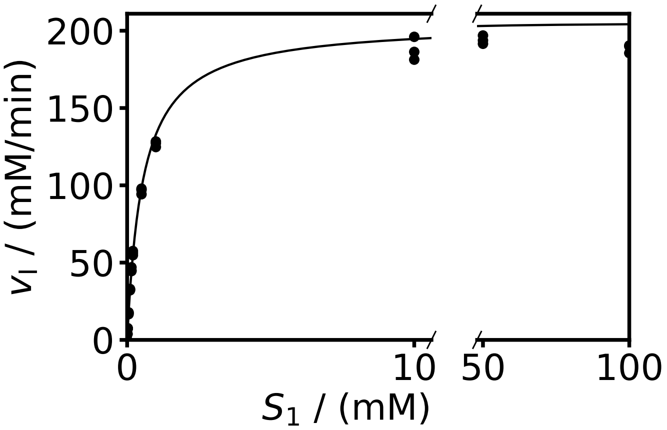

Figure 29: The reaction rate of the reaction catalyzed by UDH for different D-glucuronate concentrations, with a constant concentration of NAD$^+$ of 1 mM. — Model, • Experiment.

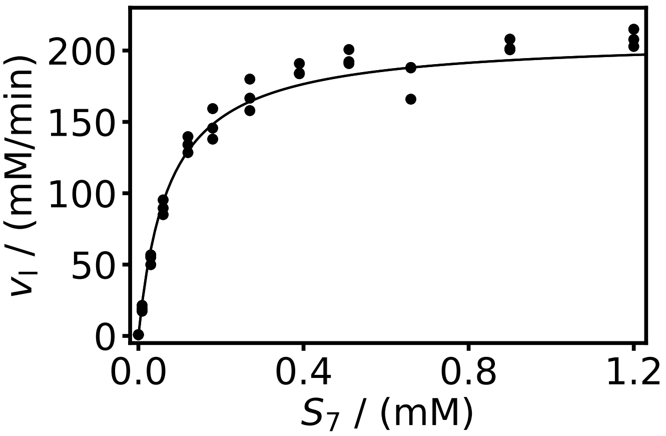

Figure 30: The reaction rate of the reaction catalyzed by UDH for different NAD$^+$ concentrations, with a constant concentration of D-glucuronate of 10 mM. — Model, • Experiment.

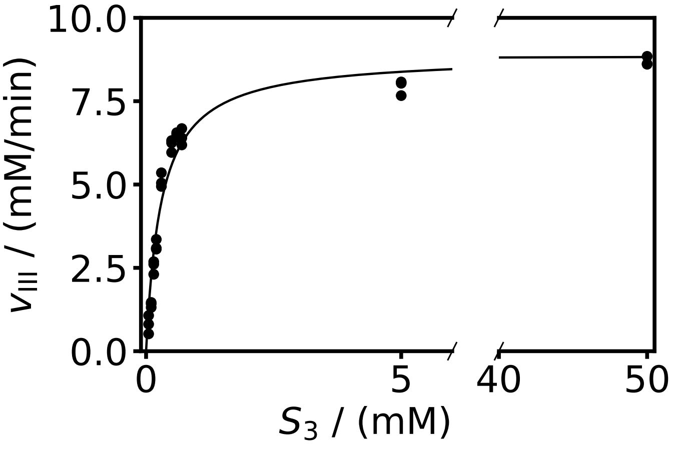

Figure 31: The reaction rate of the reaction catalyzed by GlucD for different D-glucarate concentrations. — Model, • Experiment.

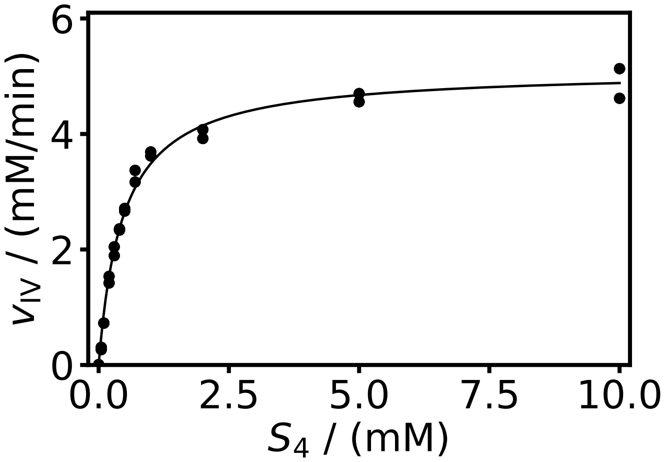

Figure 32: The reaction rate of the reaction catalyzed by KdgD for different 5-keto-4-deoxy-glucarate concentrations. — Model, • Experiment.

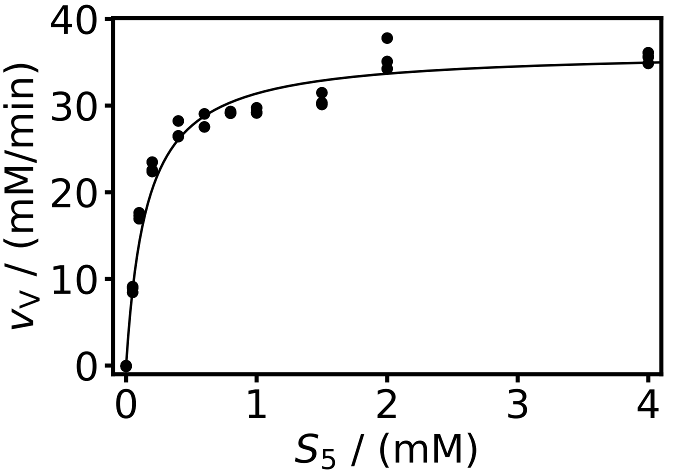

Figure 33: The reaction rate of the reaction catalyzed by KgsalDH for different α-ketoglutarate semialdehyde concentrations, with a constant concentration of NAD$^+$ of 4 mM. — Model, • Experiment.

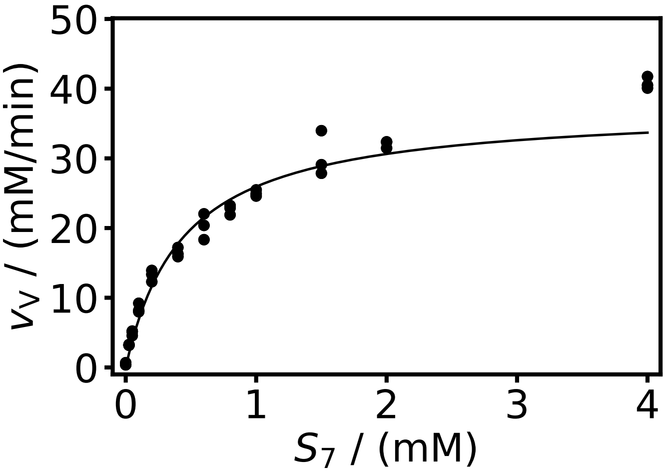

Figure 34: The reaction rate of the reaction catalyzed by KgsalDH for different NAD$^+$ concentrations, with a constant concentration of α-ketoglutarate semialdehyde of 2 mM. — Model, • Experiment.

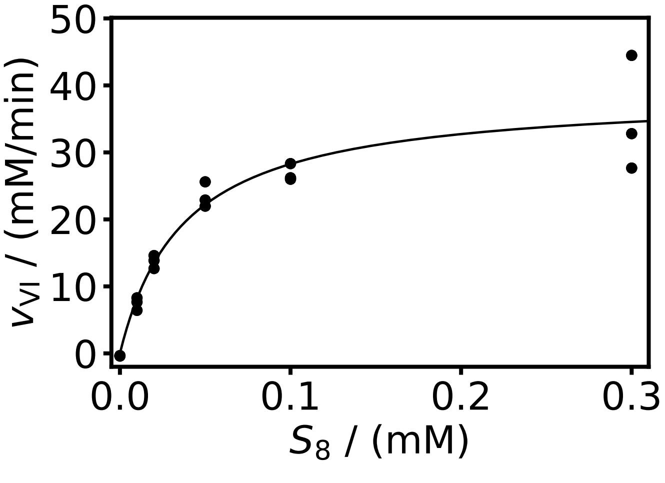

Figure 35: The reaction rate of the reaction catalyzed by NOX (used by Beer et al. [8]) for different NADH concentrations. — Model, • Experiment.

A.2 NOX deactivation fit

The deactivation of the NOX used by Beer et al. in a bubble reactor is presented in Figure 36 .

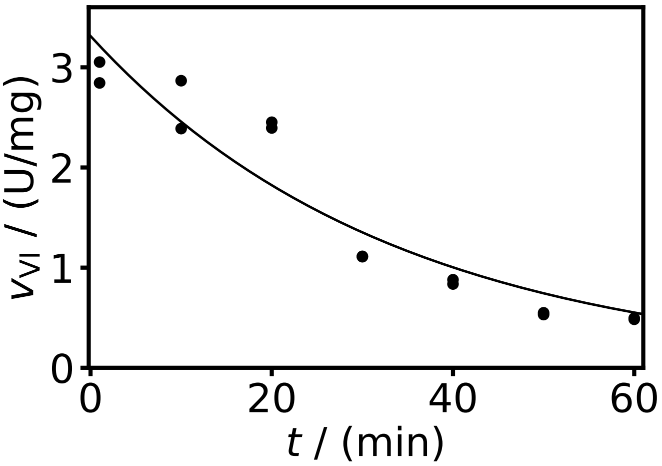

Figure 36: The deactivation of NOX used by Beer et al. [8] in a bubble reactor. — Model, • Experiment.

A.3 Data reconciliation

The data for the cascade experiment conducted by Beer et al. [8] (Figure 5B in Beer et al. [8]) are presented in Table 4. $X_{i,t}$ are the measured molar concentrations for substrate i and time point t.

Table 4: The original cascade experiment data.

t /(min)	$X_{1,t}$ /(mM)	$X_{2,t}+X_{3,t}$ /(mM)	$X_{4,t}$ /(mM)	$X_{5,t}$ /(mM)	$X_{6,t}$ /(mM)	$X_{7,t}$ /(mM)
0	49.95	0.89	0.00	0.00	0.10	4.42
10	31.13	15.33	0.00	0.00	1.23	0.94
20	10.97	21.94	0.00	0.00	3.91	1.20
30	2.03	27.15	0.00	0.00	7.14	4.59
40	0.00	24.93	0.00	5.82	11.03	4.58
50	0.00	24.33	0.00	0.00	16.09	4.57
60	0.00	22.46	0.00	0.00	18.75	4.43
70	0.00	20.65	0.00	0.00	21.33	4.31
80	0.00	18.76	0.00	0.00	24.40	4.34
90	0.00	16.81	0.00	2.07	26.61	4.46
120	0.00	15.26	0.00	0.00	32.72	4.40
300	0.00	5.73	0.00	0.00	45.97	4.26

The sum of the measured molar concentrations of substrates 1-6, λ_t, is calculated as shown in Equation (133).

$$\lambda_t = \sum_{i=1}^{6} X_{i,t} \tag{133}$$

The relative errors, $\epsilon_i^{\mathrm{rel}}$ for each substrate measurement are shown in Table 5.

Table 5: The relative errors of the HPLC instrument for each substrate.

i	$\epsilon_i^{\mathrm{rel}}$ /(mM/mM)
1	0.01
2	0.02
3	0.02
4	0.10
5	0.10
6	0.02

The absolute errors, $\epsilon_{i,t}^{\mathrm{abs}}$, are calculated for each measurement from the relative errors of the HPLC instrument as shown in Equation (134).

$$\epsilon_{i,t}^{\mathrm{abs}} = \epsilon_{i,t}^{\mathrm{rel}} \cdot X_{i,t} \tag{134}$$

The HPLC instrument has a detection limit for the measured substrates. When $X_{i,t}$ = 0 mM, it is not clear whether the measured value is indeed 0 or if there is a small amount of the chemical that goes undetected. Therefore, for all measurements, with λ_t ≤ 50.00 mM and with $X_{i,t}$ = 0 mM, the corresponding detection limit is added to the absolute error. The detection limits for S_1 is 0.50 mM while the detection limit for S_4 and S_5 is 2 mM. The resulting absolute errors are presented in Table 6.

Table 6: The absolute errors of the HPLC measurments.

t /(min)	$\epsilon^{\text{abs}}_{1,t}$ /(mM)	$\epsilon^{\text{abs}}_{2,t}+\epsilon^{\text{abs}}_{3,t}$ /(mM)	$\epsilon^{\text{abs}}_{4,t}$ /(mM)	$\epsilon^{\text{abs}}_{5,t}$ /(mM)	$\epsilon^{\text{abs}}_{6,t}$ /(mM)
0	0.50	0.02	0.00	0.00	0.00
10	0.31	0.31	2.00	2.00	0.02
20	0.11	0.44	2.00	2.00	0.08
30	0.02	0.54	2.00	2.00	0.14
40	0.50	0.50	2.00	0.58	0.22
50	0.50	0.49	2.00	2.00	0.32
60	0.50	0.45	2.00	2.00	0.38
70	0.50	0.41	2.00	2.00	0.43
80	0.50	0.38	2.00	2.00	0.49
90	0.50	0.34	2.00	0.21	0.53
120	0.50	0.31	2.00	2.00	0.65
300	0.00	0.11	0.00	0.00	0.92

The sum of all absolute errors for each time point is calculated as shown in Equation (135).

$$\psi_t = \sum_{i=1}^{6} \epsilon^{abs}_{i,t} \tag{135}$$

Since the stoichiometry of all reactions is 1:1, λ_t should remain constant and equal to 50.00 mM during the experiment. However, as shown in Figure 37, this is not the case.

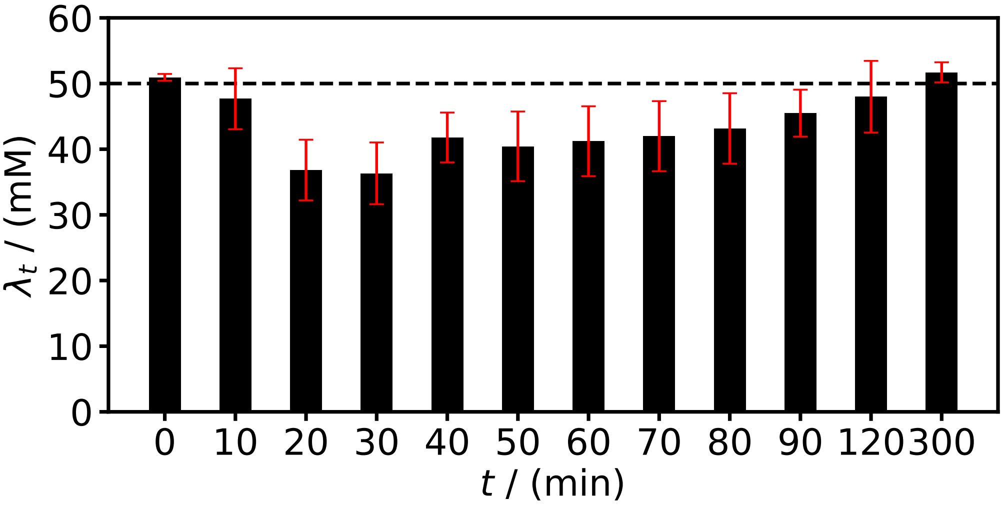

Figure 37: Comparison of λ_t with the theoretical concentration of 50.00 mM. The red error lines show ψ_t.

A factor $f_{i,t}$, is calculated from the absolute errors as shown in Equation (136).

$$f_{i,t} = \frac{\epsilon^{\text{abs}}_{i,t}}{\psi_t} \tag{136}$$

Finally, all data were reconciled as shown in Equation (137):

$$X^{rec}_{i,t} = X_{i,t} + f_{i,t} \cdot (50\,\text{mM} - \lambda_t) \tag{137}$$

The reconciled data are presented in Table 7. The sums of the reconciled data for substrates 1-6 remain constant and equal to 50.00 mM during the experiment.

Table 7: The reconciled cascade experiment data.

t /(min)	$X^{rec}_{1,t}$ /(mM)	$X^{rec}_{2,t}+X^{rec}_{3,t}$ /(mM)	$X^{rec}_{4,t}$ /(mM)	$X^{rec}_{5,t}$ /(mM)	$X^{rec}_{6,t}$ /(mM)	$X^{rec}_{7,t}$ /(mM)
0	49.04	0.86	0.00	0.00	0.10	4.42
10	31.28	15.48	1.00	1.00	1.24	0.94
20	11.29	23.19	5.70	5.70	4.13	1.20
30	2.09	28.73	5.82	5.82	7.56	4.59
40	1.08	26.00	4.32	7.08	11.51	4.58
50	0.90	25.21	3.61	3.61	16.67	4.57
60	0.83	23.20	3.30	3.30	19.37	4.43
70	0.75	21.28	3.00	3.00	21.97	4.31
80	0.64	19.24	2.55	2.55	25.02	4.34
90	0.63	17.24	2.52	2.33	27.28	4.46
120	0.18	15.37	0.74	0.74	32.97	4.40
300	0.00	5.54	0.00	0.00	44.46	4.26

A.4 Sensitivity analysis

A sensitivity analysis was conducted to study the uncertainty of the output of the developed mathematical model. Two cases were defined. In the first case, the values for the V^j_{max} and k_{II} were selected to be on the lower bound of their 95% confidence interval, while the values of K^j_i and k^{NOX} were selected to be on the corresponding upper bounds. In the second case the parameter values were selected on the opposite bounds. This way a worst and best case scenario are defined. The process schedules A, B, C, D, and E from Figures 4 and 5 of the main part of the dissertation were simulated again, but this time with the parameters of cases one and two. The resulting space-time yields are presented in Table 8.

Table 8: Results of the sensitivity analysis.

Process schedule	$\Phi^{\mathrm{STY,\,Case\,1}}$ / (mM/min)	Φ^{STY} / (mM/min)	$\Phi^{\mathrm{STY,\,Case\,2}}$ / (mM/min)
A	0.047	0.161	0.164
B	0.126	0.287	0.289
C	0.609	2.351	2.403
D	0.926	2.789	2.802
E	1.186	2.837	2.844

As shown in Table 8, the space-time yield decreases significantly when using the parameter values of case one. A very small improvement is achieved to the already calculated space-time yields when using the values of case two.

A.5 Solutions C and D

As shown in Figures 38 and 39 the optimizer uses two different strategies in solutions C and D. In solution C, α-ketoglutarate starts being produced right from the beginning of the batch process. In solution D, α-ketoglutarate starts accumulating only after all of the D-glucuronate has been consumed. In both cases, the optimizer finds the optimal profiles for the substrate concentrations to ensure that the enzyme concentrations are used in the most productive way.

A.6 Optimization results

In this section the results for each Pareto-optimal process schedule are presented. Eight tables are presented in total and they correspond to the eight different Pareto solution sets. Tables 9-12 correspond to the results presented in Figure 4a) of the main article. Tables 13-16 correspond to the results presented in Figure 5a) of the main article. In these tables the values of the objectives and control variables are included.

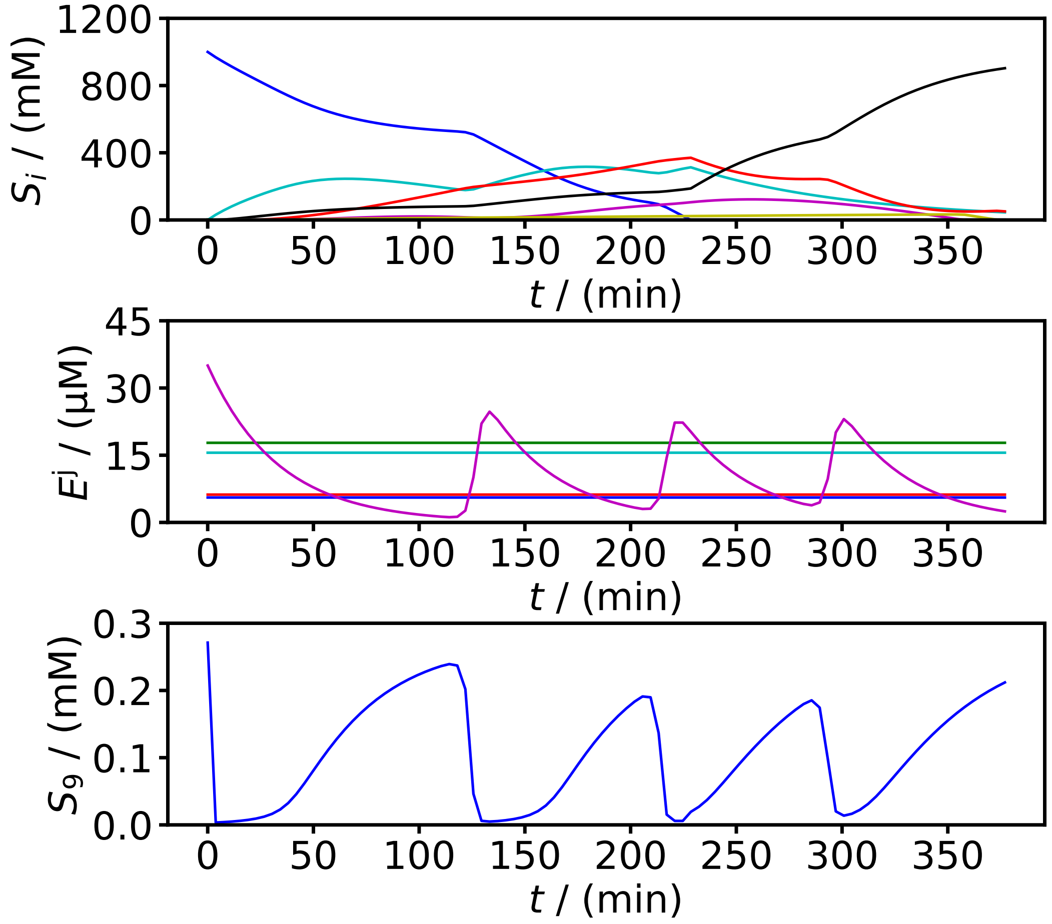

Figure 38: Time profiles for $\Phi^{\mathrm{EC}} = 0.4\ \mu\mathrm{M/min}$ and $\Phi^{\mathrm{CC}} = 0.005\ \mathrm{mM/min}$ and for the Sudar et al. [77] cofactor regeneration system with $k_{\mathrm{L}}a = 15\ \mathrm{min}^{-1}$. First plot: The substrate concentration profiles, — D-glucuronate, — glucaro-1,4-lactone, — D-glucarate, — 5-keto-4-deoxy-glucarate, — α-ketoglutarate semialdehyde, — α-ketoglutarate, — NAD⁺, — NADH. Second plot: The enzyme concentration profiles, — UDH, — GlucD, — KdgD, — KgsalDH, — NOX. Third plot: The oxygen concentration profile.

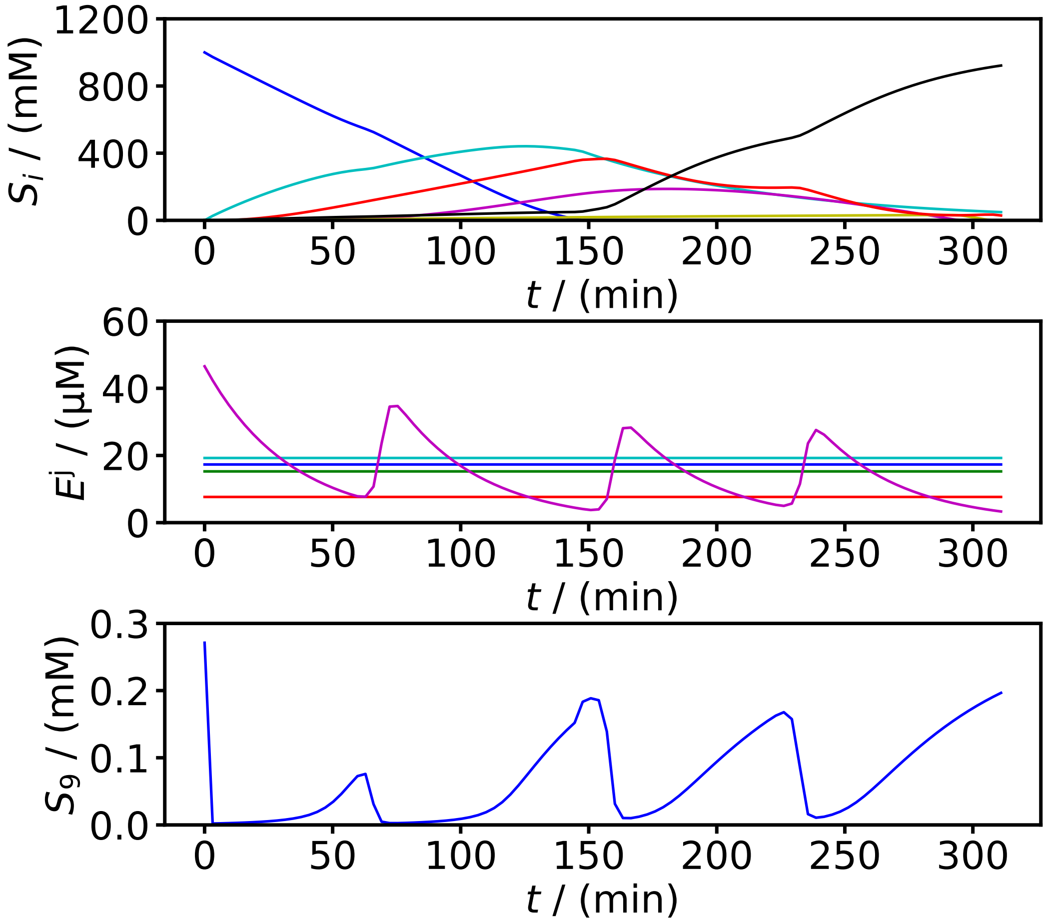

Figure 39: Time profiles for $\Phi^{\mathrm{EC}} = 0.6\ \mu\mathrm{M/min}$ and $\Phi^{\mathrm{CC}} = 0.005\ \mathrm{mM/min}$ and for the Sudar et al. [77] cofactor regeneration system with $k_{\mathrm{L}}a = 15\ \mathrm{min}^{-1}$. First plot: The substrate concentration profiles, — D-glucuronate, — glucaro-1,4-lactone, — D-glucarate, — 5-keto-4-deoxy-glucarate, — α-ketoglutarate semialdehyde, — α-ketoglutarate, — NAD$^+$, — NADH. Second plot: The enzyme concentration profiles, — UDH, — GlucD, — KdgD, — KgsalDH, — NOX. Third plot: The oxygen concentration profile.

Table 9: The optimization results for the $k_\mathrm{L}a = 1.2\ \mathrm{min}^{-1}$ case, $\epsilon^{\mathrm{CC}} = 0.005$ mM/min for the Sudar et al. [77] cofactor regeneration system.

Φ^{STY} /(mM/min)	Φ^{EC} /(μM/min)	Φ^{CC} /(mM/min)	t_f /(min)	$S_i(0)$ /(mM)		$E^j(0)$ /(μM)					A_k /(mM/min)			t_k /(min)		
				1	7	UDH	GlucD	KdgD	KgsalDH	NOX	1	2	3	1	2	3
0.000	0.000	0.005	49,999	1	234	0.00	0.00	0.00	0.00	0.00	0	0	0	733	17,271	34,645
0.161	0.025	0.005	479	84	3	0.35	0.47	1.15	1.45	2.69	29	25	29	188	285	376
0.238	0.050	0.005	357	97	2	0.68	0.73	1.79	1.84	4.39	43	39	42	110	196	271
0.272	0.075	0.005	360	111	2	1.09	0.84	2.06	2.47	6.21	68	74	66	99	190	281
0.287	0.100	0.005	394	126	2	1.60	0.87	2.14	3.16	8.78	100	109	114	105	205	302
0.295	0.125	0.005	433	140	2	2.12	0.87	2.15	3.74	12.36	151	153	153	116	230	337
0.299	0.150	0.005	477	155	3	2.16	0.87	2.15	4.13	15.06	209	214	224	125	250	370

Table 10: The optimization results for the $k_\mathrm{L}a = 1.2\ \mathrm{min}^{-1}$ case, $\epsilon^{\mathrm{CC}} = 0.010$ mM/min for the Sudar et al. [77] cofactor regeneration system.

Φ^{STY} /(mM/min)	Φ^{EC} /(μM/min)	Φ^{CC} /(mM/min)	t_f /(min)	$S_i(0)$ /(mM)		$E^j(0)$ /(μM)					A_k /(mM/min)			t_k /(min)		
				1	7	UDH	GlucD	KdgD	KgsalDH	NOX	1	2	3	1	2	3
0.000	0.000	0.005	49,999	1	251	0.00	0.00	0.00	0.00	0.00	0	0	0	736	15,050	33,702
0.165	0.025	0.010	480	86	5	0.39	0.47	1.16	1.44	2.55	29	27	28	170	276	376
0.241	0.050	0.010	358	98	4	0.68	0.73	1.80	1.86	4.16	44	40	42	103	193	271
0.274	0.075	0.010	360	112	4	1.08	0.84	2.06	2.50	6.20	64	71	72	98	186	275
0.290	0.100	0.010	394	127	4	1.59	0.87	2.14	3.17	8.76	100	109	114	105	205	302
0.297	0.125	0.010	433	141	5	2.11	0.87	2.15	3.81	11.45	149	154	164	113	225	333
0.302	0.150	0.010	469	154	5	2.78	0.87	2.15	4.37	15.66	209	201	202	125	249	366

Table 11: The optimization results for the $k_{\mathrm{L}}a = 1.2\ \mathrm{min}^{-1}$ case, $\epsilon^{\mathrm{CC}} = 0.050$ mM/min for the Sudar et al. [77] cofactor regeneration system.

Φ^{STY} /(mM/min)	Φ^{EC} /(μM/min)	Φ^{CC} /(mM/min)	t_{f} /(min)	$S_i(0)$ /(mM)		$E^j(0)$ /(μM)					A_k /(mM/min)			t_k /(min)		
				1	7	UDH	GlucD	KdgD	KgsalDH	NOX	1	2	3	1	2	3
0.000	0.000	0.008	869	0	7	0.00	0.00	0.00	0.00	0.00	0	0	0	305	471	659
0.178	0.025	0.050	506	97	27	0.51	0.49	1.20	1.65	2.56	28	30	29	204	305	406
0.258	0.050	0.050	355	104	19	0.59	0.74	1.83	1.99	4.30	43	42	37	113	202	282
0.295	0.075	0.050	355	118	19	1.04	0.85	2.09	2.62	6.33	68	67	64	101	193	278
0.310	0.100	0.050	390	134	21	1.47	0.88	2.16	3.25	8.66	99	108	113	104	203	299
0.318	0.125	0.050	430	149	23	1.92	0.88	2.19	3.86	12.27	150	152	152	116	228	335
0.322	0.150	0.050	467	163	25	2.40	0.88	2.19	4.46	15.59	208	202	202	124	248	364

Table 12: The optimization results for the $k_{\mathrm{L}}a = 1.2\ \mathrm{min}^{-1}$ case, $\epsilon^{\mathrm{CC}} = 0.100$ mM/min for the Sudar et al. [77] cofactor regeneration system.

Φ^{STY} /(mM/min)	Φ^{EC} /(μM/min)	Φ^{CC} /(mM/min)	t_{f} /(min)	$S_i(0)$ /(mM)		$E^j(0)$ /(μM)					A_k /(mM/min)			t_k /(min)		
				1	7	UDH	GlucD	KdgD	KgsalDH	NOX	1	2	3	1	2	3
0.000	0.000	0.005	49,999	1	253	0.00	0.00	0.00	0.00	0.00	0	0	0	737	16,569	33,719
0.197	0.025	0.100	546	114	58	0.92	0.53	1.31	1.84	2.51	29	32	31	205	329	439
0.280	0.050	0.100	358	112	39	0.60	0.78	1.93	2.27	3.91	41	43	39	107	199	282
0.318	0.075	0.100	352	126	38	0.91	0.89	2.20	2.88	5.86	62	67	70	96	183	269
0.335	0.100	0.100	384	142	41	1.80	0.92	2.28	4.33	8.14	90	110	100	102	198	298
0.343	0.125	0.100	427	160	46	1.78	0.93	2.31	5.04	11.08	140	161	148	111	221	332
0.348	0.150	0.100	465	174	50	1.84	0.93	2.32	5.27	14.89	189	208	216	121	241	359

Table 13: The optimization results for the $k_\mathrm{L}a = 15\ \mathrm{min}^{-1}$ case, $\epsilon^\mathrm{CC} = 0.005$ mM/min for the Sudar et al. [77] cofactor regeneration system.

Φ^STY /(mM/min)	Φ^EC /(μM/min)	Φ^CC /(mM/min)	t_f /(min)	$S_i(0)$ /(mM)		$E^j(0)$ /(μM)					A_k /(mM/min)			t_k /(min)		
				1	7	UDH	GlucD	KdgD	KgsalDH	NOX	1	2	3	1	2	3
0.000	0.000	0.005	49,999	0	234	0.00	0.00	0.00	0.00	0.00	0	0	0	866	20,025	36,081
1.482	0.200	0.005	621	979	3	2.60	3.78	9.50	16.10	24.80	296	283	341	225	350	494
2.351	0.400	0.005	377	1,000	2	5.56	6.21	15.56	17.77	35.01	378	330	325	127	217	295
2.789	0.600	0.005	311	1,000	2	17.32	7.65	19.25	15.26	46.55	460	401	369	69	160	234
2.837	0.800	0.005	305	1,000	2	43.86	7.93	19.75	10.74	62.90	615	469	454	62	151	224
2.845	1.000	0.005	304	1,000	2	68.29	9.33	20.52	8.96	89.36	705	543	472	66	162	229
2.848	1.200	0.005	304	1,000	2	84.41	10.99	21.84	8.89	156.78	485	500	482	81	172	233

Table 14: The optimization results for the $k_\mathrm{L}a = 15\ \mathrm{min}^{-1}$ case, $\epsilon^\mathrm{CC} = 0.010$ mM/min for the Sudar et al. [77] cofactor regeneration system.

Φ^STY /(mM/min)	Φ^EC /(μM/min)	Φ^CC /(mM/min)	t_f /(min)	$S_i(0)$ /(mM)		$E^j(0)$ /(μM)					A_k /(mM/min)			t_k /(min)		
				1	7	UDH	GlucD	KdgD	KgsalDH	NOX	1	2	3	1	2	3
0.000	0.000	0.005	49,999	0	251	0.00	0.00	0.00	0.00	0.00	0	0	0	866	17,663	31,036
1.485	0.200	0.010	620	978	7	2.62	3.78	9.51	16.09	24.63	294	283	342	225	344	492
2.338	0.400	0.010	378	1,000	4	5.52	6.15	15.44	17.91	36.45	378	322	322	138	225	296
2.792	0.600	0.010	310	1,000	3	17.38	7.66	19.26	15.23	46.53	460	393	375	69	159	231
2.839	0.800	0.010	305	1,000	3	43.94	7.96	19.72	10.79	62.83	616	474	444	63	153	226
2.847	1.000	0.010	304	1,000	3	68.53	9.03	20.08	9.29	96.05	646	520	469	69	168	233
2.850	1.200	0.010	303	1,000	3	81.20	10.84	21.87	8.64	153.40	566	567	418	81	177	234

Table 15: The optimization results for the $k_{\mathrm{L}}a = 15\ \mathrm{min}^{-1}$ case, $\epsilon^{\mathrm{CC}} = 0.050$ mM/min for the Sudar et al. [77] cofactor regeneration system.

Φ^{STY}	Φ^{EC}	Φ^{CC}	t_{f}	$S_i(0)$		$E^j(0)$					A_k			t_k		
/(mM/min)	/(μM/min)	/(mM/min)	/(min)	/(mM)		/(μM)					/(mM/min)			/(min)		
				1	7	UDH	GlucD	KdgD	KgsalDH	NOX	1	2	3	1	2	3
0.000	0.000	0.005	49,999	1	253	0.00	0.00	0.00	0.00	0.00	0	0	0	737	17,538	34,165
1.504	0.200	0.050	625	996	33	2.73	3.81	9.61	16.58	23.61	295	287	352	220	334	490
2.352	0.400	0.050	375	1,000	20	5.49	6.16	15.45	17.91	36.58	369	318	319	141	224	294
2.808	0.600	0.050	308	1,000	17	17.41	7.66	19.28	15.24	44.30	475	400	366	66	158	232
2.853	0.800	0.050	303	1,000	17	44.14	7.97	19.73	10.71	62.31	607	465	450	62	150	222
2.861	1.000	0.050	302	1,000	17	69.67	9.63	20.81	9.04	91.44	633	537	472	67	162	230
2.864	1.200	0.050	302	1,000	17	90.78	8.99	28.84	8.64	133.41	590	530	471	76	172	234

Table 16: The optimization results for the $k_{\mathrm{L}}a = 15\ \mathrm{min}^{-1}$ case, $\epsilon^{\mathrm{CC}} = 0.100$ mM/min for the Sudar et al. [77] cofactor regeneration system.

Φ^{STY}	Φ^{EC}	Φ^{CC}	t_{f}	$S_i(0)$		$E^j(0)$					A_k			t_k		
/(mM/min)	/(μM/min)	/(mM/min)	/(min)	/(mM)		/(μM)					/(mM/min)			/(min)		
				1	7	UDH	GlucD	KdgD	KgsalDH	NOX	1	2	3	1	2	3
0.000	0.000	0.005	49,999	0	252	0.00	0.00	0.00	0.00	0.00	0	0	0	860	14,089	33,421
1.522	0.200	0.100	621	1,000	65	3.10	3.85	9.65	16.96	22.47	296	282	349	207	338	486
2.435	0.400	0.100	361	1,000	39	3.49	6.59	16.51	18.91	29.39	303	308	411	89	162	262
2.828	0.600	0.100	306	1,000	34	17.72	7.79	19.54	14.67	43.96	431	373	419	65	138	216
2.871	0.800	0.100	301	1,000	33	44.89	7.99	19.75	10.61	60.24	589	473	454	60	146	221
2.878	1.000	0.100	300	1,000	33	49.27	10.69	20.52	7.42	83.34	786	594	602	57	141	216
2.881	1.200	0.100	300	1,000	33	57.47	13.84	24.37	6.56	86.13	1319	708	564	55	147	216

B Appendix: Theoretical analysis of dynamic processes with dissolved enzymes

B.1 Kinetic models for CRNs a), c) and d) for the theoretical analysis

The four studied chemical reaction networks were modeled with the following matrices and reaction rate models.

CRN a)

$$\mathbf{s} = \begin{bmatrix} S_1 \\ S_2 \\ S_3 \\ c_1 \\ c_2 \end{bmatrix}, \ \mathbf{U} = \begin{bmatrix} -1 & 0 \\ +1 & -1 \\ 0 & +1 \\ -1 & +1 \\ +1 & -1 \end{bmatrix}, \ \mathbf{v} = \begin{bmatrix} v_\mathrm{I} \\ v_\mathrm{II} \end{bmatrix}$$

$$v_\mathrm{I} = \frac{V_{\mathrm{max,I}} \cdot S_1 \cdot c_1}{(K_{\mathrm{m,S_1}} + S_1) \cdot (K_{\mathrm{m,c_1}} + c_1)} \tag{138}$$

$$v_\mathrm{II} = \frac{V_{\mathrm{max,II}} \cdot S_2 \cdot c_2}{(K_{\mathrm{m,S_2}} + S_2) \cdot (K_{\mathrm{m,c_2}} + c_2)} \tag{139}$$

CRN c)

$$\mathbf{s} = \begin{bmatrix} S_1 \\ S_2 \\ S_3 \\ S_4 \\ S_5 \\ S_6 \\ S_7 \\ S_8 \\ c_1 \\ c_2 \end{bmatrix}, \ \mathbf{U} = \begin{bmatrix} -1 & 0 & 0 & 0 & 0 & 0 & 0 \\ +1 & -1 & 0 & 0 & 0 & 0 & 0 \\ 0 & +1 & -1 & 0 & 0 & 0 & 0 \\ 0 & 0 & +1 & -1 & 0 & 0 & 0 \\ 0 & 0 & 0 & +1 & -1 & 0 & 0 \\ 0 & 0 & +1 & 0 & +1 & -1 & 0 \\ 0 & 0 & 0 & 0 & 0 & +1 & -1 \\ 0 & 0 & 0 & 0 & 0 & 0 & +1 \\ -1 & 0 & 0 & -1 & 0 & 0 & +1 \\ +1 & 0 & 0 & +1 & 0 & 0 & -1 \end{bmatrix}, \ \mathbf{v} = \begin{bmatrix} v_{\mathrm{I}} \\ v_{\mathrm{II}} \\ v_{\mathrm{III}} \\ v_{\mathrm{IV}} \\ v_{\mathrm{V}} \\ v_{\mathrm{VI}} \\ v_{\mathrm{VII}} \end{bmatrix}$$

$$v_{\mathrm{I}} = \frac{V_{\mathrm{max,I}} \cdot S_1 \cdot c_1}{(K_{\mathrm{m,S_1}} + S_1) \cdot (K_{\mathrm{m,c_1}} + c_1)} \tag{140}$$

$$v_{\mathrm{II}} = \frac{V_{\mathrm{max,II}} \cdot S_2}{(K_{\mathrm{m,S_2}} + S_2)} \tag{141}$$

$$v_{\mathrm{III}} = \frac{V_{\mathrm{max,III}} \cdot S_3}{(K_{\mathrm{m,S_3}} + S_3)} \tag{142}$$

$$v_{\mathrm{IV}} = \frac{V_{\mathrm{max,IV}} \cdot S_1 \cdot c_1}{(K_{\mathrm{m,S_1}} + S_1) \cdot (K_{\mathrm{m,c_1}} + c_1)} \tag{143}$$

$$v_{\mathrm{V}} = \frac{V_{\mathrm{max,V}} \cdot S_5}{(K_{\mathrm{m,S_5}} + S_5)} \tag{144}$$

$$v_{\mathrm{VI}} = \frac{V_{\mathrm{max,VI}} \cdot S_6}{(K_{\mathrm{m,S_6}} + S_6)} \tag{145}$$

$$v_{\mathrm{VII}} = \frac{V_{\mathrm{max,VII}} \cdot S_7 \cdot c_2}{(K_{\mathrm{m,S_7}} + S_7) \cdot (K_{\mathrm{m,c_2}} + c_1)} \tag{146}$$

CRN d)

$$\mathbf{s} = \begin{bmatrix} S_1 \\ S_2 \\ S_3 \\ S_4 \\ S_5 \\ S_6 \\ c_1 \\ c_2 \end{bmatrix}, \ \mathbf{U} = \begin{bmatrix} -1 & 0 & 0 & 0 & 0 \\ +1 & -1 & 0 & 0 & 0 \\ 0 & +1 & -1 & 0 & 0 \\ 0 & 0 & +1 & -1 & 0 \\ 0 & 0 & 0 & +1 & -1 \\ 0 & 0 & 0 & 0 & +1 \\ -1 & +1 & 0 & +1 & -1 \\ +1 & -1 & 0 & -1 & +1 \end{bmatrix}, \ \mathbf{v} = \begin{bmatrix} v_{\mathrm{I}} \\ v_{\mathrm{II}} \\ v_{\mathrm{III}} \\ v_{\mathrm{IV}} \\ v_{\mathrm{V}} \end{bmatrix}$$

$$v_{\mathrm{I}} = \frac{V_{\mathrm{max,I}} \cdot S_1 \cdot c_1}{(K_{\mathrm{m,S_1}} + S_1) \cdot (K_{\mathrm{m,c_1}} + c_1)} \tag{147}$$

$$v_{\mathrm{II}} = \frac{V_{\mathrm{max,II}} \cdot S_2 \cdot c_2}{(K_{\mathrm{m,S_2}} + S_2) \cdot (K_{\mathrm{m,c_2}} + c_2)} \tag{148}$$

$$v_{\mathrm{III}} = \frac{V_{\mathrm{max,III}} \cdot S_3}{(K_{\mathrm{m,S_3}} + S_3)} \tag{149}$$

$$v_{\mathrm{IV}} = \frac{V_{\mathrm{max,IV}} \cdot S_4 \cdot c_2}{(K_{\mathrm{m,S_4}} + S_4) \cdot (K_{\mathrm{m,c_2}} + c_2)} \tag{150}$$

$$v_{\mathrm{V}} = \frac{V_{\mathrm{max,V}} \cdot S_5 \cdot c_1}{(K_{\mathrm{m,S_5}} + S_5) \cdot (K_{\mathrm{m,c_1}} + c_1)} \tag{151}$$

B.2 A parameterized model for CRN b)

A model was developed for CRN b) using kinetic data from Sutiono et al. [56] The material balance for the 1,2,4-butanetriol cascade is as follows:

$$\frac{d\mathbf{s}}{dt} = \mathbf{U} \cdot \mathbf{v} \tag{152}$$

where,

$$\mathbf{s} = \begin{bmatrix} S_1 \\ S_2 \\ S_3 \\ S_4 \\ S_5 \\ S_6 \\ c_1 \\ c_2 \end{bmatrix}, \ \mathbf{U} = \begin{bmatrix} -1 & 0 & 0 & 0 & 0 \\ +1 & -1 & 0 & 0 & 0 \\ 0 & +1 & -1 & 0 & 0 \\ 0 & 0 & +1 & -1 & 0 \\ 0 & 0 & 0 & +1 & -1 \\ 0 & 0 & 0 & 0 & +1 \\ -1 & 0 & 0 & 0 & +1 \\ +1 & 0 & 0 & 0 & -1 \end{bmatrix}, \ \mathbf{v} = \begin{bmatrix} v_{\mathrm{I}} \\ v_{\mathrm{II}} \\ v_{\mathrm{III}} \\ v_{\mathrm{IV}} \\ v_{\mathrm{V}} \end{bmatrix}$$

The same reaction rate models chosen and reported in Sutiono et al. were used in the model [56]. The molecular weights for the enzymes were also taken from the same work [56]. The second reaction step, was not kinetically characterized by Sutiono et al. [56] and instead large amount of enzymes were used to ensure that that the step is not rate limiting. This reaction step is described in our model with a first-order kinetic with a large kinetic parameter to model this behaviour.

$$v_{\mathrm{I}} = \frac{V_{\mathrm{max,I}} \cdot c_1}{K_1 + c_1 \cdot (1 + \frac{K_2}{S_1}) \cdot (1 + \frac{S_1}{K_3})} \tag{153}$$

$$v_{\mathrm{II}} = 10000 \cdot S_3 \tag{154}$$

$$v_{\mathrm{III}} = \frac{V_{\mathrm{max,III}} \cdot S_3}{K_4 + S_3} \tag{155}$$

$$v_{\mathrm{IV}} = \frac{V_{\mathrm{max,IV}} \cdot S_4}{K_5 + S_4} \tag{156}$$

$$v_{\mathrm{V}} = \frac{V_{\mathrm{max,V}} \cdot S_5 \cdot c_2}{K_6 \cdot K_7 + K_7 \cdot S_5 + S_5 \cdot c_2} \tag{157}$$

where, $V_{\mathrm{max},j} = k_{\mathrm{cat},j} \cdot E_j$.

Table 17: The turnover numbers for the enzymes.

j	$k_{\mathrm{cat},j}/(\mathrm{s}^{-1})$
I	20.4
II	N/A
III	11.9
IV	0.9
V	12.0

Table 18: The kinetic parameters for the enzymes.

i	$K_i/(\mathrm{mM})$
1	0.2
2	1.4
3	524.5
4	0.5
5	7.5
6	16.8
7	1.5

A simulation of the model using the same initial conditions as in Figure 2 of Sutiono et al. [56] is given in Figure 40. The model follows the characteristic linear patern of redox balanced cascades (also observed experimentally in Figure 2 of Sutiono et al). The model predicts full conversion of D-xylose after 35 hours for the experiment presented in Figure 2 of Sutiono et al. In the actual experiment full conversion was achieved after 45 hours. Therefore, compared to that experiment our model underestimates the reaction time required by 22%. This model fit to experiment was considered suficient and our model was used to demonstrate how multi-objective optimization can be applied.

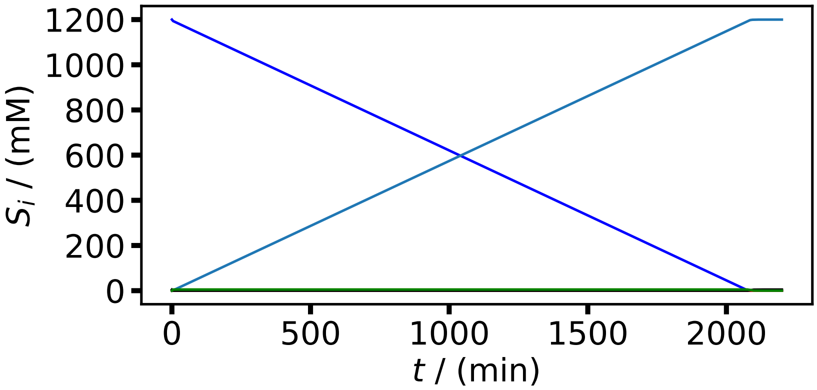

Figure 40: Simulation of the model for the following titers: $S_1^0 = 180$ g/l, $c_1^0 = 3.3$ g/l, $E_{\mathrm{I}} = 0.2$ g/l, $E_{\mathrm{II}} = 0.1$ g/l, $E_{\mathrm{III}} = 0.3$ g/l, $E_{\mathrm{IV}} = 2$ g/l, $E_{\mathrm{V}} = 0.5$ g/l . — S_1, — S_6, — c_1, — c_2, the rest of the substrates stay at very low concentrations.

B.3 Supporting evidence for the quasi steady-state approximation

In the following figures we simulate CRNs c) and d) with parameter values selected to be in typical ranges to demonstrate that certain intermediates and the cofactors reach a quasi-steady state. Note that in CRN c) not all intermediates reach a quasi steady-state. S_4 does not appear in the characteristic equation and therefore is not constrained to be below the cofactor concentration like the rest of the intermediates.

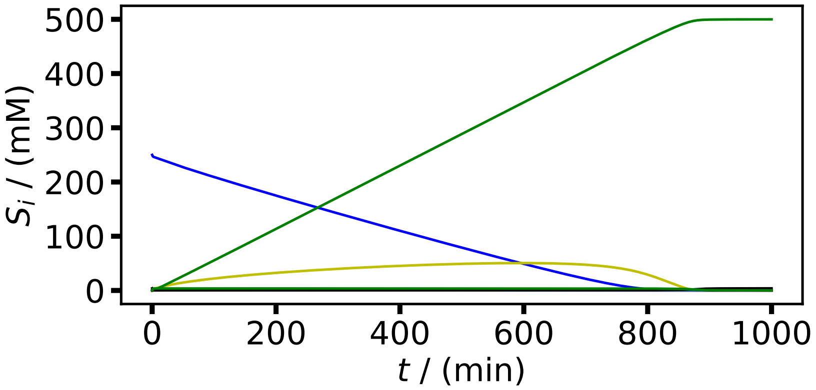

Figure 41: Simulation of the concentration profiles of CRN c) for selected parameter values: $S_1^0 = 250$ mM, $c_1^0 = 4$ mM, $c_2^0 = 0$ mM, $S_2^0 = 0$ mM, $S_3^0 = 0$ mM, $S_4^0 = 0$ mM, $S_5^0 = 0$ mM, $S_6^0 = 0$ mM, $S_7^0 = 0$ mM, $S_8^0 = 0$ mM, all $V_{\mathrm{max,j}} = 20$ mM min^{-1} and, all $K_{\mathrm{m,j}} = 15$ mM. — S_1, — S_4, — S_8, the rest of the substrates and cofactors are kept at very low concentrations.

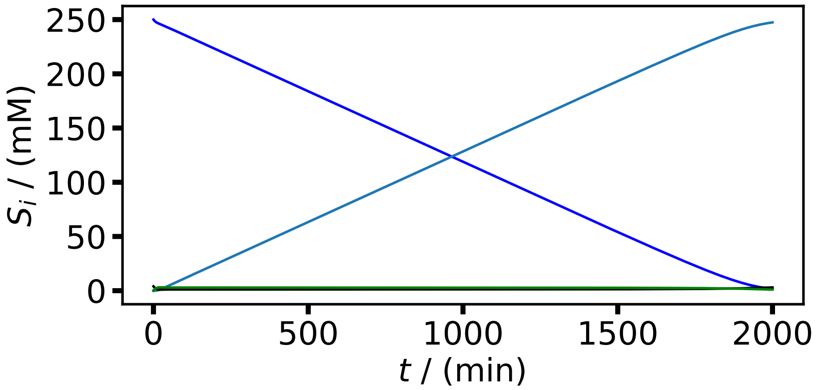

Figure 42: Simulation of the concentration profiles of CRN d) for elected parameter values: $S_1^0 = 250$ mM, $c_1^0 = 4$ mM, $c_2^0 = 0$ mM, $S_2^0 = 0$ mM, $S_3^0 = 0$ mM, $S_4^0 = 0$ mM, $S_5^0 = 0$ mM, $V_{\mathrm{max,I}} = 2$ mM min^{-1}, all other maximum reaction rates $V_{\mathrm{max,j}} = 20$ mM min^{-1} and, all $K_{\mathrm{m,j}} = 15$ mM. — S_1, — S_6, — c_1, — c_2, the rest of the substrates stay at very low concentrations.

A simulation for CRN a) was given in the main article. The parameter values used there were: $V_{\mathrm{max,I}} = 45$ mM min^{-1}, $V_{\mathrm{max,II}} = 50$ mM min^{-1}, $K_{\mathrm{m,S_1}} = 15$ mM, $K_{\mathrm{m,c_1}} = 25$ mM, $K_{\mathrm{m,S_2}} = 30$ mM, $K_{\mathrm{m,c_2}} = 10$ mM.

C Appendix: Systems with immobilized enzymes

C.1 Analytical solutions for the concentration profiles inside pore α-A and α-B

Using the methodology first established by Professor Ernst Thiele [95] and presented in detail in Professor Octave Levenspiel's book [99] we derive material balances for the pores. For substrate S_1, we derive the following material balance around pore α-A.

$$\frac{d^2 S_{1,\alpha-\mathrm{A}}}{dx^2} = \frac{k_{\mathrm{A}} \cdot E_{\mathrm{A},\alpha-\mathrm{A}}}{D_1} \cdot S_{1,\alpha-\mathrm{A}} \tag{158}$$

The following two boundary conditions are considered:

$$S_{1,\alpha-\mathrm{A}}|_{x=0} = S_{1,0} \tag{159}$$

$$\frac{dS_{1,\alpha-\mathrm{A}}}{dx}\Big|_{x=L} = 0 \tag{160}$$

Equation (158) is a second order, linear and homogeneous differential equation with constant coefficients. The general solution is:

$$S_{1,\alpha-\mathrm{A}} = c_1 \cdot e^{m_{1,\alpha-\mathrm{A}} \cdot x} + c_2 \cdot e^{-m_{1,\alpha-\mathrm{A}} \cdot x} \tag{161}$$

with

$$m_{1,\alpha-\mathrm{A}} = \sqrt{\frac{k_{\mathrm{A}} \cdot E_{\mathrm{A},\alpha-\mathrm{A}}}{D_1}} \tag{162}$$

$$c_1 = \frac{S_{1,0} \cdot e^{-m_{1,\alpha-\mathrm{A}} \cdot L}}{e^{m_{1,\alpha-\mathrm{A}} \cdot L} + e^{-m_{1,\alpha-\mathrm{A}} \cdot L}} \tag{163}$$

$$c_2 = \frac{S_{1,0} \cdot e^{m_{1,\alpha-\mathrm{A}} \cdot L}}{e^{m_{1,\alpha-\mathrm{A}} \cdot L} + e^{-m_{1,\alpha-\mathrm{A}} \cdot L}} \tag{164}$$

For substrate S_2, we derive the following material balance around pore α-A.

$$\frac{d^2 S_{2,\alpha-\mathrm{A}}}{dx^2} = -\frac{k_\mathrm{A} \cdot E_{\mathrm{A},\alpha-\mathrm{A}}}{D_2} \cdot S_{1,\alpha-\mathrm{A}} \tag{165}$$

Substituting the solution we obtained for $S_{1,\alpha-\mathrm{A}}$ in Equation (165) we get:

$$\frac{d^2 S_{2,\alpha-\mathrm{A}}}{dx^2} = -\frac{k_\mathrm{A} \cdot E_{\mathrm{A},\alpha-\mathrm{A}}}{D_2} \cdot c_1 \cdot e^{m_{1,\alpha-\mathrm{A}} \cdot x} - \frac{k_\mathrm{A} \cdot E_{\mathrm{A},\alpha-\mathrm{A}}}{D_2} \cdot c_2 \cdot e^{-m_{1,\alpha-\mathrm{A}} \cdot x} \tag{166}$$

The following two boundary conditions are considered:

$$S_{2,\alpha-\mathrm{A}}|_{x=0} = S_{2,0} \tag{167}$$

$$\frac{dS_{2,\alpha-\mathrm{A}}}{dx}\Big|_{x=L} = 0 \tag{168}$$

Equation (166) is a second order, linear and heterogeneous differential equation with constant coefficients. The general solution is:

$$S_{2,\alpha-\mathrm{A}} = c_3 \cdot x + c_4 + c_5 \cdot e^{m_{1,\alpha-\mathrm{A}} \cdot x} + c_6 \cdot e^{-m_{1,\alpha-\mathrm{A}} \cdot x} \tag{169}$$

with

$$c_3 = -c_5 \cdot m_{1,\alpha-\mathrm{A}} \cdot e^{m_{1,\alpha-\mathrm{A}} \cdot L} + c_6 \cdot m_{1,\alpha-\mathrm{A}} \cdot e^{-m_{1,\alpha-\mathrm{A}} \cdot L} \tag{170}$$

$$c_4 = S_{2,0} - c_5 - c_6 \tag{171}$$

$$c_5 = -\frac{k_\mathrm{A} \cdot E_{\mathrm{A},\alpha-\mathrm{A}} \cdot c_1}{D_2 \cdot m_{1,\alpha-\mathrm{A}}^2} \tag{172}$$

$$c_6 = -\frac{k_\mathrm{A} \cdot E_{\mathrm{A},\alpha-\mathrm{A}} \cdot c_2}{D_2 \cdot m_{1,\alpha-\mathrm{A}}^2} \tag{173}$$

For substrate S_2, we derive the following material balance around pore α-B.

$$\frac{d^2S_{2,\alpha-\mathrm{B}}}{dx^2} = \frac{k_\mathrm{B} \cdot E_{\mathrm{B},\alpha-\mathrm{B}}}{D_2} \cdot S_{2,\alpha-\mathrm{B}} \tag{174}$$

The following two boundary conditions are considered:

$$S_{2,\alpha-\mathrm{B}}|_{x=0} = S_{2,0} \tag{175}$$

$$\frac{dS_{2,\alpha-\mathrm{B}}}{dx}\Big|_{x=L} = 0 \tag{176}$$

Equation (174) is a second order, linear and homogeneous differential equation with constant coefficients. The general solution is:

$$S_{2,\alpha-\mathrm{B}} = d_1 \cdot e^{m_{2,\alpha-\mathrm{B}} \cdot x} + d_2 \cdot e^{-m_{2,\alpha-\mathrm{B}} \cdot x} \tag{177}$$

with

$$m_{2,\alpha-\mathrm{B}} = \sqrt{\frac{k_\mathrm{B} \cdot E_{\mathrm{B},\alpha-\mathrm{B}}}{D_2}} \tag{178}$$

$$d_1 = \frac{S_{2,0} \cdot e^{-m_{2,\alpha-\mathrm{B}} \cdot L}}{e^{m_{2,\alpha-\mathrm{B}} \cdot L} + e^{-m_{2,\alpha-\mathrm{B}} \cdot L}} \tag{179}$$

$$d_2 = \frac{S_{2,0} \cdot e^{m_{2,\alpha-\mathrm{B}} \cdot L}}{e^{m_{2,\alpha-\mathrm{B}} \cdot L} + e^{-m_{2,\alpha-\mathrm{B}} \cdot L}} \tag{180}$$

For substrate S_3, we derive the following material balance around pore α-B.

$$\frac{d^2S_{3,\alpha-\mathrm{B}}}{dx^2} = -\frac{k_\mathrm{B} \cdot E_{\mathrm{B},\alpha-\mathrm{B}}}{D_3} \cdot S_{2,\alpha-\mathrm{B}} \tag{181}$$

Substituting the solution we obtained for $S_{2,\alpha-\mathrm{B}}$ in Equation (181) we get:

$$\frac{d^2S_{3,\alpha-\mathrm{B}}}{dx^2} = -\frac{k_\mathrm{B} \cdot E_{\mathrm{B},\alpha-\mathrm{B}}}{D_3} \cdot d_1 \cdot e^{m_{2,\alpha-\mathrm{B}} \cdot x} - \frac{k_\mathrm{B} \cdot E_{\mathrm{B},\alpha-\mathrm{B}}}{D_3} \cdot d_2 \cdot e^{-m_{2,\alpha-\mathrm{B}} \cdot x} \tag{182}$$

The following two boundary conditions are considered:

$$S_{3,\alpha-\mathrm{B}}|_{x=0} = S_{3,0} \tag{183}$$

$$\frac{dS_{3,\alpha\text{-B}}}{dx}\Big|_{x=L} = 0 \tag{184}$$

Equation (182) is a second order, linear and heterogeneous differential equation with constant coefficients. We applied the appropriate methodology by first solving the corresponding homogeneous equation and then solving for the heterogeneous terms. The general solution is:

$$S_{3,\alpha-\mathrm{B}} = d_3 \cdot x + d_4 + d_5 \cdot e^{m_{2,\alpha-\mathrm{B}} \cdot x} + d_6 \cdot e^{-m_{2,\alpha-\mathrm{B}} \cdot x} \tag{185}$$

with

$$d_3 = -\left(d_5 \cdot m_{2,\alpha-\mathrm{B}} \cdot e^{m_{2,\alpha-\mathrm{B}} \cdot L} - d_6 \cdot m_{2,\alpha-\mathrm{B}} \cdot e^{-m_{2,\alpha-\mathrm{B}} \cdot L}\right) \tag{186}$$

$$d_4 = S_{3,0} - d_5 - d_6 \tag{187}$$

$$d_5 = -\frac{k_\mathrm{B} \cdot E_{\mathrm{B},\alpha-\mathrm{B}} \cdot d_1}{D_3 \cdot m_{2,\alpha-\mathrm{B}}^2} \tag{188}$$

$$d_6 = -\frac{k_\mathrm{B} \cdot E_{\mathrm{B},\alpha-\mathrm{B}} \cdot d_2}{D_3 \cdot m_{2,\alpha-\mathrm{B}}^2} \tag{189}$$

C.2 Macro kinetic expressions for the single immobilization case

The macro kinetics or apparent reaction rates, v_k, for the single immobilization case can then be calculated by applying Fick's law at the start ($x = 0$) of the corresponding pore. Since the concentration profiles were calculated analytically, we can also derive analytical expressions for the concentration gradient at the beginning of the pores and use this to get an analytical expression of the apparent reaction rates. For the single immobilization case, these are presented below.

$$v_\mathrm{I} = p_{1,\alpha-\mathrm{A}} \cdot S_{1,0} \tag{190}$$

$$v_\mathrm{II} = p_{2,\alpha-\mathrm{B}} \cdot S_{2,0} \tag{191}$$

with

$$p_{1,\alpha-\mathrm{A}} = N_{\alpha-\mathrm{A}} \cdot A \cdot D_1 \cdot m_{1,\alpha-\mathrm{A}} \cdot \tanh(m_{1,\alpha-\mathrm{A}} \cdot L) \tag{192}$$

$$p_{2,\alpha-\mathrm{B}} = N_{\alpha-\mathrm{B}} \cdot A \cdot D_2 \cdot m_{2,\alpha-\mathrm{B}} \cdot \tanh(m_{2,\alpha-\mathrm{B}} \cdot L) \tag{193}$$

C.3 Analytical solutions for the concentration profiles inside pore β

For substrate S_1, we derive the following material balance around pore β.

$$\frac{d^2 S_{1,\beta}}{dx^2} = \frac{k_\mathrm{A} \cdot E_{\mathrm{A},\beta}}{D_1} \cdot S_{1,\beta} \tag{194}$$

The following two boundary conditions apply:

$$S_{1,\beta}|_{x=0} = S_{1,0} \tag{195}$$

$$\frac{dS_{1,\beta}}{dx}\Big|_{x=L} = 0 \tag{196}$$

Equation (194) is a second order, linear and homogeneous differential equation with constant coefficients. The general solution is:

$$S_{1,\beta} = e_1 \cdot e^{m_{1,\beta} \cdot x} + e_2 \cdot e^{-m_{1,\beta} \cdot x} \tag{197}$$

with

$$m_{1,\beta} = \sqrt{\frac{k_\mathrm{A} \cdot E_{\mathrm{A},\beta}}{D_1}} \tag{198}$$

In order to find the particular solution we use the two boundary conditions given in Equations (195) and (196).

$$e_1 = \frac{S_{1,0} \cdot e^{-m_{1,\beta} \cdot L}}{e^{m_{1,\beta} \cdot L} + e^{-m_{1,\beta} \cdot L}} \tag{199}$$

$$e_2 = \frac{S_{1,0} \cdot e^{m_{1,\beta} \cdot L}}{e^{m_{1,\beta} \cdot L} + e^{-m_{1,\beta} \cdot L}} \tag{200}$$

For substrate S_2, we can write the following material balance around pore β.

$$\frac{d^2S_{2,\beta}}{dx^2} - \frac{k_\mathrm{B} \cdot E_{\mathrm{B},\beta}}{D_2} \cdot S_{2,\beta} = -\frac{k_\mathrm{A} \cdot E_{\mathrm{A},\beta}}{D_2} \cdot S_{1,\beta} \tag{201}$$

Substituting the solution we obtained for $S_{1,\beta}$ in Equation (201) we get:

$$\frac{d^2S_{2,\beta}}{dx^2} - \frac{k_\mathrm{B} \cdot E_{\mathrm{B},\beta}}{D_2} \cdot S_{2,\beta} = -\frac{k_\mathrm{A} \cdot E_{\mathrm{A},\beta}}{D_2} \cdot e_1 \cdot e^{m_{1,\beta} \cdot x} - \frac{k_\mathrm{A} \cdot E_{\mathrm{A},\beta}}{D_2} \cdot e_2 \cdot e^{-m_{1,\beta} \cdot x} \tag{202}$$

The following two boundary conditions are considered:

$$S_{2,\beta}|_{x=0} = S_{2,0} \tag{203}$$

$$\frac{dS_{2,\beta}}{dx}\Big|_{x=L} = 0 \tag{204}$$

Equation (202) is a second order, linear and heterogeneous differential equation with constant coefficients. We applied the appropriate methodology by first solving the corresponding homogeneous equation and then solving for the heterogeneous terms. The general solution is:

$$S_{2,\beta} = e_3 \cdot e^{m_{2,\beta} \cdot x} + e_4 \cdot e^{-m_{2,\beta} \cdot x} + e_5 \cdot e^{m_{1,\beta} \cdot x} + e_6 \cdot e^{-m_{1,\beta} \cdot x} \tag{205}$$

with

$$m_{2,\beta} = \sqrt{\frac{k_\mathrm{B} \cdot E_{\mathrm{B},\beta}}{D_2}} \tag{206}$$

$$e_3 = S_{2,0} - e_4 - e_5 - e_6 \tag{207}$$

$$e_4 = \frac{m_{2,\beta} \cdot e^{m_{2,\beta} \cdot L} \cdot (S_{2,0} - e_5 - e_6)}{m_{2,\beta} \cdot e^{m_{2,\beta} \cdot L} + m_{2,\beta} \cdot e^{-m_{2,\beta} \cdot L}} + \frac{m_{1,\beta} \cdot (e_5 \cdot e^{m_{1,\beta} \cdot L} - e_6 \cdot e^{-m_{1,\beta} \cdot L})}{m_{2,\beta} \cdot e^{m_{2,\beta} \cdot L} + m_{2,\beta} \cdot e^{-m_{2,\beta} \cdot L}} \tag{208}$$

$$e_5 = -\frac{k_A \cdot E_A \cdot e_1}{D_2 \cdot (m_{1,\beta}^2 - m_{2,\beta}^2)} \tag{209}$$

$$e_6 = -\frac{k_A \cdot E_A \cdot e_2}{D_2 \cdot (m_{1,\beta}^2 - m_{2,\beta}^2)} \tag{210}$$

For substrate S_3, we derive the following material balance around pore β.

$$\frac{d^2 S_{3,\beta}}{dx^2} = -\frac{k_\mathrm{B} \cdot E_{\mathrm{B},\beta}}{D_3} \cdot S_{2,\beta} \tag{211}$$

The following two boundary conditions are considered:

$$S_{3,\beta}|_{x=0} = S_{3,0} \tag{212}$$

$$\frac{dS_{3,\beta}}{dx}\Big|_{x=L} = 0 \tag{213}$$

Equation (211) is a second order, linear and heterogeneous differential equation with constant coefficients. We applied the appropriate methodology by first solving the corresponding homogeneous equation and then solving for the heterogeneous terms. The general solution is:

$$S_{3,\beta} = e_7 + e_8 \cdot x + e_9 \cdot e^{m_{2,\beta} \cdot x} + e_{10} \cdot e^{-m_{2,\beta} \cdot x} + e_{11} \cdot e^{m_{1,\beta} \cdot x} \tag{214}$$

with

$$e_7 = S_{3,0} - e_9 - e_{10} - e_{11} - e_{12} \tag{215}$$

$$e_8 = m_{2,\beta} \cdot \left(-e_9 \cdot e^{m_{2,\beta} \cdot L} + e_{10} \cdot e^{-m_{2,\beta} \cdot L}\right) + m_{1,\beta} \cdot \left(-e_{11} \cdot e^{m_{1,\beta} \cdot L} + e_{12} \cdot e^{-m_{2,\beta} \cdot L}\right) \tag{216}$$

$$e_9 = -\frac{k_B \cdot E_B \cdot e_3}{D_3 \cdot m_{2,\beta}^2} \tag{217}$$

$$e_{10} = -\frac{k_B \cdot E_B \cdot e_4}{D_3 \cdot m_{2,\beta}^2} \tag{218}$$

$$e_{11} = -\frac{k_B \cdot E_B \cdot e_5}{D_3 \cdot m_{1,\beta}^2} \tag{219}$$

$$e_{12} = -\frac{k_B \cdot E_B \cdot e_6}{D_3 \cdot m_{1,\beta}^2} \tag{220}$$

C.4 Macro kinetic expressions for the co-immobilization case

The macro kinetics or apparent reaction rates, v_k, for the co-immobilization spatial immobilization distribution can then be calculated by applying Fick's law at the start ($x = 0$) of the corresponding pore. Since the concentration profiles were calculated analytically, we can also derive analytical expressions for the concentration gradient at the beginning of the pores and use this to get an analytical expression of the apparent reaction rates. For the co-immobilization case, these are presented below.

$$v_{\mathrm{I}} = p_{1,\beta} \cdot S_{1,0} \tag{221}$$

$$v_{\mathrm{II}} = p_{2,\beta} \cdot S_{1,0} + p_{3,\beta} \cdot S_{2,0} \tag{222}$$

with

$$p_{1,\beta} = N_\beta \cdot A \cdot D_1 \cdot m_{1,\beta} \cdot \tanh(m_{1,\beta} \cdot L) \tag{223}$$

$$p_{2,\beta} = N_\beta \cdot A \cdot D_2 \cdot m_{2,\beta} \cdot \tanh(m_{2,\beta} \cdot L) \tag{224}$$

$$p_{3,\beta} = \frac{N_\beta \cdot A \cdot D_1 \cdot m_{1,\beta}^2 \cdot m_{2,\beta}^2}{m_{1,\beta}^2 - m_{2,\beta}^2} \cdot [\frac{\tanh(m_{2,\beta} \cdot L)}{m_{2,\beta}} - \frac{\tanh(m_{1,\beta} \cdot L)}{m_{1,\beta}}] \tag{225}$$

C.5 Time profiles for the single and co-immobilization cases

The following system of first order differential equations represents the dynamic material balances for the batch reactor when single immobilization is used as a spatial immobilization strategy (α):

$$\frac{dS_{1,0}}{dt} = -p_{1,\alpha-\mathrm{A}} \cdot S_{1,0} \tag{226}$$

$$\frac{dS_{2,0}}{dt} = +p_{1,\alpha-\mathrm{A}} \cdot S_{1,0} - p_{2,\alpha-\mathrm{B}} \cdot S_{2,0} \tag{227}$$

$$\frac{dS_{3,0}}{dt} = -p_{2,\alpha-\mathrm{B}} \cdot S_{2,0} \tag{228}$$

with the following initial conditions:

$$S_{1,0}|_{t=0} = S_{1,0}^{0} \tag{229}$$

$$S_{2,0}|_{t=0} = 0 \tag{230}$$

$$S_{3,0}|_{t=0} = 0 \tag{231}$$

This is a system of first order, linear differential equations. The solution is:

$$S_{1,0} = S_{1,0}^{0} \cdot e^{-p_{1,\alpha-\mathrm{A}} \cdot t} \tag{232}$$

$$S_{2,0} = S_{1,0}^{0} \cdot \frac{p_{1,\alpha-\mathrm{A}}}{p_{2,\alpha-\mathrm{B}} - p_{1,\alpha-\mathrm{A}}} \cdot \left(e^{-p_{1,\alpha-\mathrm{A}} \cdot t} - e^{-p_{2,\alpha-\mathrm{B}} \cdot t}\right) \tag{233}$$

$$S_{3,0} = S_{1,0}^{0} - S_{1,0} - S_{2,0} \tag{234}$$

The following system of first order differential equations represents the dynamic material balances for the batch reactor when co-immobilization is used as a spatial immobilization strategy (β):

$$\frac{dS_{1,0}}{dt} = -p_{1,\beta} \cdot S_{1,0} \tag{235}$$

$$\frac{dS_{2,0}}{dt} = +p_{1,\beta} \cdot S_{1,0} - p_{2,CI} \cdot S_{1,0} - p_{3,CI} \cdot S_{2,0} \tag{236}$$

$$\frac{dS_{3,0}}{dt} = p_{2,CI} \cdot S_{1,0} + p_{3,CI} \cdot S_{2,0} \tag{237}$$

with initial conditions:

$$S_{1,0}|_{t=0} = S_{1,0}^{0} \tag{238}$$

$$S_{2,0}|_{t=0} = 0 \tag{239}$$

$$S_{3,0}|_{t=0} = 0 \tag{240}$$

This is a system of first order, linear differential equations. The solution is:

$$S_{1,0} = S_{1,0}^{0} \cdot e^{-p_{1,\beta} \cdot t} \tag{241}$$

$$S_{2,0} = S_{1,0}^{0} \cdot \frac{p_{1,\beta} - p_{3,\beta}}{p_{2,\beta} - p_{1,\beta}} \cdot \left(e^{-p_{1,\beta} \cdot t} - e^{-p_{2,\beta} \cdot t}\right) \tag{242}$$

$$S_{3,0} = S_{1,0}^{0} - S_{1,0} - S_{2,0} \tag{243}$$

C.6 Case-specific simplification

The ratio $\mathcal{R}_{\alpha/\beta}$ can be calculated by the following expression:

$$\mathcal{R}_{\alpha/\beta} = \frac{S_{3,0}^{\alpha}}{S_{3,0}^{\beta}} = \frac{1 - e^{-p_{1,\alpha-\mathrm{A}} \cdot t} - \frac{p_{1,\alpha-\mathrm{A}}}{p_{2,\alpha-\mathrm{B}} - p_{1,\alpha-\mathrm{A}}} \cdot \left(e^{-p_{1,\alpha-\mathrm{A}} \cdot t} - e^{-p_{2,\alpha-\mathrm{B}} \cdot t}\right)}{1 - e^{-p_{1,\beta} \cdot t} - \frac{p_{1,\beta} - p_{3,\beta}}{p_{2,\beta} - p_{1,\beta}} \cdot \left(e^{-p_{1,\beta} \cdot t} - e^{-p_{2,\beta} \cdot t}\right)} \tag{244}$$

When the products $m_{1,\mathrm{n}} \cdot L$ and $m_{2,\mathrm{n}} \cdot L$ are larger than one, all tangent hyperbolicus terms become roughly equal to one. In addition, when considering cases where $D_1 = D_2 = D$, Equation (244) can be simplified. The terms $p_{1,n}$, $p_{2,n}$ and $p_{3,n}$ will now be as follows:

$$p_{1,\alpha-\mathrm{A}} = N_{\alpha-\mathrm{A}} \cdot A \cdot D \cdot m_{1,\alpha-\mathrm{A}} \tag{245}$$

$$p_{2,\alpha\text{-B}} = N_{\alpha\text{-B}} \cdot A \cdot D \cdot m_{2,\alpha\text{-B}} \tag{246}$$

$$p_{1,\beta} = N_{\beta} \cdot A \cdot D \cdot m_{1,\beta} \tag{247}$$

$$p_{2,\beta} = N_{\beta} \cdot A \cdot D \cdot m_{2,\beta} \tag{248}$$

$$p_{3,\beta} = \frac{N_{\beta} \cdot A \cdot D \cdot m_{1,\beta}^2 \cdot m_{2,\beta}^2}{m_{1,\beta}^2 - m_{2,\beta}^2} \cdot \left[\frac{1}{m_{2,\beta}} - \frac{1}{m_{1,\beta}}\right] \tag{249}$$

They can be expressed in terms of $p_{1,\alpha\text{-A}}$ and $p_{2,\alpha\text{-B}}$ as follows:

$$p_{1,\alpha\text{-B}} = p_{1,\alpha\text{-A}} \tag{250}$$

$$p_{1,\beta} = \sqrt{2} \cdot p_{1,\alpha\text{-A}} \tag{251}$$

$$p_{2,\beta} = \sqrt{2} \cdot p_{2,\alpha\text{-B}} \tag{252}$$

$$p_{3,\beta} = \frac{\sqrt{2} \cdot p_{1,\alpha\text{-A}} \cdot p_{2,\alpha\text{-B}}}{p_{1,\alpha\text{-A}} + p_{2,\alpha\text{-B}}} \tag{253}$$

We define two moduli, μ_1 and μ_2 as follows:

$$\mu_1 = p_{1,\alpha\text{-A}} \cdot t \tag{254}$$

$$\mu_2 = p_{2,\alpha\text{-B}} \cdot t \tag{255}$$

Equation (244) can then be reformulated as follows:

$$\mathcal{R}_{\alpha/\beta} = \frac{1 - e^{-\mu_1} - \frac{\mu_1}{\mu_2 - \mu_1} \cdot \left(e^{-\mu_1} - e^{-\mu_2}\right)}{1 - e^{-\sqrt{2}\cdot\mu_1} - \frac{\mu_1^2}{\mu_2^2 - \mu_1^2} \cdot \left(e^{-\sqrt{2}\cdot\mu_1} - e^{-\sqrt{2}\cdot\mu_2}\right)} \tag{256}$$

C.7 Analytical solutions for design II

The derivation of the analytical solutions for designs I and III can be found in Appendix C. In this section we derive the analytical solutions for design II:

For τ in [0, τ_{f}/c]:

$$\frac{dS_{1,0}}{d\tau} = -c \cdot p_{1,\text{a-A}} \cdot S_{1,0} \tag{257}$$

Integrating from 0 to τ:

$$\int_0^{\tau} \frac{dS_{1,0}}{S_{1,0}} = -c \cdot p_{1,\text{a-A}} \cdot \int_0^{\tau} d\tau \tag{258}$$

The analytical solution is:

$$S_{1,0}(\tau) = S_{1,0}(0) \cdot e^{-c \cdot p_{1,\text{a-A}} \cdot \tau} \tag{259}$$

From the material balance:

$$S_{2,0}(\tau) = S_{1,0}(0) - S_{1,0}(0) \cdot e^{-c \cdot p_{1,\text{a-A}} \cdot \tau} \tag{260}$$

For τ in [τ_{f}/c, τ_{f}]:

$$\frac{dS_{2,0}}{d\tau} = -c \cdot p_{2,\text{a-B}} \cdot S_{2,0} \tag{261}$$

Integrating from τ_{f}/c to τ:

$$\int_{\tau_{\mathrm{f}}/c}^{\tau} \frac{dS_{2,0}}{S_{2,0}} = -c \cdot p_{2,\text{a-B}} \cdot \int_{\tau_{\mathrm{f}}/c}^{\tau} d\tau \tag{262}$$

The analytical solution is:

$$S_{2,0}(\tau) = S_{2,0}(\tau_{\mathrm{f}}/c) \cdot e^{-c \cdot p_{2,\text{a-B}} \cdot (\tau - \tau_{\mathrm{f}}/c)} \tag{263}$$

From the material balance:

$$S_{3,0}(\tau) = S_{2,0}(\tau_{\mathrm{f}}/c) - S_{2,0}(\tau_{\mathrm{f}}/c) \cdot e^{-c \cdot p_{2,\text{a-B}} \cdot (\tau - \tau_{\mathrm{f}}/c)} \tag{264}$$

Rearranging the terms we get:

$$S_{3,0}(\tau) = \left(S_{1,0}(0) - S_{1,0}(0) \cdot e^{-p_{1,\text{a-A}} \cdot \tau_\text{f}}\right) - \left(S_{1,0}(0) - S_{1,0}(0) \cdot e^{-p_{1,\text{a-A}} \cdot \tau_\text{f}}\right) \cdot e^{-c \cdot p_{2,\text{a-B}} \cdot (\tau - \tau_\text{f}/c)} \tag{265}$$

Finally, we get:

$$S_{3,0}(\tau) = S_{1,0}(0) \cdot \left(1 - e^{-p_{1,\text{a-A}} \cdot \tau_\text{f}}\right) \cdot \left(1 - e^{-c \cdot p_{2,\text{a-B}} \cdot (\tau - \tau_\text{f}/c)}\right) \tag{266}$$

For $\tau = \tau_\text{f}$:

$$S_{3,0}(\tau) = S_{1,0}(0) \cdot \left(1 - e^{-p_{1,\text{a-A}} \cdot \tau_\text{f}}\right) \cdot \left(1 - e^{-p_{2,\text{a-B}} \cdot \tau_\text{f}}\right) \tag{267}$$

C.8 Rate determining liquid-film resistance

In this paragraph, we will compare the three designs for the case where mass transfer through the liquid film around the porous particles is much slower than the reaction and diffusion processes taking place inside the pore (c.f. Figure (15)). Mass transfer through the film can be modeled with Equation (268):

$$\dot{n}_\text{i}^\text{F} = k_{\text{L,n}} \cdot A_\text{n} \cdot \left(S_{\text{i},0} - S_{\text{i,n}}(x = 0)\right) \tag{268}$$

Where $k_{L,n}$ is the liquid side film transfer coefficient. When mass transfer through the film is much slower than the processes inside the pore Equation (269) holds:

$$S_{\text{i,n}}(x = 0) = 0 \tag{269}$$

Therefore, the following material balances can be written for the three conceptual designs:

$$u \cdot \frac{dS_{\text{i},0}}{dz} = -\sum_\text{n} N_\text{n} \cdot k_\text{L} \cdot A \cdot S_{\text{i},0},\ \forall i \in \{1, 2, 3\} \tag{270}$$

In the above equation, n symbolizes the different types of pores that participate in the reaction. Further, in design II, where multiple zones are considered, the material balance must be solved separately for each zone. Analytical solutions representing the yields achieved with the three different conceptual designs when diffusion through the film is the rate-limiting step are given below. These analytical solutions are derived in an analogous way as the analytical solutions for the reaction/diffusion limited cases and for this reason the derivation process is not presented here.

For,

$$K_{\mathrm{n}} = N_{\mathrm{n}} \cdot k_{\mathrm{L,n}} \cdot A_{\mathrm{n}} \cdot \tau_{\mathrm{f}} \tag{271}$$

the analytical solutions are:

$$Y_{\mathrm{I}} = 1 - e^{-K_{\alpha\text{-A}}} - \frac{K_{\alpha\text{-A}}}{K_{\alpha\text{-B}} - K_{\alpha\text{-A}}} \cdot \left(e^{-K_{\alpha\text{-A}}} - e^{-K_{\alpha\text{-B}}}\right) \tag{272}$$

$$Y_{\mathrm{II}} = \left(1 - e^{-K_{\mathrm{a\text{-}A}}}\right) \cdot \left(1 - e^{-K_{\mathrm{a}\text{-}\beta}}\right) \tag{273}$$

$$Y_{\mathrm{III}} = 1 - e^{-K_{\mathrm{a\text{-}A}}} \tag{274}$$

The respective comparison contour plots are presented below:

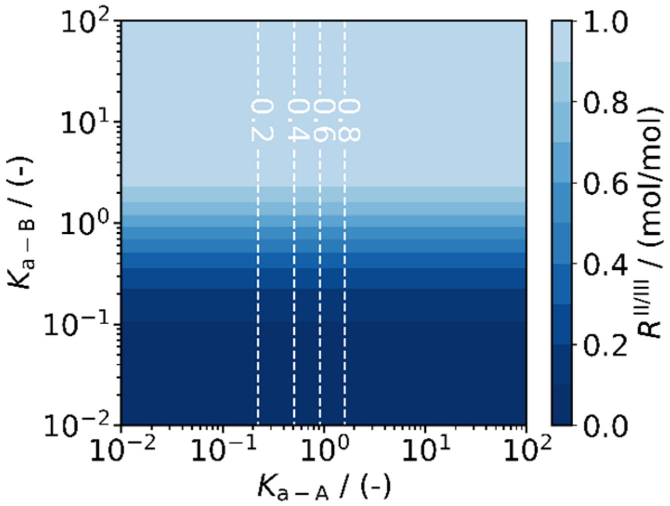

Figure 45: Contour plot of $R_{\mathrm{II/III}}$ and Y_{III} for different values of moduli K_{a-A} and K_{a-B}. $R_{\mathrm{II/III}}$ is shown with a filled contour while Y_{III} is shown with the white dashed lines.

It's interesting to note that, when mass transfer through the film is the rate-limiting

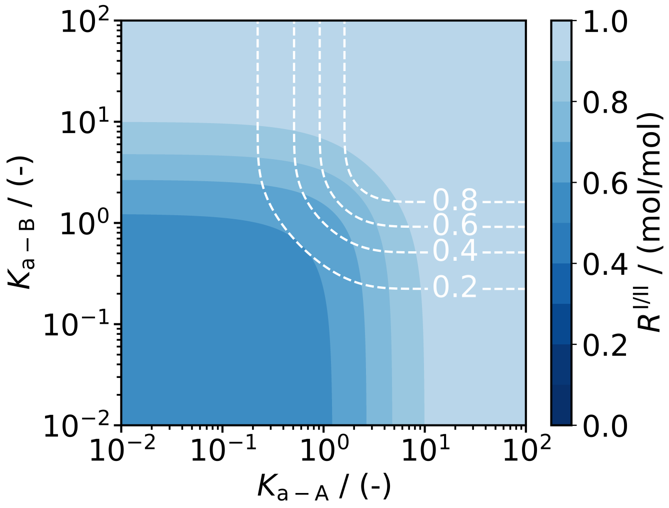

Figure 43: Contour plot of $R_{\mathrm{I/II}}$ and Y_{II} for different values of moduli K_{a-A} and K_{a-B}. $R_{\mathrm{I/II}}$ is shown with a filled contour while Y_{II} is shown with the white dashed lines.

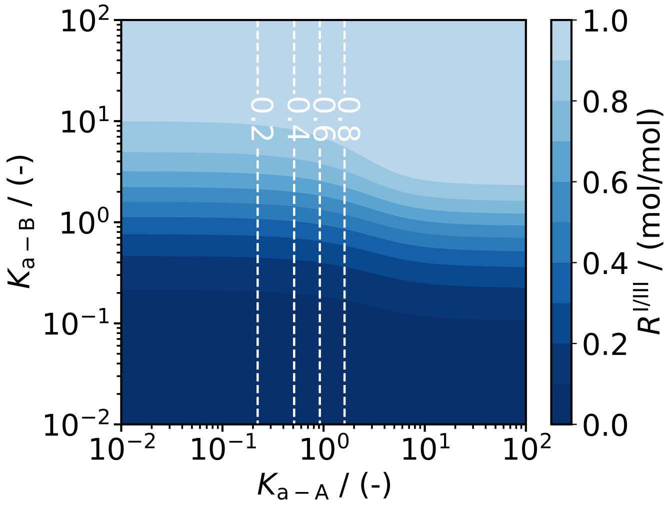

Figure 44: Contour plot of $R_{\mathrm{I/III}}$ and Y_{III} for different values of moduli K_{a-A} and K_{a-B}. $R_{\mathrm{I/III}}$ is shown with a filled contour while Y_{III} is shown with the white dashed lines.

step, for small values of modulus $K_{\alpha-B}$, design III (co-immobilization) has a significant advantage (also at high product yield) over the other two designs.

C.9 Case study solved for different final residence times

The case study solved in the main part of the dissertation is solved again. This time we plot the yields achieved with the three different conceptual designs against the final residence time. Notice that separated zones of individually immobilized enzymes always give slightly better yields than a mixed zone of individually immobilized enzymes. The advantage might become more pronounced for higher-order kinetic models.

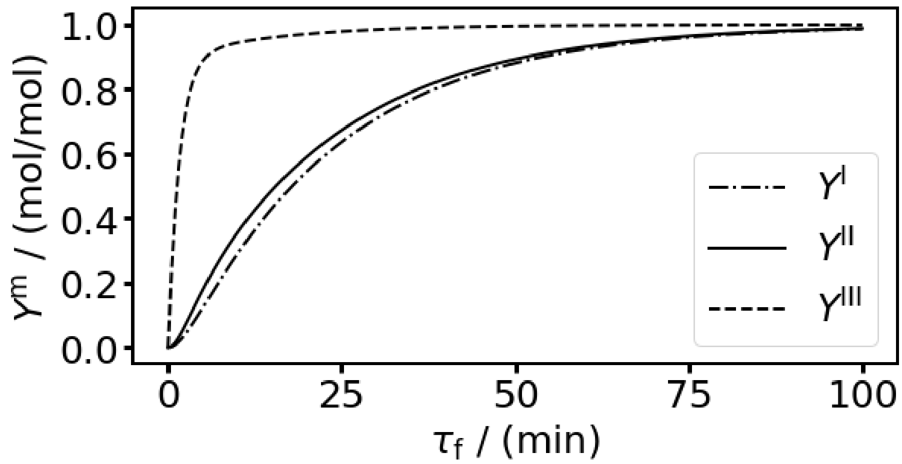

Figure 46: The yields achieved with designs I-III plotted against the final residence time. The parameters have values: $D_1 = 10^{-5}$ dm^2 min^{-1}, $D_2 = 10^{-7}$ dm^2 min^{-1}, $k_{\mathrm{A}} = 2000$ dm^2 μmol^{-1} min^{-1}, $k_{\mathrm{B}} = 2000$ dm^2 μmol^{-1} min^{-1}, $L = 10^{-4}$ dm, $N_{\alpha\text{-A}} = 10^{13}$ dm^{-3}, $N_{\alpha\text{-B}} = 10^{13}$ dm^{-3}, $N_\beta = 2\ 10^{13}$ dm^{-3}, $E_{A,\alpha\text{-A}} = 10$ μmol dm^{-2}, $E_{B,\alpha\text{-B}} = 10$ μmol dm^{-2}, $E_{A,\beta} = 5$ μmol dm^{-2}, $E_{B,\beta} = 5$ μmol dm^{-2}, $c = 2$. Note that in the above case study, the intermediate has a much lower diffusivity than the first substrate.

C.10 Proof of theorem 4

Let us consider again a case with individually immobilized enzymes. Consider two types of porous catalyst particles that catalyze two sequential reaction steps. The first particle type containing A enzymes catalyzes the first step and the second particle containing B enzymes catalyzes the second step. As shown below:

$$S_1 \xrightarrow{\text{A}} S_2 \xrightarrow{\text{B}} S_3 \tag{275}$$

In this subsection, we will prove that positioning a certain total number of A and B catalyst particles in separate zones inside the packed-bed reactor always results in higher product yields than if we were to mix them in one zone when positive order kinetic models are considered, i.e. the reaction rate increases monotonously with the substrate concentration (e.g., non-equilibrium first-order, non-equilibrium and non-inhibitory Michaelis-Menten). The proof is in two parts. First, it is proven that the total conversion of S_1 in the reactor is independent of the distribution of catalyst and only depends on the total mass of catalyst A in the reactor. The second part proves that the maximum product yield is reached when the maximum conversion of S_1 is already reached before catalyst B is reached. Let us define the conversion of S_1 as follows:

$$X_1 = \frac{S_1(0) - S_1(\tau)}{S_1(0)} = 1 - \frac{S_1(\tau)}{S_1(0)} \tag{276}$$

We can rearrange Equation (276):

$$S_1(\tau) = S_1(0) \cdot (1\text{-}X_1) \tag{277}$$

For the differential of S_1 the following holds:

$$dS_1 = -S_1(0) \cdot dX_1 \tag{278}$$

Let's consider the volume dV (c.f. Figure 47), which contains a mass dwA of catalyst particles A and inside which reaction 1 takes place with rate v_1.

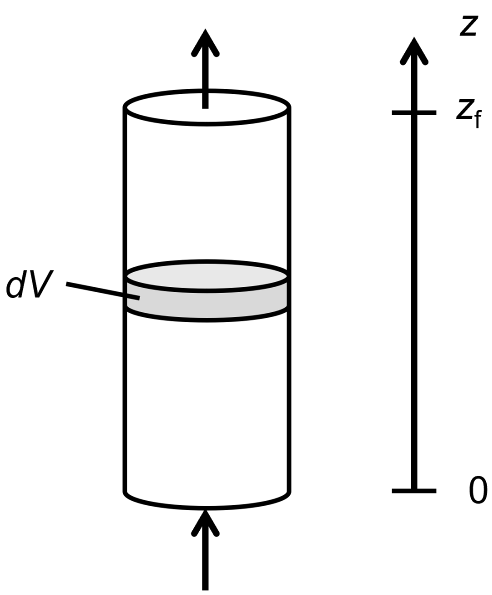

Figure 47: The plug-flow reactor geometry and the considered differential volume element.

The material balance for S_1 in the control volume dV is:

$$\dot{V} \cdot dS_1 = -v_1(S_1) \cdot dw_{\mathrm{A}} \tag{279}$$

Combining Equation 279 with 278 it follows:

$$\dot{V} \cdot S_1(0) \cdot dX_1 = +v_1(S_1(0) \cdot (1\text{-}X_1)) \cdot dw_{\mathrm{A}} \tag{280}$$

By integrating from 0 to $X_{1,\mathrm{f}}$ we get:

$$\int_0^{X_{1,\mathrm{f}}} \frac{1}{v_1(S_1(0) \cdot (1\text{-}X_1))}\ dX_1 = \frac{w_{\mathrm{A}}^{\mathrm{total}}}{\dot{V} \cdot S_1(0)}4 \tag{281}$$

$X_{1,\mathrm{f}}$ is only dependent on the total mass of catalyst wAtotal and not on its distribution in the reactor. We now need to show that positioning catalyst A as early as possible in the packed-bed reactor is advantageous for the second reaction. We define the conversion of the second reaction:

$$X_3 = \frac{S_3(\tau)}{S_1(0)} \tag{282}$$

The reaction stoichiometry gives the material balance of S_2:

$$S_2(\tau) = S_1(0) - S_1(\tau) - S_3(\tau) \tag{283}$$

Combining Equation (283) with Equation (282) and Equation (277) we get:

$$S_2(\tau) = S_1(0) \cdot X_1 - S_1(0) \cdot X_3 \tag{284}$$

Which we can simplify to:

$$S_2(\tau) = S_1(0) \cdot (X_1\text{-}X_3) \tag{285}$$

The differential of Equation (285) is:

$$dS_2(\tau) = S_1(0) \cdot (dX_1\text{-}dX_3) \tag{286}$$

The material balance for S_2 in dV, which contains dw_A and dw_B of catalyst and inside which reactions 1 and 2 take place with rates v_1 and v_2, respectively, is:

$$\dot{V} \cdot dS_2 = v_1(S_1) \cdot dw_{\mathrm{A}} - v_2(S_2) \cdot dw_{\mathrm{B}} \tag{287}$$

Combining Equation (287) with Equation (286), Equation (285) and Equation (277) we get:

$$\dot{V} \cdot S_1(0) \cdot (dX_1 - dX_3) = v_1(S_1(0) \cdot (1\text{-}X_1)) \cdot dw_{\mathrm{A}} - v_2(S_1(0) \cdot (X_1\text{-}X_3)) \cdot dw_{\mathrm{B}} \tag{288}$$

Combining with Equation (287):

$$\dot{V} \cdot S_1(0) \cdot dX_3 = v_2(S_1(0) \cdot (X_1\text{-}X_3)) \cdot dw_{\mathrm{B}} \tag{289}$$

Rearranging Equation (289):

$$dX_3 = \frac{1}{\dot{V} \cdot S_1(0)} \cdot v_2(S_1(0) \cdot (X_1\text{-}X_3)) \cdot dw_{\mathrm{B}} \tag{290}$$

For all X_3:

$$S_1(0) \cdot (X_1\text{-}X_3) \leq S_1(0) \cdot (X_{1,\mathrm{f}}\text{-}X_3) \tag{291}$$

And thus,

$$v_2 \left(S_1(0) \cdot (X_1\text{-}X_3)\right) \leq v_2 \left(S_1(0) \cdot (X_{1,\mathrm{f}}\text{-}X_3)\right) \tag{292}$$

This means that we get the maximum X_3 at the outlet if $X_1 = X_{1,\mathrm{f}}$ for all dw_B. In other words, to maximize the product yield, a maximal conversion of substrate S_1 has to be achieved before positioning the B catalyst in the packed-bed reactor. Therefore, regardless of the type of monotonically rising kinetic model (i.e., positive order, non-equilibrium, without inhibition effects) followed by two sequential heterogeneously catalyzed reactions, positioning the catalysts in separate zones, with catalyst A only in the first zone and catalyst B only in the second zone, is better than mixing the two catalysts together. The above proof can be extended for any number of sequential reaction steps.